

**Dissertation**  
submitted to the  
Combined Faculties for the Natural Sciences and for  
Mathematics  
of the Ruperto-Carola University of Heidelberg, Germany  
for the degree of  
Doctor of Natural Sciences

presented by  
Ram Gopal, M.Sc  
Born in Madikeri, India

Oral examination: 05.05.2010



**Electron Wave Packet Interferences in  
Ionization with Few-Cycle Laser Pulses and  
the Dissociative Photoionization of  $D_2$  with  
Ultrashort Extreme Ultraviolet Pulses**

**Referees: Prof. Dr. Joachim Ullrich  
Prof. Dr. Selim Jochim**



## Zusammenfassung:

Im Rahmen der vorliegenden Arbeit wurden mit einem Reaktionsmikroskop dreidimensionale (3D) Impulsverteilungen ( $\vec{P}$ ) von Elektronen und Ionen gemessen, welche aus der Ionisation von Helium-Atomen mit phasenstabilen, intensiven ( $\sim 4 \cdot 10^{14}$  W/cm<sup>2</sup>) Laserimpulsen von wenigen optischen Zyklen Dauer resultieren. Diese Messungen ergaben, dass die Emission von Elektronen niedriger Energie ( $E_e < 15$  eV) abhängig von der Träger-Einhüllenden-Phase (CEP) bevorzugt in eine der beiden Hemisphäre erfolgt. Im Impulsraum erscheinen bei CEP mit maximaler Asymmetrie deutliche Interferenzstrukturen, die im Rahmen eines einfachen Modells als Attosekunden-Interferenzen zwischen am Atomrumpf gestreuten und direkt emittierten Elektronen-Wellenpaketen erklärt werden können. Diese Ergebnisse zeigen neue Wege auf, Energiepotentiale in Atomen und Molekülen zeitabhängig abzubilden. Im zweiten Teil der Arbeit wurde ein Reaktionsmikroskop entwickelt, konstruiert und in Betrieb genommen, mit dem die dissoziative Photoionisation von  $D_2$  mit ultrakurzen ( $\sim 15$  fs) XUV ( $\sim 32$  eV) Laserimpulsen untersucht wurde. Dabei führt die Kopplung der Dynamik der Dissoziation von  $D_2^+$  an das ionisierte Elektron (aufgrund der Autoionisation) zu einer Symmetriebrechung des Dissoziationsprozesses. Zum ersten Mal konnte dies im Rahmen vorliegender Arbeit mit ultrakurzen Pulsen und in qualitativer Übereinstimmung mit entsprechenden theoretischen Vorhersagen und vorangegangenen Messungen beobachtet werden. Zukünftige Experimente mit variierender XUV-Impulslänge könnten so eine Untersuchung der Autoionisation in einfachen, zweiatomigen Molekülen ermöglichen.

## Abstract:

In this work, using a Reaction Microscope, three-dimensional (3D) electron (and ion) momentum ( $\vec{P}$ ) spectra have been recorded for carrier-envelope-phase (CEP) stabilized few-cycle ( $\sim 5$  fs), intense ( $\sim 4 \cdot 10^{14}$  W/cm<sup>2</sup>) laser pulses (740 nm) impinging on He. Preferential emission of low-energy electrons ( $E_e < 15$  eV) to either hemisphere is observed as a function of the CEP. Clear interference patterns emerge in  $\vec{P}$ -space at CEPs with maximum asymmetry, interpreted as attosecond interferences of rescattered and directly emitted electron wave packets by means of a simple model. These measurements provide an opportunity to potentially image the time-dependent potentials in atoms and molecules. In the second part of this work, a Reaction Microscope was designed, constructed and brought into operation to study the dissociative photoionization of  $D_2$  with ultrashort ( $\sim 15$  fs) XUV ( $\sim 32$  eV) pulses. The coupling of dissociation dynamics of  $D_2^+$  to the ionized electron through the autoionization channels results in breaking of the symmetry of the dissociation process, in qualitative agreement with theory and earlier measurements and observed here for the first time with ultrashort pulses. With control over the duration of the XUV pulses in future experiments, temporal evolution of the autoionization in simple diatomic molecules can eventually be studied.



# Contents

<b>1</b>	<b>Introduction</b>	<b>1</b>
<b>2</b>	<b>Atoms and molecules in external electromagnetic fields</b>	<b>5</b>
2.1	Single photon ionization	5
2.2	Ionization in intense light fields	9
2.2.1	Tunneling ionization	11
2.2.2	Strong Field Approximation (SFA)	16
2.2.3	Rescattering, higher order ATI and high harmonic generation	19
2.3	High Harmonic Generation (HHG)	23
2.3.1	Quantum orbits	24
2.3.2	Phase matching	25
2.4	Attosecond Pulse Trains	27
2.5	Two-colour, two-photon ionization of rare gases with APTs in the presence of an IR field	30
2.5.1	Semi-classical description	31
2.5.2	Sideband oscillations	33
2.6	Photoionization in molecules	34
2.6.1	Molecular structure and Born-Oppenheimer approximation	35
2.6.2	The hydrogen molecular ion	35
2.6.3	Symmetries in diatomic molecules	35
2.6.4	Potential energy curves for the $H_2^+$ ion	37
2.6.5	Selection rules for dipole-allowed transitions in molecules	39
2.7	Summary	40
<b>3</b>	<b>Experimental techniques</b>	<b>43</b>
3.1	Source	44
3.1.1	The laser system	44
3.1.2	HHG chamber	45
3.2	Aligning the XUV and IR beam line	51
3.3	The gas target	53
3.4	The spectrometer	55
3.4.1	Detector	58
3.4.2	Delay-line anodes	58

3.5	Signal processing and data acquisition . . . . .	59
3.6	Reconstructing the momentum vector . . . . .	62
3.6.1	Electron momenta . . . . .	63
3.7	Calibration . . . . .	66
3.8	Resolution and acceptance . . . . .	68
3.9	Performance and experimental procedure . . . . .	70
3.9.1	Two-colour photoionization . . . . .	73
3.10	Experimental setup at Max-Planck Institute for Quantum Optics (MPQ), Garching . . . . .	75
<b>4</b>	<b>Electron Wave Packet interference in ionization with few-cycle laser pulses</b>	<b>77</b>
4.1	Strong field dynamics using few-cycle laser pulses . . . . .	77
4.2	The experiment . . . . .	81
4.3	Results . . . . .	82
4.4	SFA-based model . . . . .	85
4.5	Discussion and outlook . . . . .	90
<b>5</b>	<b>Photoionization of <math>D_2</math> with ultrashort XUV pulses</b>	<b>93</b>
5.1	Overview . . . . .	94
5.2	Experimental details . . . . .	98
5.3	Results . . . . .	98
5.3.1	Kinetic energy spectrum for $D^+$ . . . . .	99
5.3.2	Energy correlation plots . . . . .	101
5.3.3	Molecular Frame Photoelectron Angular Distributions (MFPAD) . . . . .	103
5.3.4	Molecular Frame Electron Momentum Distributions (MFEMDs) for perpendicular transitions, $E_{XUV} = 32(\pm 1)$ eV . . . . .	105
5.3.5	MFEMD for parallel transitions, $E_{XUV} = 32(\pm 1)$ eV and $29(\pm 1)$ eV . . . . .	107
5.4	Discussion and analysis . . . . .	107
5.5	Conclusions and outlook . . . . .	114
<b>6</b>	<b>Summary and Outlook</b>	<b>119</b>
	<b>Appendix</b>	<b>122</b>
	<b>A Atomic units</b>	<b>123</b>
	<b>Bibliography</b>	<b>124</b>
	<b>Acknowledgments</b>	<b>135</b>

# Chapter 1

## Introduction

The last two decades have been a witness to astounding developments in laser technology, where unprecedented control over the laser parameters have led to new sources of pulsed, coherent electromagnetic radiation, which, for example, cover a diverse range of wavelengths in the infrared and visible regions, even extending to the soft X-ray, or, generate peak laser powers of many terawatts ( $1 \text{ TW} = 10^{12} \text{ W}$ ), or, have extremely short pulse durations, ranging from sub-5 femtoseconds ( $1 \text{ fs} = 10^{-15} \text{ seconds}$ ) infrared pulses to 80 attosecond ( $1 \text{ as} = 10^{-18} \text{ seconds}$ ) soft X-ray pulses.

These "table-top" devices have stretched the frontiers of science by creating conditions in the laboratory which allow us to investigate intriguing fundamental questions. For example, the peak light-field intensity reached in the focus of a TW laser is of the order of  $10^{15} \text{ W/cm}^2$ , wherein, a bound electron in the ground state of the hydrogen atom experiences an external field which is  $1/5^{\text{th}}$  of the Coulomb field of the nucleus at the Bohr radius. The question naturally arises, how do atoms and molecules behave in such extreme fields? On the one hand, this question is of fundamental importance as in Nature, matter in large astrophysical systems such as supernovae, Herbig-Haro jets, or giant planets can be routinely found in equivalent conditions [Rem99, Rem00]. On the other hand, potential applications of phenomena associated with intense-laser matter interactions include but are not limited to designing advanced radiation sources, such as nonlinear Thomson synchrotron sources and laser-pumped FELs [Kru00, Esa09] and "table-top" accelerators, such as the laser wake-field accelerator [Kru00, Esa09].

To further illustrate the far-reaching applications of these developments, with pulse durations down to the scale of a hundred femtoseconds, the field of gas-phase molecular dynamics has been revolutionized, initiating a new branch of science known as "femtochemistry." Here, the application of very short laser pulses, to study chemical reactions ranging in complexity from bond-breaking in diatomic molecules to dynamics in larger organic and biological molecules, has led to breakthroughs in our understanding of fundamental chemical processes [Zew00]. In fact this knowledge has opened up new vistas in physical chemistry such as 'Coherent Control', with the aim of selectively influencing atomic and molecular dynamics with the help of (shaped) ultrashort laser pulses [Wol05].

At the forefront of these innovations in laser technology, is the endeavor to develop

sources of intense light-fields with pulse durations down to 5 fs [Nis97]. In such a pulse the electric field has only 2-3 cycles of oscillation, hence, termed as a few-cycle laser pulse, and a new parameter, called the Carrier Envelope Phase (CEP) [Bra00], begins to play an important role. Control over the relative phase between the maximum of the pulse envelope and the nearest maximum of the carrier wave - the CEP or absolute phase - allows us to essentially fix the sign and the amplitude of the electric field at the peak of the pulse, and therefore, the waveform of the pulse. With superlative stabilization and control of the CEP in few-cycle laser pulses being achieved in the last five years [Gou05, Kre09b], the study of the interaction of waveform-controlled few-cycle laser pulses with atoms and molecules assumes contemporary significance. In fact, this waveform control on the level of a sub-cycle was first demonstrated in the generation of isolated sub-femtosecond extreme ultraviolet (XUV) fields from few-cycle infrared pulses [Bal03]. Since then, CEP controlled few-cycle laser pulses have been used to steer the direction of electron emission from atoms (see e.g. [Lin05, Mil06] and references therein), or in the localization of electrons in molecular fragmentation [Kli06, Kre09a].

Concomitant with these advances, table-top sources of coherent ultrashort pulses with photon energies in the XUV regions have been realized through the process of Higher order Harmonic Generation (HHG). For example, with a driving infrared laser fields of durations  $\sim 30$  fs, XUV ( $\hbar\omega = 20 - 45$  eV) pulse trains under an envelope of  $\sim 15$  fs have been demonstrated in only a few laboratories around the world (for eg. [Lun09, JILA09]). With the availability of such pulses,

- highly excited states of atoms and molecules, which are simply not directly accessible using visible or UV laser photons, can now be populated coherently through the XUV photons.
- few femtoseconds to sub-femtosecond time resolution is achieved for the first time, necessary to directly observe IR or XUV-induced ultrafast nuclear or electronic dynamics, e.g. during a chemical reaction.

This field, often dubbed 'attosecond science', though in a nascent stage of development, has, however, yielded pioneering results [Kra09]. For example in [Gag07, San08] the real time evolution of the molecular potential has been captured in the XUV-induced fragmentation of simple molecules. In another experiment, sub-femtosecond XUV pulses were used to track, in a time resolved measurement, the process of strong-field induced tunneling of valence electrons in atoms [Uib07].

In parallel to the development of novel ultrashort sources charted above, rapid strides have been made in detection techniques, which have in fact allowed many of the above phenomena to be observed. In the last decade, the invention of the Reaction Microscope<sup>1</sup> represented a 'quantum leap' in detection techniques. The application of schemes to project the charged particles onto position sensitive detectors, allowed for the first time, the retrieval of all the components of the momentum vector of (several) charged fragments in

---

<sup>1</sup>also known as COLTRIMS (COld Target Recoil Ion Momentum Spectroscopy)

coincidence. Moreover, due to the large detection solid angle, often reaching 100% of  $4\pi$ , the many-particle final-state momentum space is recorded in unprecedented completeness. Thus, the kinematically complete investigations into fragmentation of atoms and molecules induced by single photon, charged particles and intense laser fields have lead to benchmark results which have been extensively reviewed in [Ull03].

The work presented in this thesis is motivated by the leading-edge developments introduced above. It represents an attempt to amalgamate the state-of-the-art technology in the areas of laser sources and multi-particle measurement techniques to investigate phenomena in hitherto unexplored regimes with extraordinary completeness. In particular, in the scope of this thesis, measurements were carried out with intense few-cycle pulses interacting with helium in a Reaction Microscope. These experiments have enhanced our understanding of the mechanism of single ionization, in the case where only a single cycle of the electric field contributes to the ionization. Moreover, the measurements provide an opportunity to potentially extract information about the time-dependent potential in atoms and molecules. Likewise, the promise of time-resolved studies of highly excited states in atoms and molecules was indeed the incentive for assembling a new experimental setup at the Max Planck Institute for Nuclear Physics (MPI-K), Heidelberg. In this PhD thesis, one of the major achievements was the construction and installation of a dedicated Reaction Microscope in conjunction with a table-top, ultrashort XUV source based on HHG.

In 2005-2006, a 10 kHz, 25 fs, 1 mJ, laser system was installed at the HHG laboratory at MPI-K. With its high repetition rate, pulse energy scalability [Gag08] and CEP control, the laser combines many state-of-the-art features. By the end of 2006, the first results of HHG at MPI-K were reported [Rie06]. In parallel, the construction of a dedicated Reaction Microscope was initiated, which is the main experimental contribution of this PhD work. In the autumn of 2007, a prototype of the present Reaction Microscope [Dew06] was transported to the Max Planck Institute for Quantum Optics (MPQ), Garching, under the aegis of a collaboration between the groups of MPI-K and MPQ, to be coupled with an intense few-cycle laser source [Gou05] at MPQ. The thesis work also covers results, analysis and interpretation of the data from the subsequent experiments carried out. Finally in the spring of 2009, with the HHG source optimized for maximum photon flux and stability over many hours of operation, the new Reaction Microscope was installed at the HHG laboratory at MPI-K. The first experiments with this setup, with promising results, are also described in this work.

The organization of the thesis is as follows: we begin in Chap. 2 by laying out the basics of interaction of atoms and molecules with electromagnetic fields. The first part of this chapter introduces single ionization mechanisms in intense laser fields, particularly in the framework of the Strong Field Approximation (SFA). One of the myriad phenomena accompanying intense laser-atom interactions is HHG, which is elaborated in the next part. Finally, we give a brief overview of the interaction of XUV photons, which can be generated through HHG, with simple molecules such as  $H_2$  or  $D_2$ . The focus of Chap. 3 is the experimental setup and technique used in this work. We begin with a brief description of the laser system and the optical setup for High Harmonic Generation at the MPI-K. This is followed by an elaboration on the construction of the coincident ion-electron momentum

spectrometer, that is the Reaction Microscope. In the final sections of this chapter, we overview the performance and working of the Reaction Microscope installed at the HHG laboratory in MPI-K. The first results of experiments carried out as a part of this PhD work are reported in Chap. 4. These experiments were executed at the MPQ, Garching with intense few-cycle laser pulses impinging on helium. The chapter also describes the theoretical model, based on SFA, which was developed in the course of this work. The results and interpretations elaborated in this chapter are the basis of Ref. [Gop09]. The chapter following this, details experiments carried out with the setup presented in Chap. 3. Photoionization and fragmentation of  $D_2$  with ultrashort XUV pulses was studied as a prototype experiment to illustrate the full capability of the setup for promising experiments in the future. Finally we conclude with a brief summary of this work and also present an outlook for future experiments.

# Chapter 2

## Atoms and molecules in external electromagnetic fields

The work presented in this thesis covers a large spectrum of phenomena associated with the interaction of atoms and molecules with external electromagnetic fields. Specifically, while Chap. 4 discusses intense infrared (IR) laser fields acting on a rare gas atom such as helium (He), Chap. 5 presents the results of the interaction of coherent extreme ultraviolet (XUV) radiation with a simple molecule such as  $D_2$ . The aim of this chapter is therefore, to introduce the various aspects of photon-atom/molecule interactions, thereby providing a theoretical background for the experimental results presented in this work. We begin with describing ionization of rare gas atoms in intense laser fields (§2.2). We show later that an application of such interactions is in the development of a table-top coherent, ultrashort source of XUV radiation (§2.3 and §2.4). Finally in §2.6 we introduce a few concepts relating to photoionization in molecules with XUV radiation.

### 2.1 Single photon ionization

Single photon ionization occurs when a single quantum of electromagnetic radiation ( $E_\gamma = \hbar\omega$ )<sup>1</sup> is absorbed by the atom, thereby transferring enough energy to a bound electron (with binding energy  $E_b$ ), to set it free. While being referred to as photoionization (PI) in atoms, the analogous process in solids is historically more commonly known as the photoelectric effect. The electron then emerges into the continuum with a kinetic energy ( $E_e$ ) which is the excess of  $E_\gamma$  over  $E_b$  (the recoil-ion carries away a negligible amount of the kinetic energy). For example, consider a photon with energy,  $E_\gamma = 100$  eV impinging on a Helium atom (Fig. 2.1). The valence electron has a binding energy  $E_b = 24.6$  eV, also known as the first ionization potential ( $I_P$ ). It now emerges into the continuum with a kinetic energy  $E_e = E_\gamma - I_P = 75.4$  eV. When this process is observed in a momentum spectrometer as the Reaction Microscope [Dor96], the electron and the recoil-ion are measured to have the same momentum (through momentum conservation) with a magnitude  $|\vec{p}| = \sqrt{2E_e} = 2.3$

---

<sup>1</sup> $\hbar = 1$  in atomic units (a.u.), the units used throughout this chapter. See Appendix A for details

a.u.. Plotted in the right panel of Fig. 2.1 is a projection of the experimental momentum distribution [Dor96] of the recoil-ion (and therefore, of the photoelectron) in the ionization of He with a single photon  $E_\gamma = 100$  eV . Along the horizontal axis is the momentum along the polarization axis of the ionizing radiation. On the vertical axis is the momentum in a plane transverse to that of the polarization axis.

Single Photon Ionization

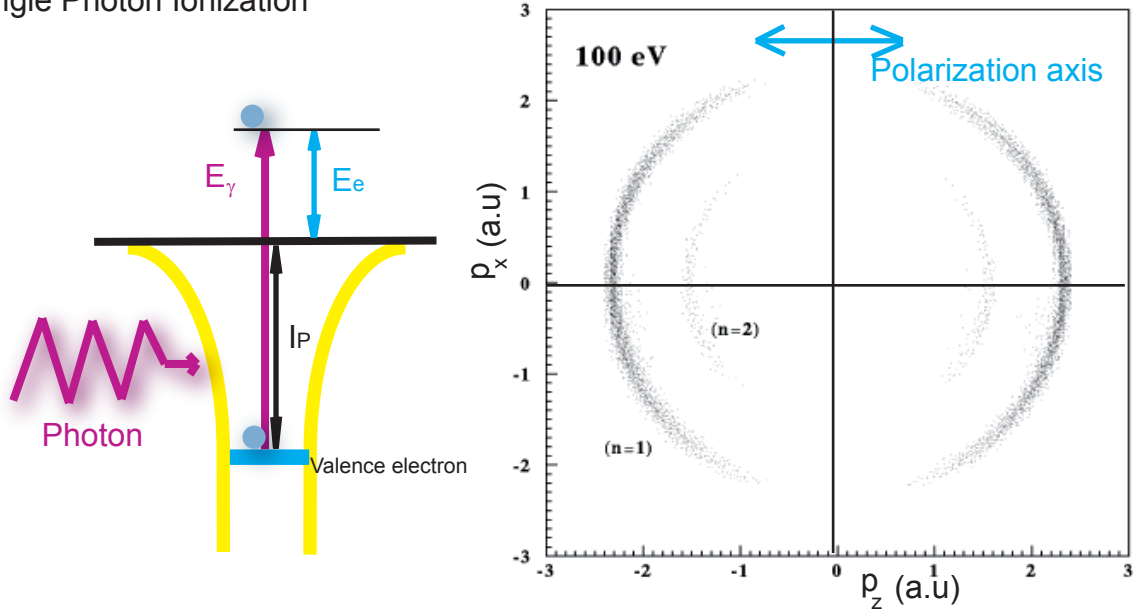


Figure 2.1: (Left) The single-photon ionization process in a rare gas atom. The electron emerges with an energy  $E_e$ . In 3D momentum space, the electron therefore, lies on the surface of a sphere of radius  $|\vec{p}| = \sqrt{2E_e}$ . (Right) A cut of the experimentally measured 3D momentum distribution in the plane, where the horizontal axis is the polarization axis of the ionizing radiation. The distribution labeled  $n = 1$  is that corresponding to an electron with energy  $E_e = 75.4$  eV, i.e. the ionization of the valence electron in He. (Adapted from [Dor96])

To theoretically describe the process of photoionization (see [Bra03] for the complete treatment) we must consider the interaction of the electromagnetic field with an electron in the Coulomb field of its parent ion. In general, the Hamiltonian of a (spin less) electron in an electromagnetic field described by a vector potential  $\vec{A}$  and scalar potential  $\phi$ , is given by

$$H = \frac{1}{2} \left( \vec{p} + \frac{\vec{A}}{c} \right)^2 + \phi \quad (2.1)$$

with  $\vec{A}$  and  $\phi$  given by the Maxwell's equation:

$$\vec{E}(\vec{r}, t) = -\nabla\phi - \frac{1}{c} \frac{\partial \vec{A}}{\partial t}, \quad (2.2)$$

$$\vec{B}(\vec{r}, t) = \nabla \times \vec{A}, \quad (2.3)$$

$$\nabla \cdot \vec{A} = 0, \quad (2.4)$$

$$\phi = 0 \quad (2.5)$$

and,  $\vec{p} = -i\nabla$  is the momentum of the electron. It is convenient to take the scalar potential  $\phi$  to be the Coulomb potential of the parent nuclei  $-Z/r$ , so that the Schrödinger equation for the electron in the influence of the electromagnetic field and the Coulomb field of the atom is given by

$$\left[ -\frac{1}{2}\nabla^2 - \frac{Z}{r} - \frac{i}{c}\vec{A} \cdot \nabla + \frac{1}{2c^2}\vec{A}^2 \right] \psi(r, t) = i \frac{\partial \psi(r, t)}{\partial t}, \quad (2.6)$$

Under the assumption of a weakly perturbing electromagnetic field  $|\vec{p}| \gg |\vec{A}|$ ,  $\vec{A}^2$  can be neglected. In terms of photons, this implies that there is emission or absorption of only one photon at a time. So, we may formulate the eq. 2.6 to be in the well known form of standard perturbation theory as,

$$[H_0 + H_{int}(t)] \psi(r, t) = i \frac{\partial \psi(r, t)}{\partial t} \quad (2.7)$$

$$\text{with } H_0 = -\frac{\nabla^2}{2} - \frac{Z}{r}, \quad (2.8)$$

$$\text{and } H_{int}(t) = -\frac{i}{c}\vec{A} \cdot \nabla \quad (2.9)$$

such that  $H_{int}(t)$  is the interaction Hamiltonian describing the perturbation. For example, a plane polarized electromagnetic field can be represented as

$$\vec{A}(\vec{r}, t) = \hat{e}A_0 \left[ \exp(i(\vec{k} \cdot \vec{r}) - \omega t) + c.c \right] \quad (2.10)$$

such that<sup>2</sup>,  $\vec{E}(\vec{r}, t) = -1/c \left[ \partial \vec{A}(\vec{r}, t) / \partial t \right] = \hat{e}E_0 \left[ \exp(i(\vec{k} \cdot \vec{r} - \omega t + \pi/2)) + c.c \right]$ , where  $E_0 = \omega A_0/c$ . The explicit time dependence of the interaction Hamiltonian can also be extracted to write it in the form  $H_{int} = H' [\exp(i\omega t) + c.c]$  and  $H' = E_0/\omega \exp(i\vec{k} \cdot \vec{r}) \hat{e} \cdot \nabla$ . The first order perturbation theory therefore, gives the probability per unit time for the radiation induced transition between an initial state  $\psi_b$  and the final state  $\psi_f$ , with energies  $E_b$  and  $E_f$  respectively, as

$$W_{fb} = 2\pi \overbrace{|\langle \psi_f | H' | \psi_b \rangle|^2}^{M_{fb}} \delta(E_f - E_b - E_\gamma), \quad (2.11)$$

---

<sup>2</sup> $c.c$  = complex conjugate

where,  $M_{fb}$  is known as the transition matrix element which now reads as,

$$M_{fb} = \hat{\epsilon} \cdot \frac{E_0}{\omega} \left\langle \psi_f \left| \exp(i\vec{k} \cdot \vec{r}) \nabla \right| \psi_b \right\rangle \quad (2.12)$$

However, while the above expression pertains to transitions between two bound states, in photoionization from the ground state, the final state  $\psi_f$  corresponds to an electron in the continuum with a momentum<sup>3</sup>  $\vec{p}_f = (p_f, \theta, \phi)$  [Fed97, Bet77]. One now has to consider the transition rate  $d^2w$  to an interval of states in momentum space  $d\vec{p} = p \cdot dE \cdot d\Omega$  around the energy  $E_e = p_f^2/2$  given by the energy conservation  $E_e = E_\gamma - I_P$ . We have therefore,

$$\frac{d^2w}{dE d\Omega} = 2\pi |M_{fb}|^2 \cdot p \cdot \delta(E_e - E_\gamma - I_P) \quad (2.13)$$

By integrating over  $E$ , we finally obtain the probability per unit time of observing a photoelectron with a momentum  $p_f$  in a solid angle  $d\Omega = \sin\theta d\theta d\phi$ :

$$\frac{dw}{d\Omega} = 2\pi |M_{fb}|^2 p_f \quad (2.14)$$

We are finally left with evaluating the transition matrix element

$$M_{fb} = \hat{\epsilon} \cdot \frac{E_0}{\omega} \left\langle \psi_E \left| \exp(i\vec{k} \cdot \vec{r}) \nabla \right| \psi_b \right\rangle \quad (2.15)$$

Now, under the dipole approximation,  $\exp(i\vec{k} \cdot \vec{r}) = 1 + i\vec{k} \cdot \vec{r} + \dots$ , and when  $|\vec{k}||\vec{r}| \ll 1$ ,  $\exp(i\vec{k} \cdot \vec{r}) \approx 1$ . This is valid so long the wavelength of the interacting radiation ( $\lambda = 2\pi/k$ ) is larger than the Bohr radius of the atom, i.e. for  $E_\gamma < 10$  keV. Under this approximation the transition matrix transforms to

$$M_{fb} = \hat{\epsilon} \cdot \frac{E_0}{\omega} \langle \psi_f | \nabla | \psi_b \rangle \quad (2.16)$$

Further, it can be shown that  $\langle \psi_f | \nabla | \psi_b \rangle = \omega \langle \psi_f | \vec{r} | \psi_b \rangle$  [Bra03]. Additionally, if the interacting radiation is polarized along the  $z$  axis, then  $\hat{\epsilon} \cdot \vec{r} = z$ , allowing the dipole matrix element to be expressed as,

$$M_{fb} = E_0 \langle \psi_f | z | \psi_b \rangle \quad (2.17)$$

Now, we may include the dipole matrix element in eq. 2.14 to obtain the differential photoionization rate. The transition rate per photon, called *cross section* is, however, the more commonly used term. So the differential cross section can be defined as:

$$\frac{d\sigma}{d\Omega} = \frac{1}{N_{ph}} \frac{dw}{d\Omega} = 2\pi\omega^3 |\langle \psi_f | z | \psi_b \rangle|^2 \quad (2.18)$$

---

<sup>3</sup>in spherical polar coordinates

where,  $N_{ph}$  is the photon flux: the number of photons per unit area per unit time. For example from the ground state of a hydrogen-like atom,  $\psi_b = \psi_{100} = R_{1s}(r)Y_{00}(\theta, \varphi)$ , the final state wave function of the electron in the continuum,  $\psi_f = \psi_{\ell m}$ , can be written as an expansion of spherical harmonics  $R_{\ell l}(r)Y_{\ell m}(\theta, \vartheta)$ , leading to

$$\langle \psi_{\ell m} | z | \psi_{100} \rangle = \sum_{lm} a_{lm} \langle R_{\ell l}(r)Y_{\ell m}(\theta, \phi) | r \cos \theta | R_{1s}(r)Y_{00}(\theta, \phi) \rangle \quad (2.19)$$

Using the selection rules for dipole allowed transitions for linearly polarized radiation,  $\Delta l = \pm 1$ ,  $\Delta m = 0$ , there are at most two partial waves possible. Furthermore in an experiment which is not sensitive to the spin of the initial and final states, we may sum over the contributions from the spin states, so that the differential cross sections have no longer any terms containing  $\phi$ . So it is easy to see that a general expression for the differential cross section can be written as

$$\frac{d\sigma}{d\Omega} = \frac{\sigma}{4\pi} [1 + \beta \cdot P_2(\cos \theta)] \quad (2.20)$$

$$P_2(\cos \theta) = \frac{1}{2}(3 \cos^2 \theta - 1) \quad (2.21)$$

Here  $P_2$  is the Legendre Polynomial of second order, and  $\theta$  is the angle between the direction of the emitted electron and the polarization axis.  $\beta$  is defined as the anisotropy parameter of the photoelectron angular distribution.  $\beta$  lies in the interval  $[-1, 2]$  and depends on the initial state of the electron prior to the ionization. For example, for ionization from the  $s$ -electron shell ( $l_b = 0$ ), the outgoing wave can only be a  $p$  type ( $\sim \cos^2 \theta$ ), therefore, with a  $\beta$  parameter of 2. On the other hand for ionization from higher shells,  $p, d, f \dots$  or  $l_b = 1, 2, 3, \dots$ ,  $\beta$  is dependent on the photoelectron energy, as there are two competing outgoing channels:  $l_b \pm 1$ , which interfere to generate the final angular distribution [Bet77, Coo68].

## 2.2 Ionization in intense light fields

When the photon energy is not sufficient to cause ionization,  $E_\gamma < I_P$ , but the target atom is irradiated with a surfeit of such photons, there exists a probability for the absorption of multiple photons at the same time leading to ionization, termed as Multiphoton Ionization (MPI) [Del00]. Given that no real intermediate states of the atom are accessible by a single photon, the Bohr-correspondence principle:  $\omega = E_f - E_b$ , is violated. Such an electronic transition is, however, possible through the uncertainty principle for energy and time,  $\Delta E \Delta t \geq 1$ . The relevant interpretation in this case is that a transition with the energy difference  $\Delta E = E_\gamma$  is possible, with the condition that the electron can be found in the *virtual* state with energy  $E_b + \Delta E$ , however, only for the time  $\Delta t$ , unlike transitions to real states which have long lifetimes. Thus, MPI, with  $E_\gamma < I_P$  can occur through multiple intermediate virtual states, as sketched in Fig. 2.2(a). Furthermore the atom can absorb photons in excess of the minimum number required for ionization to take place, in a phenomenon called 'Above Threshold Ionization' (ATI) [Ago79]. Therefore, at

sufficiently high intensities of the light field, the photoelectron spectrum exhibits several peaks separated by the photon energy  $E_\gamma$ , appearing at the energies  $E_e = (n + s)\omega - I_P$ , where  $n$  is the minimum number of photons required for ionization and  $s$  is the number of additional photons absorbed.

### Multi-Photon Ionization

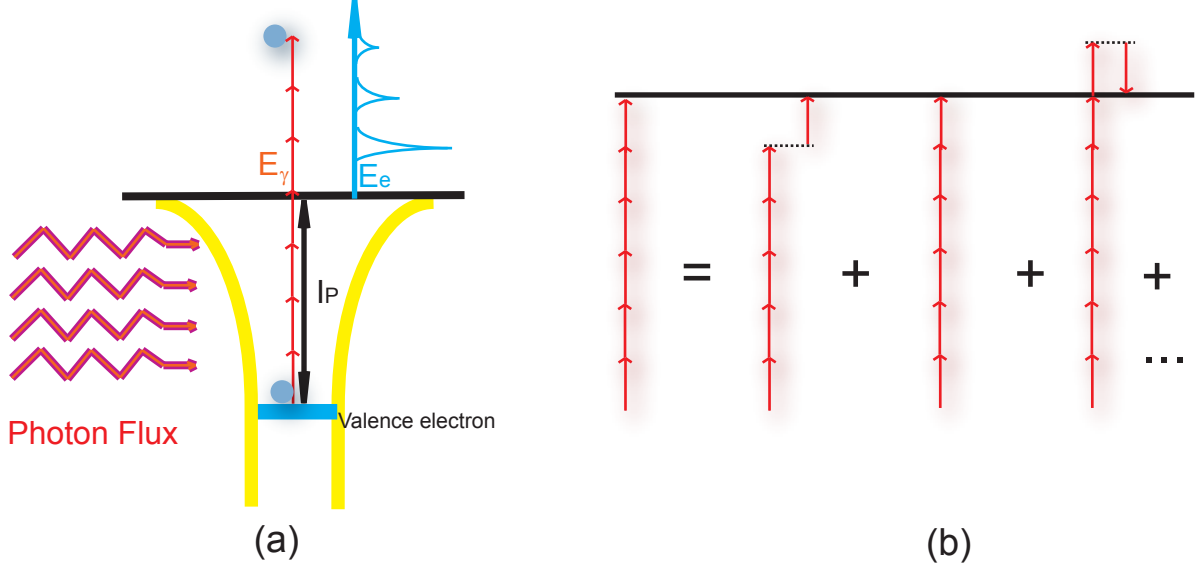


Figure 2.2: (a) Multi-Photon Ionization (MPI) is illustrated as a step-wise ascendancy of the electron from the ground state through virtual states separated by the one-photon energy, leading to the continuum. The atom may absorb more quanta of photons necessary than to just ionize, manifesting as Above Threshold Ionization (ATI) - peaks in the electron energy spectrum ( $E_e$ ). (b) The transition matrix element for the  $n$ - photon process has contributions through different pathways.

At low intensities ( $\leq 10^{13}$  W/cm<sup>2</sup> at  $\lambda = 800$  nm), the so-called lowest order perturbation theory (LOPT) [Lam76, Fai86] can be used to model the multiphoton processes. Simply stated, the theory calculates the rate of an  $n$ - photon transition by using the  $n$ th order perturbation theory for the atom-field interaction (variation of eq 2.14) as

$$W_{fb}^{(n)} = 2\pi(2\pi\alpha)^n I^n \left| T_{fb}^{(n)} \right|^2 \rho(E_e) \quad (2.22)$$

where  $\alpha$  is the fine structure constant,  $I = |\vec{E}|^2$  is the intensity of the field, and  $T_{fb}^{(n)}$  is the LOPT transition matrix element for the absorption of  $n$  photons given by [Lam76, Fai86] (illustrated in Fig. 2.2(b))

$$T_{fb}^{(n)} = \sum_{\kappa_1} \sum_{\kappa_2} \dots \sum_{\kappa_{n-1}} \frac{\langle \psi_f | \hat{\epsilon} \cdot \mathbf{R} | \psi_{\kappa_{n-1}} \rangle \dots \langle \psi_{\kappa_2} | \hat{\epsilon} \cdot \mathbf{R} | \psi_{\kappa_1} \rangle \langle \psi_{\kappa_1} | \hat{\epsilon} \cdot \mathbf{R} | \psi_b \rangle}{(E_b + (n-1)\omega - E_{\kappa_{n-1}}) \dots (E_b + 2\omega - E_{\kappa_2})(E_b + \omega - E_{\kappa_1})} \quad (2.23)$$

with the summations over the intermediate states  $\psi_{\kappa_1}, \psi_{\kappa_2}, \dots, \psi_{\kappa_{n-1}}$ , assumed to include integrations in the atomic continuum. The significance of eq. 2.22 is the dependence of the ionization rate on the intensity of the incident field in the  $n$ -th order, where  $n$  is the number of photons absorbed [Fab82]. So, according to the LOPT, photoelectron spectra would show an exponential drop off for higher energy peaks, as seen in Fig. 2.3(a). But as the intensity is increased ( $> 10^{13} \text{W/cm}^2$ ), higher energy peaks appear, accompanied by suppression of those at lower energies as in Fig. 2.3(b). The reason for this peak suppression is the Stark-shift of the atomic states in the presence of the laser field [Mul02]. For low laser frequencies (eg.  $E_\gamma = 1.55 \text{ eV}$ ), the AC-Stark shifts in the lowest bound states is negligible, while those in the continuum and the Rydberg states are of significant magnitude, and are essentially given by the kinetic energy of a classical 'free' electron which quivers in the alternating field of the laser radiation, also known as the *ponderomotive energy* [Cor01].

$$U_p = \frac{I}{4\omega^2} \text{ in a.u} \quad (2.24)$$

At an intensity of  $\sim 3.2 \cdot 10^{13} \text{W/cm}^2$ ,  $U_p \sim 1.55 \text{ eV} = E_\gamma$ , implying that the effective intensity dependent ionization potential for the atom,  $I_p^*(I) = I_p + U_p(I)$ , is now increased by the one-photon energy, energetically prohibiting the ionization by  $n$  photons (Fig. 2.3(b)). However, since the atom encounters various intensities in the course of its interaction with a smoothly varying laser pulse, the lower energy peaks are not altogether absent in the final spectrum [Pet88].

The angular distributions of the electrons in the ATI spectra can be expected to be strongly aligned along the axis of polarization of the applied laser field [Wie03] (Fig. 2.4). The electrons in momentum space essentially lie on concentric spheres, i.e., constant energy surfaces, separated by the one-photon energy. Depending on the intensity of the laser, the details in the energy and angular distribution of the electrons reflect multiple processes such as channel switching, multiphoton resonant and non-resonant ionization and AC stark splitting [Wie03].

### 2.2.1 Tunneling ionization

As we progress to higher intensities of the laser (with low photon energies),  $\sim 10^{14}$ - $10^{15} \text{W/cm}^2$ , the ponderomotive energy gained by the electron in the laser field comes close to the ionization potential. E.g.: intensity  $\sim 3 \cdot 10^{14} \text{W/cm}^2$ ,  $U_p \sim 15 \text{ eV} \sim I_p(\text{Argon})$ . The simple picture of ATI peaks presented above is no longer valid, as the external field is not perturbative, and rather, is comparable to the Coulomb field of the nucleus. In experiments, the sharp ATI peaks blur into a continuous distribution with poorly contrasted peaks [Aug89, Mev93]. At such high laser intensities, one usually makes a transition from a 'photon'- based picture, to a 'field'- based description of ionization. This transition is formally treated using the so called Keldysh parameter [Kel64]  $\gamma = \sqrt{I_p/2U_p}$ . Specifically, when  $\gamma$  is far greater than 1, the perturbative picture leading to MPI is more applicable. On the other hand, the case of  $\gamma < 1$  is generally termed as the 'Tunneling Ionization' regime (Fig. 2.5). In the tunneling regime, ionization is viewed as a two-step process.

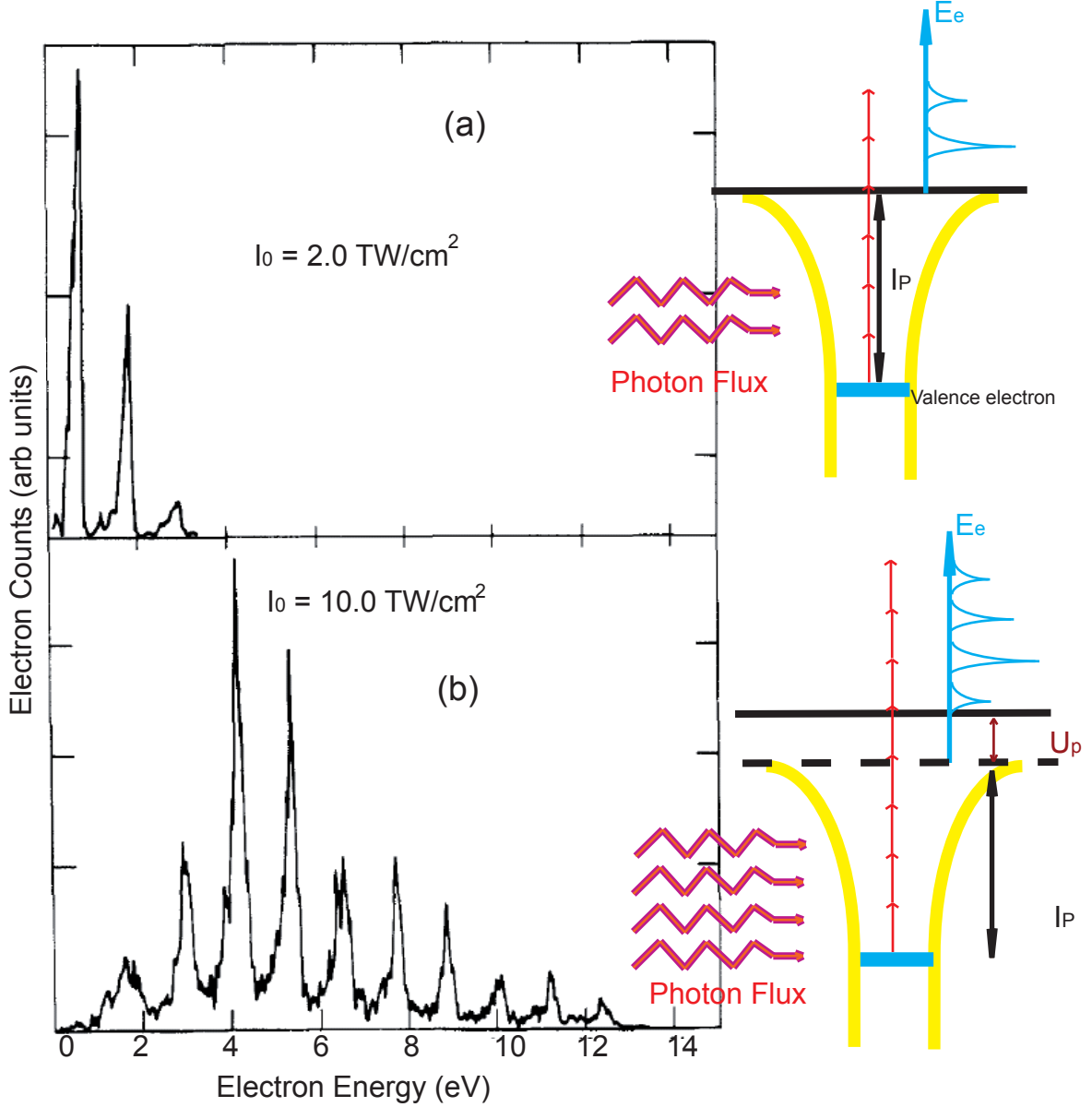


Figure 2.3: Experimental ATI peaks [Pet88] for two different intensities. (a) For a  $I = 2 \cdot 10^{12} \text{ W/cm}^2$ , the intensity of the electron energy peaks show an exponential fall with energy, indicating that the  $n + 1$ - photon process is less likely than the  $n$ -photon process. However, when  $I$  is increased to (b)  $1 \cdot 10^{13} \text{ W/cm}^2$ , the AC-Stark shift of the near-continuum levels at the peak of the electric field, increases the ionization potential by  $U_p$ , thereby suppressing the lower-order peaks (see text).

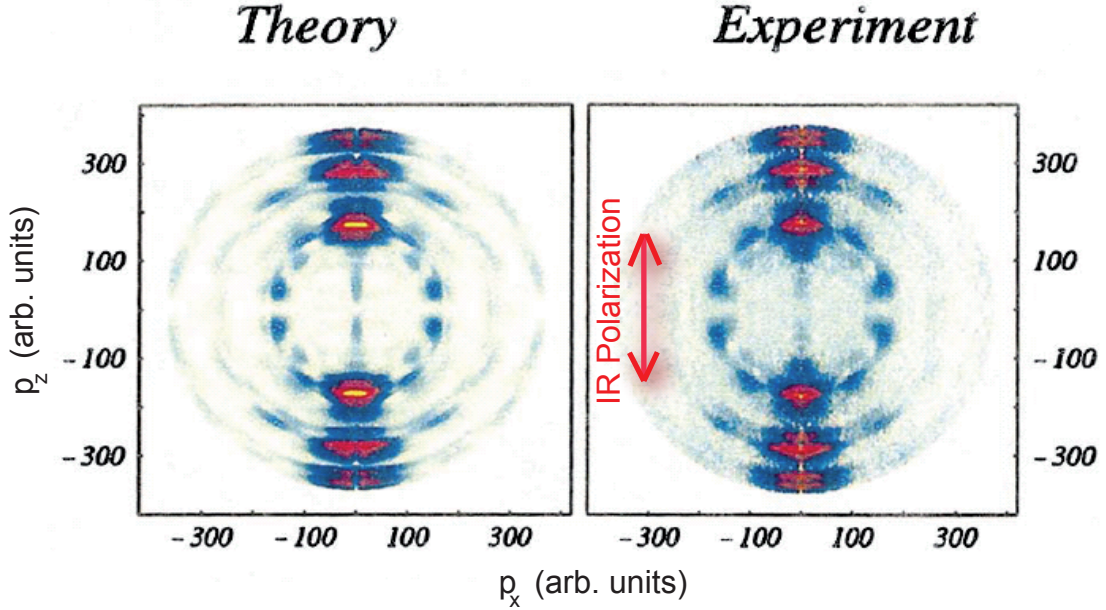


Figure 2.4: The theoretical (left) and experimental angular distribution are anisotropic being aligned preferentially along the polarization axis. The ATI peaks which lie on concentric surfaces in momentum space, separated by one-photon energy, are seen as rings in a cut through the 3D distribution. (Adapted from [Wie03])

In the first step, the Coulomb field of the ion core is so modified due to the laser that the electron has a probability of tunneling through the barrier formed by the combined potential (Fig. 2.5). The electron therefore, emerges into the continuum with almost zero velocity. In the second step, the electron now sees the strong field of the laser field, wherein it is driven back and forth by the field ('quiver' motion). For short laser pulses, where the electron remains within the spatial confinement of the field during the pulse, the electron returns this 'quiver' energy back to the field at the end of the pulse, but is left with a *drift* energy determined by the phase of the field at the 'time of birth' of the electron.

To see this, a semi-classical treatment of the two-step model can be employed [Cor89]. In the tunneling step, obviously described quantum-mechanically, the laser is considered as a quasi-static field with an instantaneous value  $E(t)$  at the time  $t$ , and the corresponding tunneling rate is given by the well-known Ammosov-Delone-Krainov (ADK) rate [Amm86]

$$\Gamma(t) = AI_P \left( \frac{4\sqrt{2I_P^3}}{|E(t)|} \right)^{2n^* - |m| - 1} \exp \left( -\frac{4\sqrt{2I_P^3}}{3|E(t)|} \right) \quad (2.25)$$

where  $n^* = Z/\sqrt{2I_P}$  is the effective principle quantum number, with  $Z$  as the charge of nucleus and,  $m$  as the projection of the angular momentum in the direction of the laser polarization. The highly non-linear dependence on the instantaneous electric field leads to

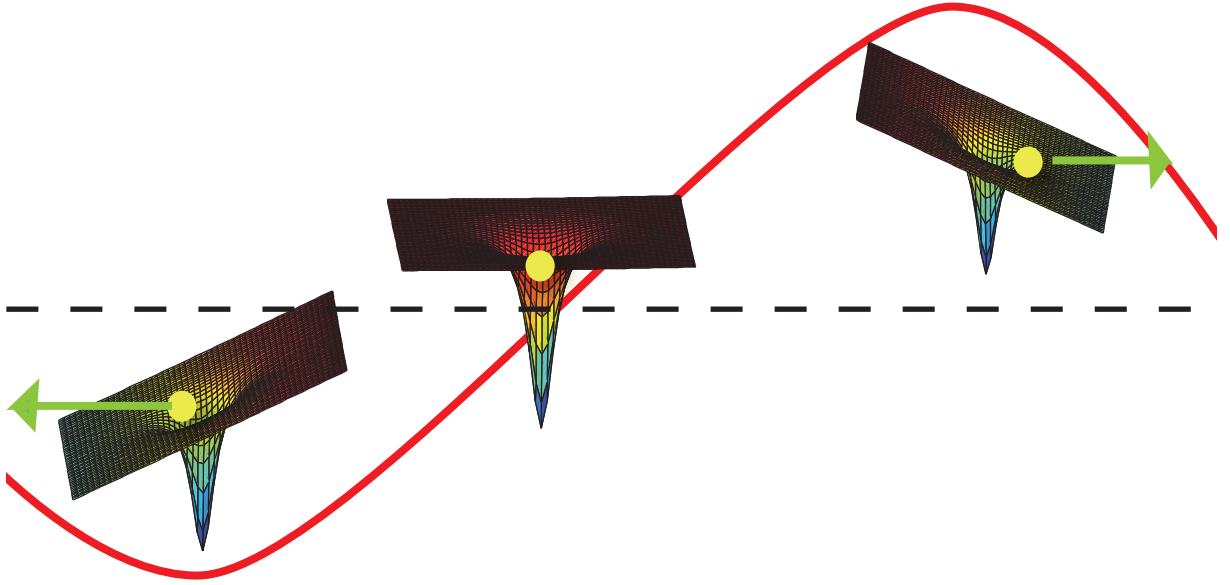


Figure 2.5: For intense fields, the potential corresponding to that of a linearly polarized plane wave field, i.e.  $-zE(t)$  is superimposed on to the 3D Coulomb Potential of the ion core. At the peak of the electric field, the ionic potential is suppressed such that the electron can tunnel through the barrier formed by the combined potential. This process can repeat itself at every maxima of the field (red curve), thereby giving rise to Electron Wave Packets (EWPs) at the maxima (absolute).

the formation of an outgoing Electron Wave Packet (EWP) repetitively, at the peak values of the electric field (Fig. 2.5).

The interaction of the electron in the continuum with the laser field can then be considered using the classical Newton's equations of motion. Neglecting the influence of the atomic potential and of the magnetic field (a good approximation for non-relativistic field intensities), the acceleration of the electron is given by,

$$\frac{d\vec{p}(t)}{dt} = -\vec{E}(t) \quad (2.26)$$

So that

$$\vec{p}(t) = - \int_{t_0}^t \vec{E}(t') dt' \quad (2.27)$$

where  $\vec{p}(t_0)$  is taken to be zero, i.e., the electron emerges into the continuum at time  $t_0$ , with no initial momentum. Considering only linearly polarized fields,  $\vec{E}(t) = \hat{z}E(t)$ , the final momentum of the electron in this model has only the  $z$  component, so we can drop the vector notation. Specifically for a linearly polarized electric field  $E(t) = E_0 \sin \omega t$ , we

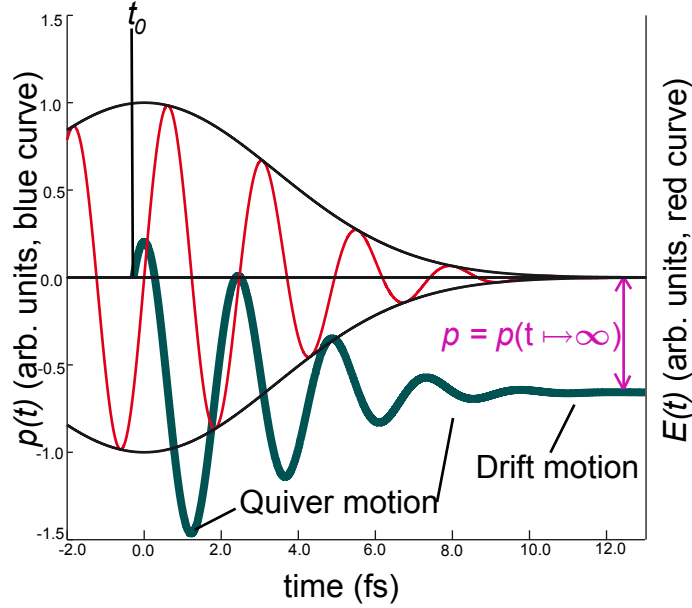


Figure 2.6: The instantaneous momentum for an electron born at time  $t_0$ , calculated through the classical equations of motions. The electron is driven back and forth by the oscillating field, while finally ending up with a constant drift momentum at the end of the pulse.

obtain the instantaneous momentum of the electron as,

$$p(t) = \frac{E_0}{\omega} (\cos \omega t - \cos \omega t_0) \quad (2.28)$$

It is clear to see that  $p$  has two components, a constant drift term, and a time varying 'quiver' term (Fig. 2.6). Since real laser pulses have a finite duration, we can formally set  $E(t \rightarrow \infty) = 0$ , so, when we measure at the detector, the drift momentum alone remains,

$$p = p(\infty) = -\frac{E_0}{\omega} \cos \omega t_0 \quad (2.29)$$

Further,

$$E(t) = -\frac{1}{c} \frac{\partial}{\partial t} A(t), \quad (2.30)$$

$$A(t_0) = -c \int_{-\infty}^{t_0} E(t') dt' = c \frac{E_0}{\omega} \cos \omega t_0 \quad (2.31)$$

Hence, in general, we may write

$$p + \frac{A(t_0)}{c} = 0 \quad (2.32)$$

To summarize the semi-classical treatment of tunneling ionization detailed above, the ionization probability at a certain time  $t_0$  depends on the electric field  $E(t_0)$ , while the final drift momentum depends on the vector potential at the time of birth,  $A(t_0)$ . The electron is preferentially ionized at the peak of the electric field, where the vector potential is zero, leading to zero drift momentum. The maximum momentum,  $p_{max} = E_0/\omega = 2\sqrt{U_P}$  is reached for electrons tunneling out at the zero crossing of the electric field, i.e. for  $\omega t_0 = n\pi, n = 0, 1, 2, 3, \dots$ , where the ionization probability is the least. Thus, one must expect the distribution of electron energies to have a peak at  $E_e = 0$  and then a rapid drop off for the number of electrons with increasing photoelectron energy. The first experimental observations for ATI in the tunneling regime indeed agree with the model [Cor89].

However, even for quite intense IR fields, the electron energy spectrum is not a monotonic distribution [Aug89, Mev93, Rud04], but does exhibit peaks which correspond to the absorption of an integer number of photons, i.e., with an energy spacing of  $\Delta E_e = \omega$ . Clearly, a classical description as presented above does not suffice, and one turns to one of three popular quantum-mechanical approaches

- Numerical solution of the time dependent Schrödinger equation (TDSE) [Kul87],
- Strong Field Approximation or related methods [Rie92],
- Floquet-type calculations [Dor90].

### 2.2.2 Strong Field Approximation (SFA)

Confining ourselves to the second case only [Rie80], the goal is to arrive at the transition amplitude,  $M_{fi}$ , for an electron in its ground state  $|\psi_i\rangle = \phi(\vec{r}) \exp(-i I_P t)$  to a state  $\psi_f$  in the continuum with a momentum  $p_f$  in the presence of a strong light field. That is,

$$M_{fi} = -i \int_{-\infty}^{\infty} dt \langle \psi_f | H_{int}(t) | \psi_i \rangle \quad (2.33)$$

where the interaction Hamiltonian is given by

$$H_{int}(t) = \frac{\vec{A}(t) \cdot (-i\nabla)}{c} + \frac{\vec{A}^2(t)}{2c^2} \quad (2.34)$$

which differs from eq. 2.9 as it now contains the term  $A^2(t)$ , which is no longer negligible in the strong field case. The eigenvalue solution of the interaction Hamiltonian is the well-known Volkov wave function describing the motion of an electron in an electromagnetic field. In particular,

$$H_{int} |\psi_v(t)\rangle = V_{int} |\psi_v(t)\rangle \quad (2.35)$$

where, the Volkov wave function for an electron with a momentum  $p$  is,

$$\psi_v(t) = \frac{1}{V^{1/2}} \exp \left[ i\vec{p} \cdot \vec{r} - i\frac{p^2 t}{2} - i \int_{-\infty}^t d\tau \left\{ \frac{\vec{p} \cdot \vec{A}(\tau)}{c} + \frac{\vec{A}^2(\tau)}{2c^2} \right\} \right] \quad (2.36)$$

which is a plane wave function<sup>4</sup>, with an additional Volkov phase factor,  $S(t)$ , which arises from the quiver of the electron in the field, and is given by<sup>5</sup>:

$$S(t) = i \int_{-\infty}^t d\tau \left\{ \frac{\vec{p} \cdot \vec{A}(\tau)}{c} + \frac{\vec{A}^2(\tau)}{2c^2} \right\} \quad (2.37)$$

The eigenvalue  $V_{int}$  is therefore, given by

$$V_{int} = \frac{\vec{A}(t) \cdot \vec{p}}{c} + \frac{\vec{A}^2(t)}{2c^2} \quad (2.38)$$

While the preceding equations are all exact, in the framework of the SFA, the electron in the continuum is assumed to no longer feel the atomic potential. So, the final state corresponds to the Volkov state, or, in other words,  $\psi_f(t) = \psi_v(t)$ . The transition amplitude therefore, transforms to

$$M_{fi} = -i \int_{-\infty}^{\infty} dt \langle \psi_v | H_{int}(t) | \psi_i \rangle, \text{ or,} \quad (2.39)$$

$$M_{fi} = -i \int_{-\infty}^{\infty} dt V_{int} \langle \psi_v | \psi_i \rangle \quad (2.40)$$

where, the second expression is obtained from the eigenvalue equation, eq. 2.35. Now we impose a separation of the space and time variables, to obtain

$$M_{fi} = -i \left\langle \frac{e^{i\vec{p} \cdot \vec{r}}}{V^{1/2}} | \phi_i(\vec{r}) \right\rangle \int_{-\infty}^{\infty} dt e^{i(p^2/2 - I_P)t} V_{int}(t) \exp \left( i \int_{-\infty}^t d\tau V_{int}(\tau) \right) \quad (2.41)$$

The above equation can be simplified through integration by parts [Rie80] to

$$M_{fi} = i \frac{\phi_i(\vec{p})}{V^{1/2}} \left\{ \frac{p^2}{2} - I_P \right\} \int_{-\infty}^{\infty} dt e^{i(p^2/2 - I_P)t} \exp \left( i \int_{-\infty}^t d\tau V_{int}(\tau) \right) \quad (2.42)$$

where,  $\phi_i(\vec{p})$  is the Fourier transform of the one-electron wave function in the ground state,  $\phi_i(\vec{r})$ . Now, considering a linearly polarized monochromatic plane wave of the form  $\vec{A}(t) = \hat{z} \frac{E_0}{\omega} \cos \omega t$  (see §2.6) for the vector potential, and assuming that the electron in the continuum has only momentum components along the  $z$  axis, the phase integral  $S(t)$  is reduced to,

$$S(t) = \frac{pE_0}{\omega^2} \sin \omega t + \frac{E_0^2}{8\omega^3} \sin 2\omega t + \frac{E_0^2}{4\omega^2} t \quad (2.43)$$

Further, using an infinite sum of generalized Bessel Functions  $J_n(u, v)$ , we can show that

$$\exp i(u \sin \vartheta + v \sin 2\vartheta) = \sum_n^{\infty} e^{in\vartheta} J_n(u, v) \quad (2.44)$$

<sup>4</sup>normalized by the volume element  $V$

<sup>5</sup>One easily recognizes that this is exactly the classical action of an electron in an electromagnetic field

We recognize the last term in eq. 2.43 is nothing but the ponderomotive energy  $U_p$ . Now, gathering the terms outside the integral in 2.42 into a single term  $C(p)$ , the transition amplitude becomes

$$M_{fi} = C(p) \sum_n^{\infty} J_n \left( \frac{pE_0}{\omega^2}, \frac{E_0^2}{8\omega^3} \right) \int_{-\infty}^{\infty} dt e^{i(p^2/2 + U_p - I_P + n\omega)t} \quad (2.45)$$

Now, the integral is in fact the definition of a  $\delta$  function peaking at  $p^2/2 + U_p - I_P + n\omega$ . So the final expression for the SFA transition amplitude is given by

$$M_{fi} = C(p) \sum_n^{\infty} J_n \left( \frac{pE_0}{\omega^2}, \frac{E_0^2}{8\omega^3} \right) \delta \left\{ \frac{p^2}{2} + U_p - I_P + n\omega \right\} \quad (2.46)$$

which leads to the physical interpretation that the transitions to continuum states which are given by the electron energy  $E_e = p^2/2 = U_p - I_P + n\omega$  are the only ones possible. Clearly, the electron energy spectrum would show peaks which are separated by one photon in energy,  $\Delta E_e = \omega$ , i.e. the ATI peaks!<sup>6</sup>

In the discussion above, implicit was the fact that the external field is an intense plane monochromatic wave, which is, however, not physically realizable. In experiments, such intense fields are generated from infrared (IR) laser sources, which are pulsed, and thus, can concentrate a large number of photons in ultrashort time durations, of the order of a few femtoseconds to picoseconds, through schemes known as Mode-Locking [Bra00]. Mathematically such short pulses can be represented through the Slowly Varying Envelope Approximation (SVEA) as

$$E(t) = E_0(t) \sin \omega t \quad (2.47)$$

where a slowly varying envelope function  $E_0(t)$  modulates the rapidly oscillating part, such that most of the energy of the field is confined in time to a duration  $\delta t$ . For example, for a Gaussian envelope  $E_0(t) = E_0 \exp(-\frac{t^2}{2T_0^2})$ , the field has a peak value of  $E_0$  at  $t = 0$ , which exponentially falls to half its value for  $t = \pm 1.18T_0$ , so that the field has a Full Width at Half Maximum (FWHM),  $\delta t = 2.36T_0$ .

Nevertheless, the physical interpretation of eq. 2.46 is approximately valid even for pulses which have an intensity FWHM of  $\sim 25$  fs, corroborated by the experiments of Rudenko *et al* [Rud04]. Rigorously, however, no elegant analytical expressions can be obtained for the general case of a pulsed laser field, and solutions to 2.42 have to be found numerically. Alternatively, one uses the so called saddle point analysis (method of steepest descent) to arrive at an approximate expression, which reduces the computation time and also allows for an intuitive explanation [Bec02, Mil06].

In the saddle point method, one recognizes that the exponential terms (the phase terms) in the integrand of 2.42 would lead to rapid oscillations of the integrand so that only points where the phase term is stationary would contribute to the final integral. These points of

<sup>6</sup>Note that the terminology of ATI peaks is still followed in the intensity regime  $\gamma \ll 1$  (Keldysh parameter) or  $\approx 1.10^{14} - 5.10^{14} \text{W/cm}^2$ , which is at the interface of the tunneling and multiphoton regimes

stationary phase ( $t_s$ ) are easily found by setting the first derivative of the phase to zero i.e.,

$$\frac{d}{dt} \left\{ \left( \frac{p^2}{2} - I_P \right) t + S(t) \right\}_{t_s} = \frac{1}{2} \left[ p + \frac{A(t_s)}{c} \right]^2 - I_P = 0 \quad (2.48)$$

The point of interest here is that though, in general,  $t_s$  are complex numbers, when we set  $I_P = 0$ , we arrive at 2.32, the Newton's equation of motion. So we come to the most important interpretation of the stationary phase equation: the quantum paths which provide the main contribution to the transition matrix element converge to the classical trajectories of the electron in the laser field. So now, the integral reduces to a sum over the stationary points which have a positive imaginary part,

$$M_{fi} = C(p) \sum_{t_s} \left( \frac{2\pi i}{S''(t_s)} \right)^{1/2} e^{i((p^2/2 - I_P)t_s + S(t_s))} \quad (2.49)$$

The elegant expression above offers the interpretation that to find an electron in the continuum with a momentum  $p$ , there are many ionization pathways, which can be parametrized by the stationary points  $t_s$ , and their corresponding stationary phases  $S(t_s)$ . To a good approximation, these stationary points can be obtained as the solutions to the classical trajectories eq. 2.32. So the probability of observing an electron with a momentum  $p$ , which is  $\propto |M_{fi}(p)|^2$ , is the superposition of the contributions of interfering trajectories ( $t_s$ ). Now, for a 'long' pulse, with many cycles within the FWHM, the periodicity ensures that for a given  $p$ , stationary phase solutions are repeated every cycle of the pulse i.e.,  $t'_s = t_s + 2n\pi/\omega$ . So it is easy to see that interference of the contributions from different periods (which goes as the term  $\sim \cos(2 \cdot \frac{p^2}{2} \cdot \frac{2\pi}{\omega})$ ) restricts the observance of electrons to those with momenta  $p^2/2 = N\omega$ , once again the ATI peaks! We neglected to mention here that even within a single cycle, two phases  $\omega t_1$  and  $\omega t_2$  which are symmetrically placed about a zero crossing, will lead to the same momentum. So the final probability amplitude will also have contributions from the sub-cycle interference of these two trajectories. However, for a multi-cycle pulse, much in the fashion of a multiple slit experiment, where the details of the intra-slit interference is overridden by the interference between the multiple slits, the sub-cycle interference is subsumed in the pattern of the ATI peaks. But, if the laser field is made so short that only a single-cycle of the pulse effectively contributes to the ionization, then we may expect these interferences to show up analogous to diffraction from a single slit. In fact, Chap 4 is a report on what we believe, is the experimental observation of these sub-cycle interferences, and therefore, will be dealt with in more detail there.

### 2.2.3 Rescattering, higher order ATI and high harmonic generation

Coming back to the Newton's equation of motion, we see that they impose a classical limit on the maximum energy the electron can gain from the laser field,  $E_e^{max} = 2U_p$ . However,

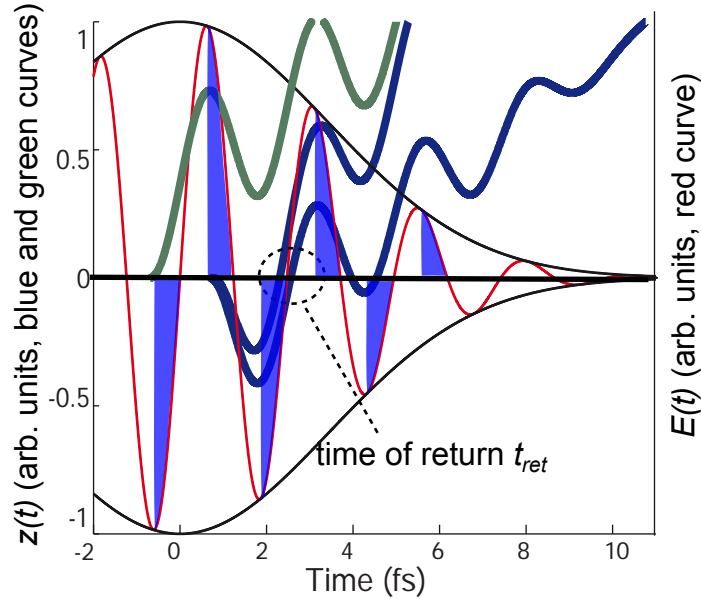


Figure 2.7: The electron in the continuum is driven back and forth by the field such that it follows the classical trajectories illustrated above. The trajectories,  $z(t)$ , of the electron born at different times,  $t_0$ , in the field can be divided into returning trajectories (blue) and non-returning trajectories (green) depending on whether or not there exists a time  $t_{ret}$ , such that  $z(t_{ret}) = 0$ . It is easy to see that returning trajectories exist for electrons born in an odd quarter-cycle of the field, i.e.,  $(2n + 1)\pi/\omega \leq t_0 \leq 2n\pi/\omega$  (shaded light blue)

in experiments [Yang93, Pau94a], electrons with energies greater than  $2U_p$  were observed, identified in the photoelectron spectrum as a plateau like structure with a cutoff at  $\sim 10U_p$ . An accompanying phenomenon is that when atoms interact with a strong laser field, they emit radiation in multiples of the incident frequency, known as High Harmonic Generation (HHG), where orders of 100 and more were observed [Fer88, Hui92]. The underlying physics behind both observations can easily be understood using the so-called three-step model, developed by P. B. Corkum [Cor93], and by J. L Krause *et al.*[Kra92].

As before, the electron 'appears' in the continuum at a certain time  $t_0$  through the tunneling process. Now the electron is driven back and forth in space by the laser field as shown in Fig. 2.7. Depending on its time of birth  $t_0$ , there is a possibility that the electron can 'revisit' the position of the parent ion within the first laser period. The electron has then the following possibilities:

- it is elastically rescattered off the ion core, or
- it recombines with the parent ion to release a high energy photon, or
- it scatters inelastically off the ion, depositing enough energy in the ion to further

excite or ionize it.

The first case leads to the observation of higher order ATI (HATI) [Bec02], the second to High Harmonic Generation (HHG) [Fer88], and the third leads to phenomena such as non-sequential double or multiple ionization [Bec05], as illustrated in Fig. 2.8.

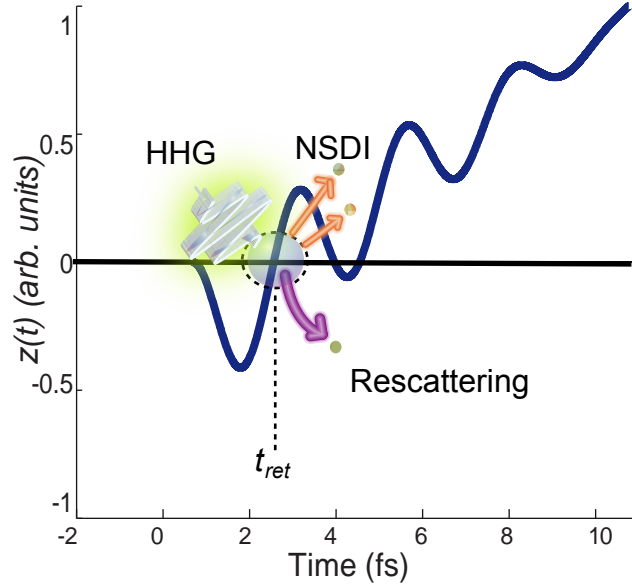


Figure 2.8: The returning electron may recombine with the parent ion, to give off its energy as a high energy photon in HHG. Alternatively it can rescatter elastically off the ion in any direction, called HATI, or scatter inelastically and for e.g. remove one or more electrons, in the process called non-sequential multiple ionization.

As before, in the first approximation, we may consider the electron in the laser field using only classical mechanics. Starting from the equations of motion (2.32) the instantaneous displacement of the electron along the laser polarization axis in general is given by

$$z(t) - z(t_0) = \int_{t_0}^t p(t') dt' = -\frac{1}{c} \left( (t - t_0) A(t_0) - \int_{t_0}^t dt' A(t') \right) \quad (2.50)$$

Again with the laser described as a linearly polarized field  $E = E_0 \sin(\omega t)$ , and considering the electron to be at the position of the ion core at its time of birth  $z(t_0) = 0$ , we get

$$z(t) = -\frac{E_0}{\omega} \left( (t - t_0) \cos \omega t_0 - \frac{1}{\omega} (\sin \omega t - \sin \omega t_0) \right) \quad (2.51)$$

Sketched in Fig. 2.7 are the instantaneous positions of the electron for different times of birth. Clearly the condition for the electron to return to the site of its parent ion is

$z(t_{ret}) = 0$ , which occurs whenever there is a zero crossing of the field within the half-cycle of the birth of the electron, for example in the light blue area of Fig. 2.7. The electron born within these areas returns to the ion with varying energies

$$E_{ret} = \frac{1}{2}p(t_{ret})^2 = \frac{1}{2c^2} (A(t_{ret}) - A(t_0))^2 = \frac{E_0^2}{2\omega^2} (\cos \omega t_{ret} - \cos \omega t_0)^2 \quad (2.52)$$

which is maximum when  $\omega t_0 = 108^\circ$  and  $\omega t_{ret} = 342^\circ$ , with  $E_{ret}^{max} = 3.17U_p$  [Cor93]. A radiative recombination of the electron into the ground state of the parent ion would therefore, yield a photon with a maximum energy given by the classical cut off law

$$E_{cut\ off} (HHG) = 3.17U_p + I_P \quad (2.53)$$

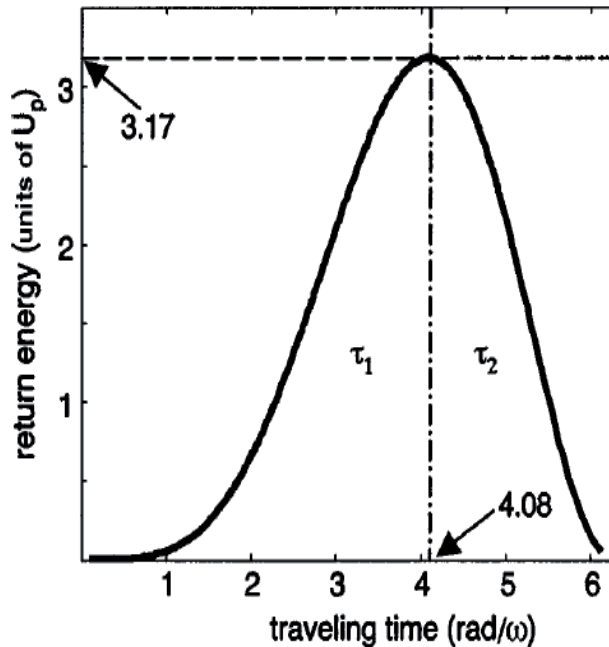


Figure 2.9: Each of the returning trajectories (blue in Fig. 2.7), can be associated with a traveling time  $\tau = t_{ret} - t_0$ , and corresponding return energy. Plotted is the return energy as a function of the traveling time. The maximum return energy has a traveling time of  $1.3\pi/\omega$ . For all other return energies, there are two trajectories:  $\tau_1$ , the "short" trajectory, and  $\tau_2$ , the "long" trajectory. (Adapted from [Lin03])

For energies lower than the cut off, two different solutions exist. Introducing a 'traveling time'  $\tau = t_0 - t_{ret}$ , these two trajectories can be distinguished as short ( $\tau_1$ ) and long trajectories ( $\tau_2$ ) (Fig. 2.9 and Fig. 2.10), the importance of which in the generation of high harmonics will be discussed in the following section.

If the returning electron is elastically back scattered, due to its interaction with the ion, then its momentum just after scattering is reversed in direction,  $p(t_{ret}^+) = -p(t_{ret}^-)$ .

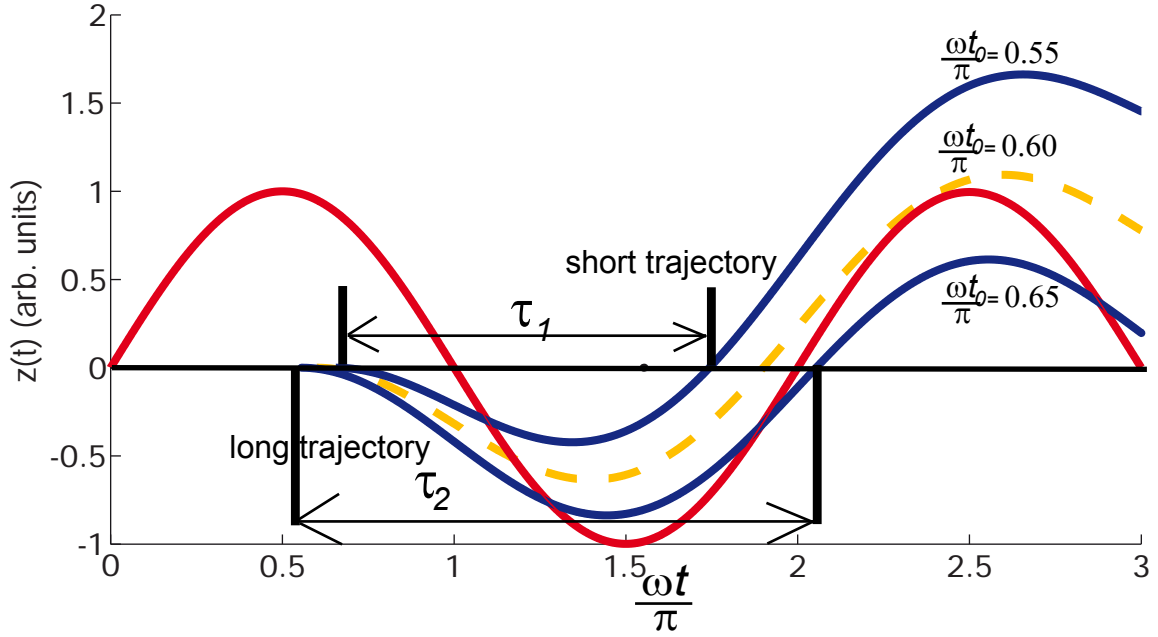


Figure 2.10: Plot of trajectories leading to different return energies. The electron born at the phase  $\omega t_0 = 0.6\pi$  (broken yellow curve) returns to the parent ion at the phase  $\omega t_0 = 1.9\pi$ , with the maximum energy,  $3.17U_p$ . For a return energy of  $2.65U_p$ , the long and short trajectories are illustrated as blue curves.

The electron now is further accelerated by the laser field, so that it ends up with a drift momentum  $p = -p(t_{ret}) - A(t_{ret})/c = -1/c(2A(t_{ret}) - A(t_0))$ . This leads to the observation of electrons with higher energies (HATI). The maximum energy of the observed photoelectrons is therefore, when  $\omega t_0 = 105^\circ$  and  $\omega t_{ret} = 352^\circ$ , yielding the cut off for the ATI electrons as

$$E_{cut\ off} \text{ (ATI)} = 10.007U_p \quad (2.54)$$

## 2.3 High Harmonic Generation (HHG)

In the previous section the generation of high energy photons was seen as a strong field process, wherein the electron can be steered by the laser to recombine with the parent ion, leading to HHG. The high harmonics spectrum is generic [Fer88], consisting of equidistant peaks, which are odd harmonics of the driving laser frequency ( $\omega$ ), with a rapid fall in the intensity of the lower order harmonics, followed by a plateau, and finally a sharp decrease of intensity close to the classically predicted cut off at  $3.17U_p + I_P$ . Depending on the target gas used, different regions of the XUV spectrum can be accessed. Clearly, higher photon energies can be reached, if the ionization potential is high. So He ( $I_P=24.6$  eV), and Ne ( $I_P=20.2$  eV) are the choice in experiments where photon energies up to 460 eV have been

reached [Cha97]. However, the trade off with higher ionization potential is obviously the lower efficiency of the process [Hui92]. So a compromise can be found with generation of lower photon energies, ( $\sim 40$  eV, Ar), ( $\sim 30$  eV, Kr), ( $\sim 20$  eV, Xe) but at a higher photon flux.

The production of high-energy photons in the XUV region of the electromagnetic spectrum, with a reasonable and flat conversion efficiency ( $\sim 10^{-5}$ ) in the plateau make the HHG process a viable candidate for a table-top, ultrashort, coherent source of XUV photons, with durations of a few femtoseconds, or possibly even sub-femtoseconds. Since a part of the work presented here was utilizing such a source, in this section we will develop a few of the concepts related to high harmonics generation.

### 2.3.1 Quantum orbits

Returning to the recollision model presented above, it is clear to see that in the time domain, the recollision process is repeated every half cycle, such that photonic wave packets are emitted twice every cycle, predominantly near the zero-crossing of the driving field. In the Fourier domain, this manifests as equidistant peaks separated by twice the frequency of the driving laser field. Implied in this approach to treating HHG is a sub-cycle time structure [Dim03] to the radiation, which can be exploited to create Attosecond Pulse Trains (APTs) [Mar05] and single attosecond pulses [Bal03]. The recollision model also provides a basis for developing a theory for HHG [Lew94], which we shall briefly consider now.

Formally the electron is considered in the framework of the SFA theory described in 2.2.2, with the exception that the free electron is allowed to interact with the ion. The observable of interest is the radiated harmonic spectrum, which can be obtained most simply through the Fourier transform of the time dependent dipole moment. In the SFA approach, this dipole moment has a form which intuitively captures the three-step model:

$$D(t) = -i \int_{-\infty}^t dt' \int dp \underbrace{d_x [p + A(t')/c] \cdot E(t')}_{\text{Ionization}} \cdot \underbrace{e^{iS(p,t',t)}}_{\text{Propagation}} \cdot \underbrace{d_x^* [p + A(t)/c]}_{\text{Recombination}} \quad (2.55)$$

where

$$S(p, t', t) = \int_{t'}^t dt'' \frac{(p + A(t'')/c)^2}{2} - I_P \quad (2.56)$$

$d_x$  is the dipole matrix element for ionization introduced earlier in another form in 2.41 and  $d_x^*$  is the complex conjugate denoting recombination to the ground state. Assuming a linearly polarized monochromatic driving field, the periodicity of the field allows us to consider emission from a single half cycle. The time dependent dipole moment can finally be Fourier transformed to

$$D(\Omega) = -i \int_0^{\pi/\omega} dt \int_{-\infty}^t dt' \int dp d_x [p + A(t')/c] \cdot E(t') \cdot e^{iS(p,t',t)} \cdot d_x^* [p + A(t)/c] \quad (2.57)$$

where  $\Omega$  is the frequency of the emitted radiation. It is clear to see that for each frequency component, there are an infinite number of contributions in the integral. Again using a

stationary phase analysis it is easy to show, that for high laser intensities (large values for  $A(t)$ ) only a limited number of paths, for which the phase term,  $S(p, t, t')$  is stationary, contribute. Representing these quantum orbits, which correspond to the classical trajectories eq. 2.51, through the traveling time as  $\tau_n = t_n - t'_n$ , the resulting spectrum can therefore, be written using a sum over contributions  $D_n$  from the quantum orbits,

$$D(\Omega) = \sum_n D_n(\Omega) \quad (2.58)$$

where, associated to each quantum orbit  $\tau_n$ , is the dipole amplitude and phase term, which have an implicit dependence on the intensity of the laser field [Bel98, Sal02].

$$D_n(\Omega) = A_n(\Omega) \exp(i\Phi_n(\Omega)) \quad (2.59)$$

Finally, a rigorous application of the stationary phase method similar to §2.2.2 can be used to show that the spectrum indeed has peaks separated by  $2\omega$ , also retrieving the generic shape of the HHG spectrum.

### 2.3.2 Phase matching

The single atom response detailed above predicts that an atom driven by an intense laser field emits harmonics of the laser frequency. But in order to utilize this property to engineer an effective source for high energy photons with spatial and temporal properties similar to that of a laser, it is important to consider the collective effects associated with the HHG process, in particular, the phase relationship between the emitted radiation and the driving radiation [Hui90, Bal93]. For example, a single atom source behaves as an oscillating electric dipole aligned along the polarization axis of the driving laser and can therefore, be expected to emit radiation in both the forward and backward direction, with respect to the propagation direction of the driving laser. On the other hand, in a gas target, the harmonics are observed to emerge collinear with the driving laser field (and in the forward direction) as a result of the interference of the radiation from different atoms adding up constructively only in the forward direction [Pro97].

In practice, the harmonics are generated by focusing a laser beam on a gas target, which could be an effusive jet or confined in a gas-cell (Fig. 2.11), such that the medium has an effective interaction length of  $L$ . Phase matching is achieved, leading to maximum transfer of the laser energy into the harmonic radiation, when the field strength for the  $q$ -th harmonic field,  $E_q$  is in phase with the  $q$ -th order source polarization  $P_q$ . After a short distance  $L_{coh}$ , the two fields are out of phase by  $\pi$ , and the energy of the harmonics is returned to the fundamental field. The phase mismatch for the  $q$ -th harmonic  $\Delta kz$  for the field traversing a distance  $z$  in the medium is given by the sum of the contributions from mainly three effects [Pro97]:

1. The dispersive phase mismatch resulting from the frequency dependence of the refractive index of the medium, given by  $\Delta k_{disp}z = q\omega(n_q - n_0)cz$ , where  $n_q$  is the refractive index for the  $q$ -th harmonic and  $n_0$  is the refractive index for the fundamental.

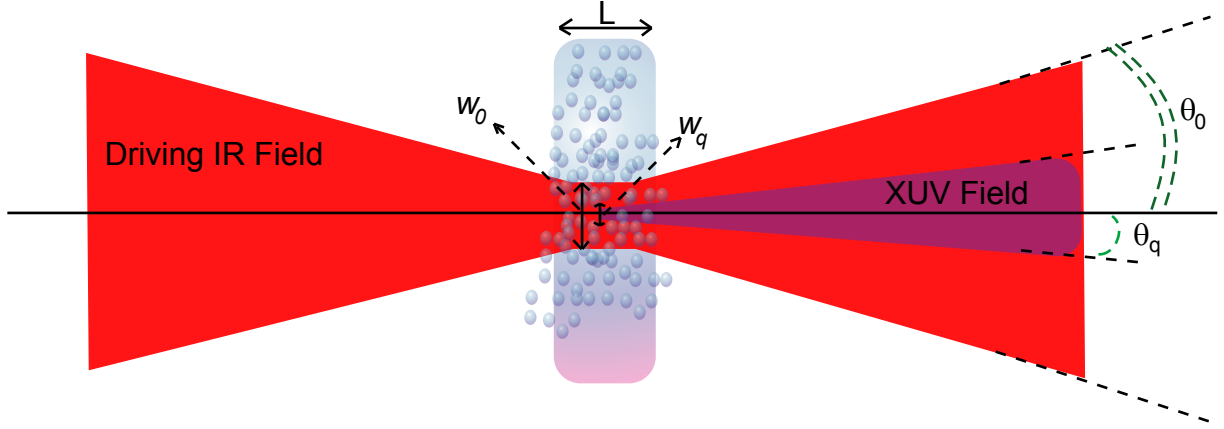


Figure 2.11: The geometry for HHG in gaseous media. The interaction length  $L$ , is related to the physical length of the medium along the propagation direction and the ionization volume of the laser field which generates the harmonics. The harmonic  $\omega_q$  generated derives its far field divergence angle,  $\theta_q$  from that of the driving laser field,  $\theta_0$

2. The Gouy phase shift relative to a plane wave for a Gaussian beam passing through the focus  $\Delta k_{Gouy}z = 2(1 - q)/(k_0 w_0^2)z$ , where  $k_0 = 2\pi/\lambda$  is the wave vector and  $w_0$  is the beam waist at the focal spot.
3. The dipole phase  $\Delta k_{dip}(z)$ , which originates from the accumulated phase during the excursion of the electron in the laser field can be approximated for each quantum orbit by the product of the ponderomotive energy and the traveling time as  $-U_P \tau_n$  [Sal02]. The dipole phase varies along the propagation direction  $z$ , through its intensity dependence.

For a given  $L_{coh} = \pi/\Delta k$ , the total harmonic signal at the end of the medium increases monotonically with the length of the interaction region,  $L$ , reaching a maximum when  $L = L_{coh}$ . Therefore, the signal is optimum when  $L_{coh}$  is so maximized to be equal to the interaction length. The interplay of the above three effects, dependent on the pressure and width of the target gas, the laser intensity and the focusing conditions therefore, determines the flux of the harmonic photons emitted. For example, using loose focusing, the focal spot can be increased to minimize  $\Delta k_{Gouy}$ , also leading to lower intensity, and lower dipole phase mismatch. In addition, by focusing the laser before the medium, the change in sign of Gouy-phase can be avoided and a favorable position found such that  $\Delta k_{Gouy}L$  partly cancels out  $\Delta k_{disp}(L)$ . Furthermore,  $\Delta k_{disp}$  has components from the

refractive index of the atomic medium and the plasma created by ionization. In general, for the high harmonics the medium (usually a rare gas) has a small negative dispersion, while the plasma is positively dispersive. So for an optimum laser intensity the plasma density can be reduced such that the two effects cancel out to minimize  $\Delta k_{disp}$ . Finally, in the experiment, an iterative adjustment of the parameters leads to an optimum flux of the harmonics with coherent temporal and spatial properties derived from the driving laser field [Pro97]:

$$w_0^{(q)} = \sqrt{q}w_0/\sqrt{p} \quad (2.60)$$

$$\theta_q = \sqrt{q}\theta_0/\sqrt{p} \quad (2.61)$$

$$\tau_q = \tau_0/\sqrt{p} \quad (2.62)$$

where,  $w_0^{(q)}$  is the minimum beam waist size at the focal spot of the  $q$ -th harmonic;  $\theta_q$  and  $\theta_0$  are the far field divergence angle for the  $q$ -th harmonic and the fundamental (Fig. 2.11);  $\tau_p$  and  $\tau_0$  are the pulse durations of the harmonic and the fundamental respectively. Finally  $p$  is the effective power and is less than  $q$  for the plateau harmonics. This is in contrast to the lower order harmonics, where,  $p = q$  as in the well-known nonlinear processes of Second Harmonic Generation (SHG) and Third Harmonic Generation (THG) [Boy03].

## 2.4 Attosecond Pulse Trains

The HHG spectrum spans from the ultraviolet region, where there is a rapid fall of the efficiency of generation, to the extreme ultraviolet (XUV) region, with a nearly constant efficiency for the harmonics (plateau), followed by a sharp cut off in the soft X-ray regime. This large bandwidth, especially in the plateau, in principle, should support very short pulses of durations less than a femtosecond. Of course, given that the spectrum has the form of sharp harmonic peaks, in the limit that the harmonics are synchronized, one would expect to see in the time domain a train of ultrashort pulses under a broad envelope. Indeed, even in the recollision picture [Ant96], since the laser-driven recollision, leading to bursts of photons, occurs in a very small time window every half-cycle [Din03], it raises the possibility of obtaining a train of pulses, with a single-pulse-duration which is a fraction of the half-cycle of driving laser field, i.e.. less than 1 fs (a single cycle for an 800 nm laser is 2.7 fs). However, the time structure of the harmonics which emerge directly from the target gas consists of broad, poorly contrasted, periodically occurring structures (left panel of Fig. 2.12). In this section, we therefore, consider the physics behind the techniques used to obtain Attosecond Pulse Trains (APT) from high harmonics.

Considering the HHG process, it is not so difficult to imagine why the time resolution is poor. Firstly, the harmonic signal is dominated by the lower order harmonics which are produced with an efficiency which is at least two orders of magnitude higher than that for the plateau harmonics. Since the mechanism involved in generating these harmonics is perturbative, it leads to a different intra-harmonic phase relationship than those for the plateau. This manifests as broad structures in the time domain, while the short time

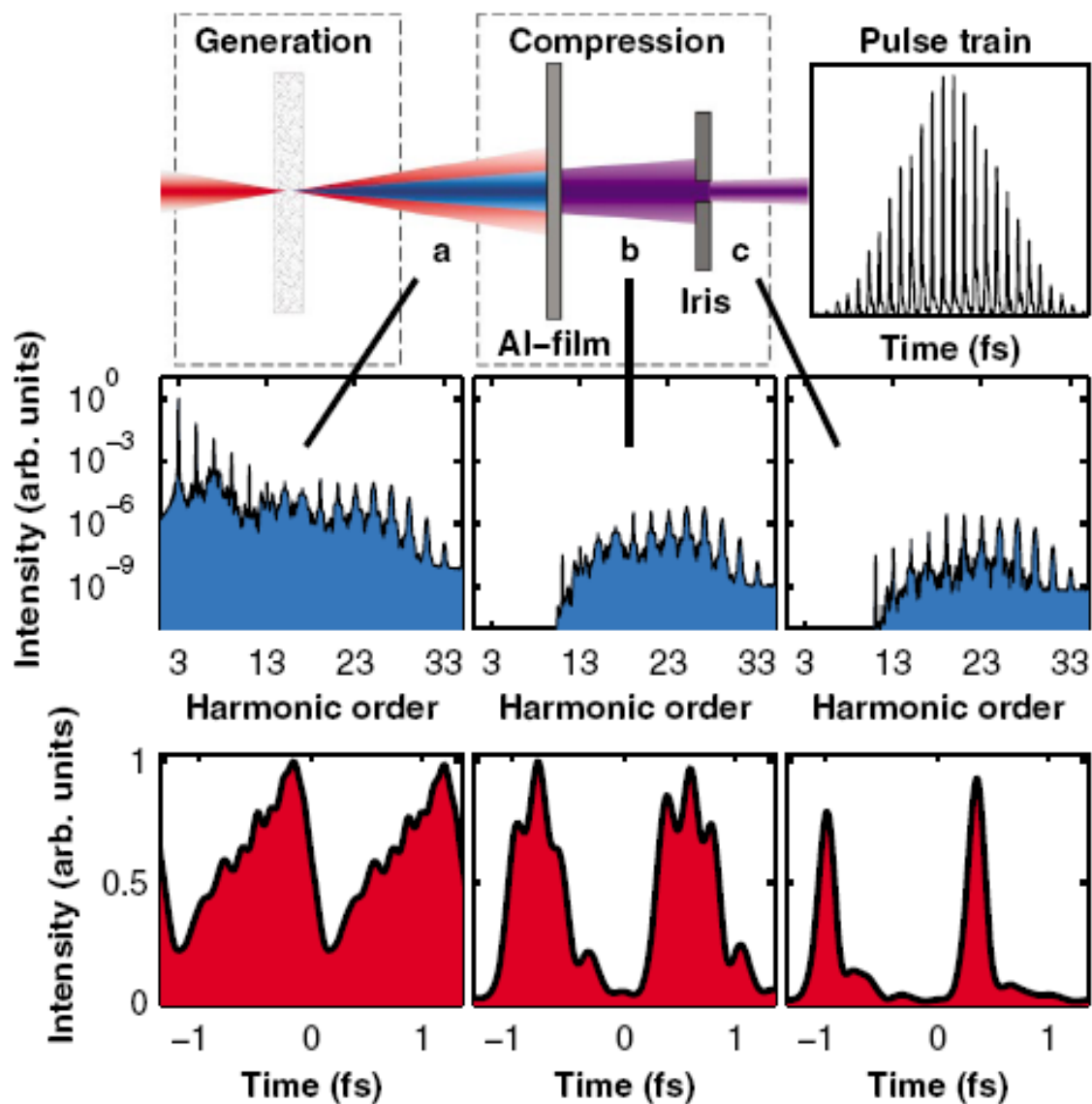


Figure 2.12: The generation of APTs from harmonic generation. Left: the time structure of the HHG radiation as seen in TDSE calculations (lowest panel) shows poor time resolution. Center: When the lower harmonics are suppressed through a thin Al filter, the ultrashort-time structure of the plateau harmonics shows up. Right: compression is finally achieved by using an aperture in the far field to filter out contributions of the long trajectories (see text). (Adapted from [Mar05])

structures of the plateau harmonics are hidden within this broad background. So the first step in obtaining ultrashort pulse trains is to spectrally filter the harmonics to suppress the lower order harmonics [Mar05, Mai04] (central panel of Fig. 2.12). For example, a thin ( $< 1\mu\text{m}$ ) aluminum foil [Gus07] with a lower spectral cutoff for photon energies below  $\approx 20$  eV is an effective filter for harmonics generated in Ar or Kr (Fig. 2.13a)).

Secondly, coming to the plateau harmonics, where the recollision picture is valid, it is clear from Fig. 2.9 that associated with each harmonic are two sets of trajectories, short and long, which have different phase behaviors with respect to the generating field. Furthermore, considering only one set of trajectories, say, the short trajectories (for example  $\tau_1$  in Figs. 2.9 and 2.10), one sees that the traveling time associated with the electrons generating high energy photons is greater than the traveling time for those producing lower energies. Therefore, the low-frequency components of the harmonic radiation arrive earlier than the high-frequency constituents and the pulse is said to have a positive 'atto chirp' [Joh06], within the time scale of one half-cycle period of the driving pulse. In addition, the intensity variation along a pulse leads to different traveling times for consecutive half-cycles, even for a single harmonic. The consequent chirp, which is on the time scale of the envelope of the driving pulse is termed as 'harmonic chirp' [Joh06].

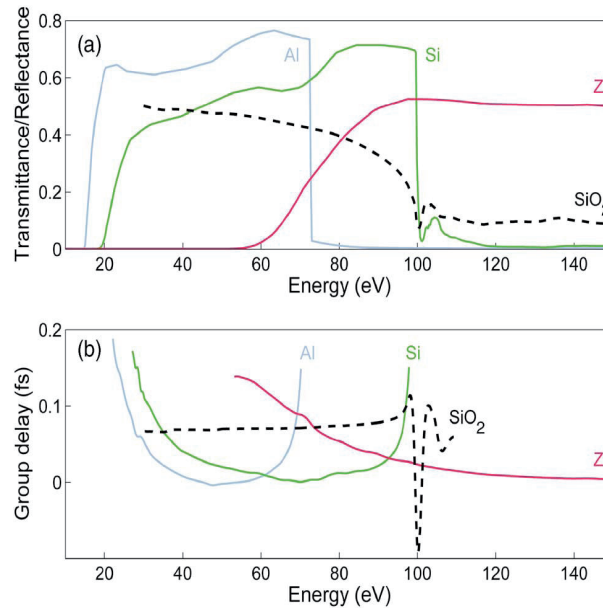


Figure 2.13: (a) The transmittance (reflectance for SiO<sub>2</sub>) as a function of photon energy of commonly used spectral filters to suppress the lower harmonics. (b) The corresponding dispersion curves show that in the spectral regions of interest, these filters also have a negative dispersion, which can be used to cancel out the positive dispersion of the 'atto chirp'. (Adapted from [Gus07])

In the light of the various phase-related effects that accompany the generation of plateau harmonics, a combination of techniques have to be used to achieve synchronization. For

example, phase matching can ensure that only one set of trajectories, the short trajectories, are propagated through the medium. As alluded to in §2.3.2, the  $z$ -dependent dipole phase is compensated for by the Gouy phase if the focal position is before the medium. This is, however, true only for the short trajectories, as for the long trajectories, the dipole phase ( $\approx U_P \tau_n$ ) is large and therefore, does not survive the phase-mismatch while propagating through the medium. Of course, a large enough radial phase component (associated with a focused Gaussian beam) may bring the  $\tau_2$  harmonics into phase-match in the off-axis region. Here again, the authors in [Bel98] show that the rapid variation of the dipole phase with the laser intensity leads to a strong curvature of the phase front and, therefore, a large divergence. Thus, the harmonics from long trajectories can be effectively filtered out through a simple aperture in the far field [Mar05, Mai04] (right panel of Fig. 2.12).

The final obstacle to obtain bandwidth-limited pulses from the plateau harmonics is the compensation for the atto and harmonic chirp. The latter, in general, can be achieved by using a positively chirped driving pulse [Joh06]. The compensation for the atto chirp has been effectively demonstrated [Mar05] by propagating the harmonics through a medium (or reflecting it off a surface) with negative dispersion in the relevant spectral region (Fig. 2.13(b)). For example, for the harmonics generated in Ar, a 600 nm Al filter, in addition to spectrally filtering the lower harmonics also provides the requisite negative dispersion to compress the harmonics to APTs with single pulse widths of 170 as corresponding to only 1.2 cycles of the carrier frequency ( $\approx 30$  eV) within the FWHM of the single pulse.

## 2.5 Two-colour, two-photon ionization of rare gases with APTs in the presence of an IR field

When HHG radiation is incident on a rare gas atom, the photoionized electron shares the same spectral properties as the incident radiation, except that the energy is reduced as compared to the photon energy by the ionization potential  $E_e = E_\gamma - I_P$ <sup>7</sup>. So the electron energy spectra also consist of sharp spikes with the same energy spacing as in the harmonics. In the time domain, the half-cycle period of the APT is replicated by a train of Electron Wave Packets (EWP) emitted for each of the single pulses of the APT.

The transition amplitude for the transition of an electron from the ground state to a momentum state  $p_f$  through interaction with an external field  $E_{XUV}(t)$  can be obtained through first order perturbation theory under the single active electron approximation to yield [Que05],

$$a(p_f) = -i \int_{-\infty}^{\infty} dt d(p_f) \cdot E_{XUV}(t) \exp(ip_f^2 t + I_P t) \quad (2.63)$$

where  $d(p_f)$  is the dipole matrix element and the final state is represented by a plane wave solution. The above equation immediately shows the direct relation between the XUV spectrum and the measured electron spectrum. If the amplitude of the dipole element

---

<sup>7</sup>Of course, since the HHG spectrum spans only up to the soft X-ray region, only the valence electrons are ionized, the inner electrons being left undisturbed.

$d(p_f)$ , which is related to the photoionization cross section of the target atom, depends on the ejected momentum  $p_f$ , then the XUV spectra and the electron spectra differ in amplitude. However, the photoionization cross sections for rare gas atoms are well-known, allowing the electron spectra to be corrected for this dependence. In addition, the spectra may differ by the atomic dipole phase, which can be neglected or calculated from theory when such corrections are necessary. Since the measured photoelectron spectrum in single photon ionization is proportional to the modulus squared of the transition amplitude, all information of the spectral phase of the XUV field is lost. In other words, the spectral phase variation is contained in the temporal variation of the spectrum, i.e., the arrival of different spectral components at different times. Since the photoelectron spectrum is measured with a time integrating detector, the phase information is lost.

The problem then reduces to designing a time non stationary filter, which introduces a time-dispersion of the spectrum, which can be inverted to obtain the spectral components at different times. For APTs, this can be achieved by considering the two-colour XUV-IR photoionization process. Depending on the delay between the XUV and the IR field, the photoelectron spectrum is modulated, and the delay-dependent energy spectrum can be inverted to obtain the spectral phase. In the following subsections we briefly introduce the physics involved in the ionization of rare gas atoms with XUV pulses, in the presence of an intense ( $10^{12}$  to  $10^{14}$  W/cm<sup>2</sup>) IR laser field, to understand the techniques for characterizing ultrashort XUV pulses.

### 2.5.1 Semi-classical description

Given the extremely large difference in the energies of the XUV and the IR photons, we are justified in treating the two-colour process as a two-step process: the photoionization by the XUV photon, followed by acceleration of the photoelectron in the laser field. The acceleration by the XUV field is negligible since with contemporary HHG sources, the maximum intensities one may expect are only about  $10^8$  to  $10^9$  W/cm<sup>2</sup>. Furthermore, on a more fundamental note, the ponderomotive energy, scales inversely with the frequency squared (eq. 2.24), therefore, for the XUV, the ponderomotive energy is negligible as compared to the IR field, even for comparable intensities.

So, the electron is ejected into the continuum at a time  $t_0$  by the XUV field, with an initial momentum  $p_0$ . This is in contrast to the two-step ionization by a strong IR field, where the electron in the first step tunnels out with near zero initial momentum. Once again for an IR field  $E = E_0 \sin(\omega t)$ , with the vector potential given by  $A(t) = cE_0/\omega \cos \omega t$ , the momentum of the electron is given by

$$p(t) = \frac{E_0}{\omega} (\cos(\omega t) - \cos(\omega t_0)) + p_0 \quad (2.64)$$

which can be generalized as

$$p(t) = p_0 + A(t)/c - A(t_0)/c \quad (2.65)$$

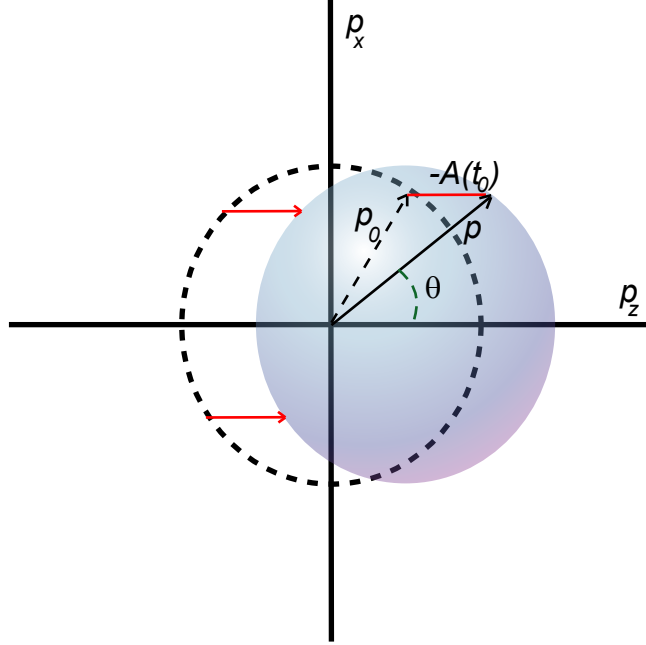


Figure 2.14: Illustration of streaking. The momentum sphere associated with single-photon ionization is shifted, or 'streaked', depending on the time of birth of the electron,  $t_0$ , along the polarization axis of the laser, by the term  $-A(t_0)$ .

where the quiver term  $A(t)/c$  integrates out to zero at the end of the pulse, so that the electron is detected with a momentum which is the initial momentum  $p_0$  modified by the vector potential of the IR field  $A(t_0)$ . To visualize this, consider Fig. 2.14. Plotted is the classical 2D momentum distribution  $p = p(t \rightarrow \infty)$ . On the horizontal is the momentum component along the polarization axis of the laser, the vertical axis is the momentum component perpendicular to the polarization. When there is no laser field, classically, the electron is confined in momentum space to the surface of a sphere with a radius  $|p_0|$ , illustrated as a dotted circle in Fig. 2.14. In the presence of the laser, depending on  $t_0$ , the momentum sphere is shifted by the vector potential, and therefore, oscillates along the polarization axis with  $t_0$  (streaking). The time-of-birth dependent energy for an electron observed along the polarization axis is given by [Que05, Joh05]

$$E_e = W_0 + 2U_P \cos^2 \omega t_0 + (8W_0 U_P)^{1/2} \cos \omega t_0, \quad (2.66)$$

where  $W_0 = E_\gamma - I_P$  is the initial energy of the electron when it enters the continuum at  $t_0$ . Within the duration of the XUV pulse, different temporal slices of the Electron Wave Packet (EWP) will experience different vector potentials. Consequently, the momentum distribution will be broadened and shifted along the polarization axis, as function of time of birth. While the semi-classical model provides an intuitive basis to understand the physics behind the process, it fails to account for interferences between EWPs born at different times leading to the same electron energy. A more intuitive understanding for

the modulation of the spectra can be obtained from the photon picture illustrated in Fig. 2.15, where the photoelectron in the continuum can resonantly exchange energy with the IR field in quanta of one or more IR photons [Ven96]. Therefore, additional peaks, termed as sidebands, appear in the photoelectron spectra exactly between the peaks of the fundamental harmonics.

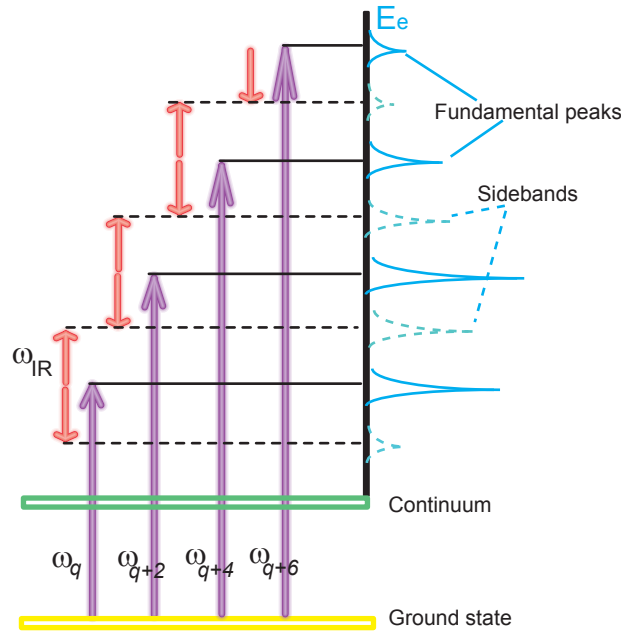


Figure 2.15: In the low intensity regime sidebands appear in the electron energy spectra between the fundamental peaks from the ionization by the harmonics as a result of absorbing or emitting one IR photon of energy.

## 2.5.2 Sideband oscillations

In two-color ionization experiments, when the XUV pulses within the envelope of the APT are longer or comparable in duration to the half-cycle ( $\sim 1.3$  fs), and the XUV-IR delay  $\tau$  is varied, the sidebands show a monotonic rise and fall in their intensity on the time scale of the envelope of the pulses. But as the single pulse width reduces,  $I_{SB}(\tau)$  begins to show modulations on the delay time scales of few hundreds of attoseconds [Joh05, Pau01]. These modulations can be explained if we consider the fact that in a low-intensity regime ( $\sim 10^{12}$  W/cm<sup>2</sup>) [Ven96], the final quantum state denoting a sideband can be reached through two indistinguishable paths: one from the absorption of a photon from a primary XUV harmonic transition ( $q$ ), and the other from the emission of a photon from the consecutive primary XUV harmonic transition ( $q + 2$ ) (Fig. 2.15). Further, the phases of the two interfering pathways have opposite signs since one path involves an emission process and

the other an absorption process. It is easy to show, therefore, that the intensity of the sideband between the fundamental peaks  $q$  and  $q + 2$  is proportional to [Joh06]:

$$I_{SB}^{q,q+2}(\tau) \propto \cos(2\omega\tau + \phi_q - \phi_{q+2}) \quad (2.67)$$

giving an access to the relative phase between two consecutive harmonics,  $\Delta\phi_{q,q+2} = \phi_q - \phi_{q+2}$ . Provided the pulses within the APT are short, that is the intra-harmonic dispersion  $((\partial\phi_q/\partial\omega)_{q,q+2})$ , is small, the observed sideband intensity  $I_{SB}^{q,q+1}(\tau)$ , shows a periodic modulation with a period equal to the half-cycle period of the fundamental laser pulse, when the XUV-IR delay  $\tau$  is varied. In experiments, this average sub-cycle temporal beating is recorded for the different harmonic pairs and is the principle behind the RABITT ("Resolution of Attosecond Beating by Interference of Two-photon Transitions") method for complete characterization of APTs [Mul02]. Once the intra-harmonic phase ( $\Delta\phi_{q,q+2}$ ) for the involved harmonics is obtained, the individual phases  $\phi_q$  can be reconstructed by concatenation. With the amplitudes of the harmonics,  $A_q$  easily measured from the photoelectron spectrum (or using an XUV spectrometer) in an experiment with no dressing IR, the temporal structure of the APT is easily retrieved as

$$I_{XUV}(t) = \left| \sum_q A_q e^{-iq\omega t} e^{i\phi_q} \right|^2 \quad (2.68)$$

## 2.6 Photoionization in molecules

From the preceding sections it is clear that a coherent, ultrashort source of XUV radiation can be engineered from the HHG process occurring in the interaction of rare gas atoms with intense IR laser pulses. When the target gas is Ar, the XUV pulses have a bandwidth starting from  $\sim 20$  eV (the lower edge of the transmittance of an Al filter) to up to 40 eV in the cutoff region ( $3.17U_p + I_P$ ). The photon energies accessible are therefore, ideal to not only induce single photon ionization in molecules [Hik03], but also to leave the molecular ion in an excited state [Deh78, Hik02]. The decay of the excited states in molecules vis-à-vis rare gas atoms, is richer in dynamics with the involvement of nuclear processes such as vibration, rotation and even fragmentation of the molecule [Kou97]. Traditionally, such photon energies are available only through synchrotron sources or, in the very early stages, through discharge lamps where excellent spectral resolution could be obtained, but little or no time resolution. However, with the development of ultrashort XUV sources as introduced in the preceding sections, there has been a renewed theoretical and experimental interest in studying the time-resolved dynamics of photoionization of molecules [Gag07, San08, Per09]. In Chap. 5 we present the results of applying such a source to study fragmentation in  $D_2$  through the excited states of  $D_2^+$ . Therefore, in this section, we will introduce a few of the concepts involved in photoionization of diatomic homonuclear molecules. We begin with a brief review of molecular structure by way of familiarizing with the terms and symbols used.

### 2.6.1 Molecular structure and Born-Oppenheimer approximation

The molecule is defined as a bound system of electrons with more than one nucleus. A complete quantum mechanical description of multi-body systems is challenging, with no exact solutions existing for a majority of them. In the case of molecules, a considerable simplification is obtained by recognizing that the mass of the electrons is much smaller than that of the nuclei, while the forces associated are comparable in magnitude. As a result, the motion of the nuclei is much slower than that of the electrons. That is, on the time scales of electronic motion, the electrons essentially see the nuclei to be stationary, such that, to a very good approximation, we can treat the two motions independently. It would therefore, suffice to determine the electronic energies and wave functions at various spatial configurations of the nuclei. The electronic charge distribution thus obtained then shapes the potential in which the nuclei move. The theoretical framework which includes the above considerations is called the Born-Oppenheimer approximation, which will be implicit in the discussions that follow (along the lines of [Bra03]).

### 2.6.2 The hydrogen molecular ion

The simplest of all molecules is the hydrogen molecule,  $H_2$ , with two identical nuclei and two electrons. The corresponding molecular ion,  $H_2^+$ , is hence the simplest molecule, and therefore, provides a test system to develop the ideas of the previous subsection. In a diatomic molecule the various spatial configurations can be parameterized simply through one single variable: the internuclear separation  $R$ . If  $r_A$  and  $r_B$  are the displacement of the lone electron with respect to the two nuclei labeled as A and B, the Hamiltonian for the electron at fixed  $R$  is given by :

$$H_e = \left( -\frac{1}{2}\nabla_r^2 - \frac{1}{r_A} - \frac{1}{r_B} + \frac{1}{R} \right) \quad (2.69)$$

where, the spatial derivative,  $\nabla_r$ , is with respect to the midpoint of the inter-nuclear line. The Schrödinger Equation, neglecting spin-orbit and hyperfine interactions then reads as

$$(H_e + E_s)\Phi_s = 0 \quad (2.70)$$

In solving the wave equation, a useful coordinate frame is the one that is fixed with respect to the molecule called the body-fixed or molecular frame. In general such a frame can be constructed by choosing the  $Z$  axis along the internuclear line, and having the  $Y$  axis to coincide with the space-fixed (or laboratory frame)  $Y'$  axis. Before we proceed to obtain the eigenvalues for the electron energies a useful insight into the choice of the eigenfunctions of the electrons can be obtained by noting a few symmetries that exist in diatomic molecules.

### 2.6.3 Symmetries in diatomic molecules

At first glance, we note that, in contrast to the case of atoms, all directions in space are no longer equivalent for a diatomic molecule. With the internuclear axis defining an axis of

symmetry, the electronic Hamiltonian is invariant under rotations about the  $Z$  axis. The same, however, cannot be said of rotations about  $X$  and  $Y$ . The electronic eigenfunctions  $\Phi_s$  of a diatomic molecule can therefore, be constructed to be simultaneous eigenfunctions of the Hamiltonian  $H_e$  and the rotation operator about the  $Z$  axis,  $L_z$ . In other words,

$$L_z\Phi_s = M_L\Phi_s, \quad M_L = 0, \pm 1, \pm 2, \dots \quad (2.71)$$

$$= \pm\Lambda\Phi_s, \quad \Lambda = 0, 1, 2, \dots \quad (2.72)$$

where  $\Lambda = |M_L|$  is the absolute value of the projection of the total angular momentum on the internuclear axis. The spectroscopic notation associated with  $\Lambda$  is similar to that for atoms and is given by table 2.1. When referring to a single electron, as in the case of  $H_2^+$ , the more commonly used notation is given in table 2.2.

Value of $\Lambda$	Notation
0	$\Sigma$
1	$\Pi$
2	$\Delta$
3	$\Phi$

Value of $\lambda$	Notation
0	$\sigma$
1	$\pi$
2	$\delta$
3	$\phi$

The next symmetry property for the electronic Hamiltonian is the invariance under reflections in all planes which contain the internuclear axis. For example, the reflection of the electrons about the  $XZ$  plane corresponds to the operation  $y_i \rightarrow -y_i$ , denoted by the operator  $A_y$  and

$$[A_y, H_e] = 0, \text{ and} \quad (2.73)$$

$$A_y L_z = -L_z A_y. \quad (2.74)$$

From the above equation, it is clear to see that if  $\Lambda \neq 0$ , the reflection operation leads to a degenerate function with eigenvalue  $-\Lambda$ . Thus, the electronic terms  $\Pi, \Delta, \Phi \dots$  are doubly degenerate, with the states differing by the direction of the propagation of the orbital angular momentum along the molecular axis. In contrast, the  $\Sigma$  states are non-degenerate. Further, simultaneous eigenfunctions of  $H_e, L_z$  and  $A_y$  can be constructed with the eigenvalues of  $A_y$  being  $\pm 1$ . Thereby the  $\Sigma$  states are distinguished as  $\Sigma^+$ , for which the wave functions are left unchanged upon reflection and as  $\Sigma^-$ , for which the wave function changes its sign upon reflection.

Another symmetry which occurs in homo nuclear diatomic molecules is the existence of a center of inversion that is the midpoint of the internuclear axis. Clearly, a reflection of the coordinates of all the electrons with respect to this point, leaves the Hamiltonian unchanged. Furthermore, the inversion process can be deconstructed into two commuting operations: i) reflection in a plane perpendicular to the internuclear axis, containing the midpoint and ii) rotation about the  $Z$ -axis. The operator associated with inversion

therefore, commutes with  $L_z$ , the operator for rotation about  $Z$ -axis. So for a given  $\Lambda$ , the states can be classified according to their behavior with respect to inversion. The states with even parity remain unchanged upon inversion and are called *gerade* states, designated by the subscript  $g$  in the term symbol. Conversely the states with an odd parity change sign upon inversion, and are called *ungerade* states, designated  $u$ . So finally, for a homo nuclear diatomic molecule, we arrive at four non-degenerate  $\Sigma$  states:  $\Sigma_g^+, \Sigma_u^+, \Sigma_g^-, \Sigma_u^-$ .

### 2.6.4 Potential energy curves for the $H_2^+$ ion

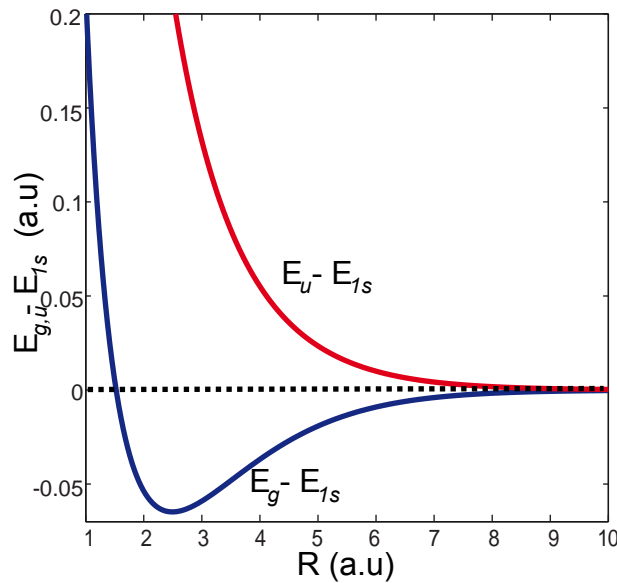


Figure 2.16: The calculated potential energy curves of the  $1s\sigma_{g,u}$  states of  $H_2^+$  using the eq. 2.79. The red repulsive curve corresponds to the anti-bonding orbital with  $u$  symmetry. The blue curve is attractive forming a 'well' with binding energy of  $D_1 = 0.065$  a.u. = 1.77 eV. At  $R \rightarrow \infty$ , both the curves lead to dissociative products  $H$  and  $H^+$ .

Returning to the molecular ion  $H_2^+$ , the object is to obtain the electron energy as a function of the inter-nuclear distance, thus, defining the potentials on which the nuclei move. An insight can be gained by approximating the electronic orbital through a linear combination of atomic orbitals (LCAO), where the atomic orbitals are those of the nuclei  $A$  and  $B$ . When the two nuclei are far apart, the electron is attached to one of them. So if the electron is attached to nuclei  $A$ :

$$\Phi(R; r) = \phi_{1s}(r_A) \quad (2.75)$$

where  $\phi_{1s}(r_A) = \pi^{1/2} \exp(-r)$  is the normalized ground state wave function for atomic hydrogen. Of course, this is not the complete solution for the molecular orbital, as it lacks

any specific symmetry with respect to the center of the inter-nuclear axis. So the following linear combinations are possible:

$$\Phi_g = \frac{1}{\sqrt{2}} [\phi_{1s}(r_A) + \phi_{1s}(r_B)], \text{ and} \quad (2.76)$$

$$\Phi_u = \frac{1}{\sqrt{2}} [\phi_{1s}(r_A) - \phi_{1s}(r_B)]. \quad (2.77)$$

which are even ( $\sigma_g$ ) and odd ( $\sigma_u$ ) respectively under inversion about the midpoint of the internuclear axis. The above trial wave functions are accurate only in the asymptotic region of large  $R$ . Nevertheless, an approximation for the ground state energy for the molecular ion can easily be obtained through variational analysis and can be written as:

$$E_{g,u}(R) = \frac{\int \phi_{g,u}^* H_e \phi_{g,u} dr}{\int |\phi_{g,u}|^2 dr} \quad (2.78)$$

A little bit of mathematics and we arrive at an expression for the ground state energy as a function of  $R$

$$E_{g,u}(R) = E_{1s} + \frac{1}{R} \frac{(1+R)\exp(-2R) \pm (1-2R^2/3)\exp(-R)}{1 \pm (1+R+R^2/3)\exp(-R)} \quad (2.79)$$

where  $E_{1s} = -0.5$  a.u is the ground state energy of atomic hydrogen. Plotted in Fig. 2.16 are the electron energies for the gerade and ungerade states as a function of internuclear distance  $R$ . The nuclear wave equation can therefore, be solved, where  $E_{g,u}$  play the role of a potential. As  $R \rightarrow 0$ ,  $E_{g,u}(R)$  is dominated by Coulomb repulsion between the nuclei. On the other hand as  $R \rightarrow \infty$ ,  $E_{g,u}$  converges to the ground state energy of atomic hydrogen,  $E_{1s}$ , which indeed it should, as the two nuclei are so far apart that the electron is under the influence of only one of the nuclei. These curves are termed as the lowest electronic potential energy curves for  $H_2^+$ .

Further, the function  $E_g$  exhibits a minimum at  $R_0 = 2.49$  a.u ( $1.32 \text{ \AA}$ ) with binding energy of  $D_1 = E_{1s} - E_g(R_0) = 0.065$  a.u = 1.77 eV. Since the curve represents a net attractive force between the two nuclei, mediated by the electron, the corresponding molecular orbital is termed as a bonding molecular orbital, with a binding energy given by  $D_1$ . The exact ground state molecular orbital of the  $H_2^+$  ion is therefore, designated as  $1s\sigma_g$ . On the other hand, the function  $E_u$  has no minimum, hence, the curve is repulsive, and the  $H_2^+$  ion in this anti bonding orbital immediately dissociates into a proton and a hydrogen atom in the  $1s$  state. This orbital is designated by  $1s\sigma_u^*$ . While the discussion above was done using approximate trial wave functions constructed through LCAO, it is evident that at least for the case of the hydrogen ion, it is fairly simple to numerically solve 2.70, to derive the potential curves for the various electronic states of  $H_2^+$ . Similarly, the potential curves for  $H_2$  can also be calculated. Plotted in 2.17 are examples of the potential curves for  $H_2^+$  with respect to the ground state of  $H_2^8$ ,  $X^1\Sigma_g^+$

<sup>8</sup>Here X in general denotes the ground state of a molecule, and the superscript  $2S+1=1$  indicates the net spin of the electrons.

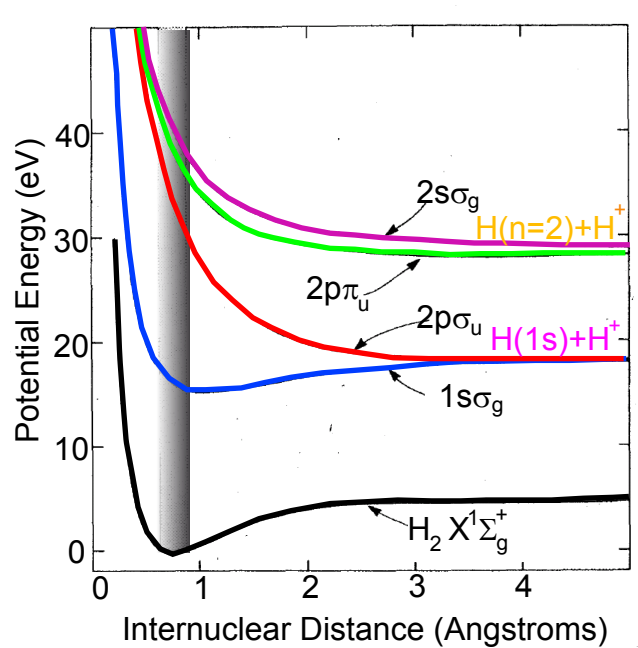


Figure 2.17: The calculated potential energy curves of  $H_2^+$  with respect to the ground state of  $H_2$ ,  $X^1\Sigma_g^+$  (black). There is only one bound electronic state in  $H_2^+$ , with the term symbol  $X^2\Sigma_g$ , also commonly written as  $1s\sigma_g$ . The next higher curve which converges to the  $1s\sigma_g$  curve at  $R = \infty$  is the repulsive  $2p\sigma_u$ . At the dissociation limit ( $R = \infty$ ) of these two curves we get a proton and a neutral  $H$  in the ground state. The higher repulsive curves dissociate to a proton and a neutral  $H$  in the  $n = 2$  state.

### 2.6.5 Selection rules for dipole-allowed transitions in molecules

Since the photon energy of the sources considered in this work are in the range of a few tens of eV, the molecular transitions induced following the absorption of a photon can be considered within the framework of the dipole approximation (see §2.1). The selection rules for dipole allowed transitions in molecules is much more involved than those in atoms, and therefore, will be considered in some detail in this subsection. In general, one can use symmetry considerations to arrive at the selection rules. That is, since the probability amplitude is a scalar quantity, the total symmetry of the integrand in the matrix element connecting a transition from an initial molecular state  $\psi_i$  to the final state  $\psi_f$ ,  $\langle \psi_i | \mu | \psi_f \rangle$  should be symmetric;  $\mu$  is the dipole operator ( $-\vec{E} \cdot \vec{r}$  in the Coulomb gauge).

If the electric field inducing the transition is linearly polarized, then the dipole operator is given by  $\mu_z = -Ez$  and two directions in space are evident. The first is defined by the polarization axis, and the second being the internuclear axis. In an isotropic sample the molecular axis is randomly aligned with respect to the polarization axis. If the polarization axis is aligned along the molecular axis, then it is easy to see that the dipole operator ( $\mu_z$ ) has the same symmetry properties as a  $\sigma_u^+$  orbital. That is, a reflection of the dipole

operator in the  $XZ$  plane leaves it unchanged, while an inversion about the midpoint of the inter-nuclear axis causes it to change its sign. So the integral is symmetric only if the final and initial states are symmetric-antisymmetric pairs of each other. In other words<sup>9</sup>, the allowed transitions are restricted to  $\Delta\Lambda = 0$ ,  $+\leftrightarrow +'$ ,  $-\leftrightarrow -$ , and  $g\leftrightarrow u$ , where  $\leftrightarrow$  indicates that the transition is allowed in both directions. The class of transitions defined by the above set of selection rules are known as *parallel* transitions.

Similarly, when the polarization is aligned perpendicular to the internuclear axis the dipole operator has a  $\pi_u$  symmetry and the selection rules for the allowed transitions, called *perpendicular* transitions, are more involved and need to be derived through Group Theory [Hol72, Har78, Bun79]. The dipole-allowed transitions for both parallel and perpendicular transitions can be neatly summarized in the following table adapted from [Dun76]:

Table 2.3: Dipole-allowed Transitions

	$\Sigma_g^+$	$\Sigma_g^-$	$\Sigma_u^+$	$\Sigma_u^-$	$\Pi_g$	$\Pi_u$	$\Delta_g$	$\Delta_u$
$\Sigma_g^+$	X	X	$P_{  }$	X	X	$P_{\perp}$	X	X
$\Sigma_g^-$		X	X	$P_{  }$	X	$P_{\perp}$	X	X
$\Sigma_u^+$			X	X	$P_{\perp}$	X	X	X
$\Sigma_u^-$				X	$P_{\perp}$	X	X	X
$\Pi_g$					X	$P_{  }$	X	$P_{\perp}$
$\Pi_u$						X	$P_{\perp}$	X
$\Delta_g$							X	$P_{  }$
$\Delta_u$								X

where,  $P_{||}$  and  $P_{\perp}$  indicate allowed parallel and perpendicular transitions respectively, while  $X$  indicates a dipole-forbidden transition. Finally, while the above discussion pertained to bound-bound transitions, photoionization processes involve the electric dipole-allowed bound-free transitions. The selection rules in general are more involved and have been comprehensively derived by Xie and Zare [Xie90], but for the molecule of interest,  $H_2$ , the work of Dehmer and Dill [Deh78] is illustrative and the key results can be summarized in the table 2.4 (Adapted from [Deh78])

## 2.7 Summary

To briefly summarize this chapter, we have shown how the interaction of moderate as well as intense laser fields with atoms, leads to ionization, where the photoelectron energy spectrum mainly consists of equidistant structures called ATI peaks. An offshoot of strong-field interactions is the generation of high harmonics, which through clever techniques can be synthesized to give rise to ultrashort, coherent XUV pulses. These pulses can be fully characterized by overlapping a synchronized IR pulse and analyzing photoelectron spectrum

<sup>9</sup>the general set of selection rules can be derived through Group Theory

Table 2.4: Dipole allowed transitions in Photoionization of molecules

Channel	Symmetry of $H_2^+$ ionic state	Dipole -allowed photoelectron symmetry	Total ion core plus photoelectron symmetry
1	$1s\sigma_g$	$\sigma_u$	$\Sigma_u$
2	$1s\sigma_g$	$\pi_u$	$\Pi_u$
3	$2p\sigma_u$	$\sigma_g$	$\Sigma_u$
4	$2p\sigma_u$	$\pi_u$	$\Pi_u$
5	$2p\pi_u$	$\sigma_g$	$\Pi_u$
6	$2p\pi_u$	$\pi_g$	$\Sigma_u$
7	$2p\pi_u$	$\delta_g$	$\Pi_u$
8	$2s\sigma_g$	$\sigma_u$	$\Sigma_u$
9	$2s\sigma_g$	$\pi_u$	$\Pi_u$

thereof, for a varying delay between the XUV and the IR pulses. Finally, as an example of the application of these XUV pulses to study processes in atomic and molecular physics, we have considered the interaction of XUV radiation with simple diatomic molecules such as  $H_2$ . In the next chapter, we will describe the experimental techniques which we have used in this work, to study the various processes mentioned in this chapter.



# Chapter 3

## Experimental techniques

In this work we have studied photoionization and dissociation processes in atoms and molecules introduced in the preceding chapter using the technique of momentum spectroscopy of the charged fragments. The basic scheme of the experiment can be described in brief as follows: A photon beam is crossed with a supersonic jet, which provides a cold atomic or molecular target. The interaction volume lies in the center of a so-called Reaction Microscope, which is essentially a cold target recoil-ion momentum spectrometer (COLTRIMS) combined with a large solid angle electron momentum spectrometer [Ull03]. A homogeneous constant electric field extracts the ions and electrons created in the interaction region in opposite directions. A homogeneous magnetic field parallel to the spectrometer axis serves to confine the electrons in the radial direction. The charged particles are detected by position and time-of-flight sensitive detectors located at each end. The time-of-flight (TOF) and the positions of the detected particles are recorded and used to reconstruct their trajectories and thereby finally obtain the three dimensional (3D) momentum spectra of all the fragments. In this chapter, we will elaborate on the experimental technique beginning by describing the generation of the photon beams at the MPI-K HHG laboratory. The alignment of the photon beams into the spectrometer will be detailed in Sec. 3.2. In Secs. 3.3 and 3.4, we then describe the construction and specifications of the cold gas target and the ion and electron spectrometer, which were purpose-built for the MPI-K HHG laboratory. The present design of the Reaction Microscope (REMI) is based on the prototype designed and constructed earlier for experiments with low brilliance, high repetition IR sources [Dew06]. The detection of the fragments, followed by the acquisition and the recording of the TOF and position signals are discussed in Sec. 3.5. The reconstruction of the initial momenta of the fragments from these signals is described in the sections after this. Finally, we provide as an example, the study of two-colour XUV-IR photoionization in helium, with the present experimental setup to illustrate its performance for a well-known process.

## 3.1 Source

### 3.1.1 The laser system

The work-horse of the experiments at the HHG laboratory at MPI-K is the commercially assembled laser system from 'Kapteyn-Murnane Laboratories' (KM Labs), which provide us with  $\sim 32$  fs pulses at 1 mJ at repetition rates adjustable from 3 to 10 kHz, delivering an average power of up to 9 W. The innovative use of a high repetition laser source was required due to the low efficiency of the HHG process. By operating at repetition rates which exceed those of all other comparable laser sources in the world, we increase the number of photons available per second significantly, thereby reducing acquisition times for the experiments.

The heart of the system is a mode-locked Titanium-Sapphire (Ti:Sa) laser oscillator, Model MTS-I, pumped by a frequency doubled (532 nm) Nd: YVO - continuous wave laser ("Verdi" from Coherent Inc.) The oscillator generates 18 fs pulses at a repetition rate of 80 MHz and an average power of 650 mW. The pulses are in the near infrared (IR) region of the electromagnetic spectrum with a central wavelength of 785 nm and a spectral bandwidth of about 60 nm.

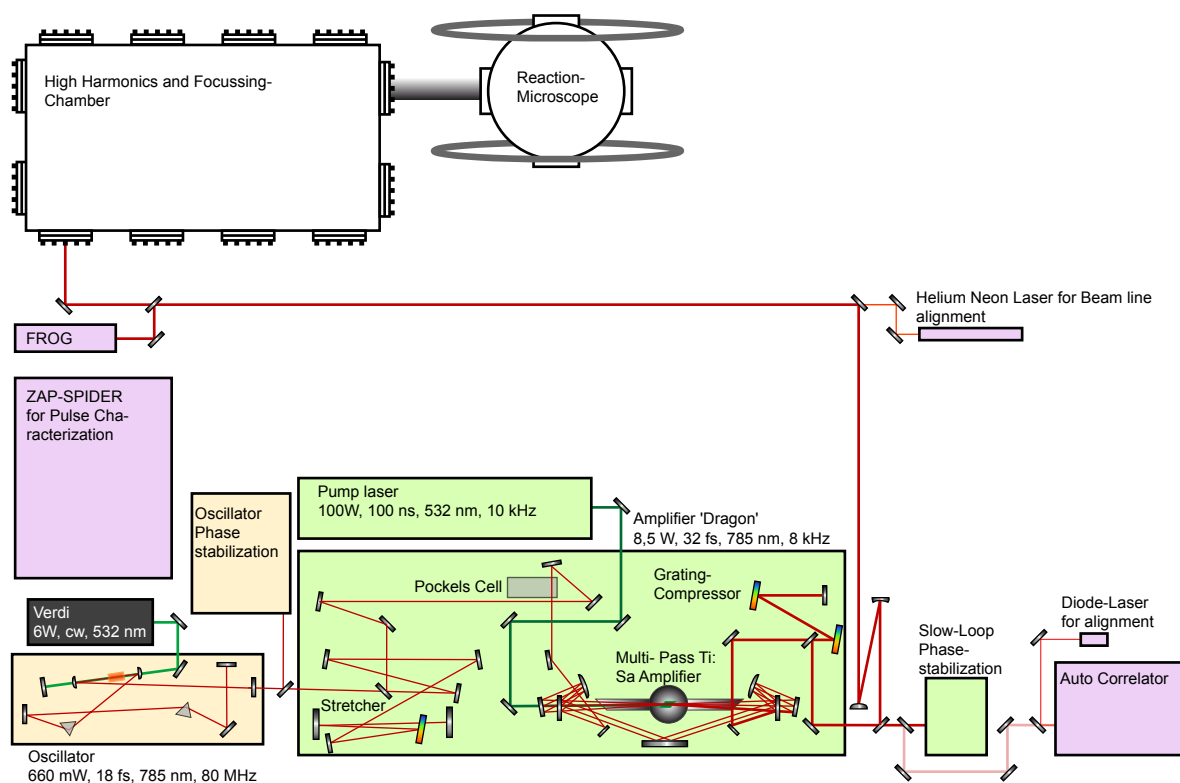


Figure 3.1: A schematic of the laser system including the high harmonics generation source and the Reaction Microscope.

The single pulse energy of the oscillator in the range of 8 nJ is then amplified with the Chirped Pulse Amplification (CPA) based "Dragon" system from KM Labs. In the CPA scheme the ultrashort pulses of the oscillator are initially stretched by nearly 5 orders of magnitude, so as to lower the peak intensity reached in the amplifier crystal during the amplification. The Ti:Sa amplifier crystal is pumped by a frequency doubled (532 nm), Q-switched, 100 W, 100 ns, Nd: YAG laser system from "Lee Lasers Inc." with an adjustable repetition rate from 3-10 kHz. The high repetition rate of up to 10 kHz is supported in the crystal by cooling it in a closed-cycle helium. At a temperature of about 60 Kelvin the crystal is at its maximum thermal conductivity thereby reducing thermal lensing effects. In the amplification stage, the pulses from the oscillator are steered by two focusing mirrors placed in a ring-shaped arrangement to pass through the crystal a total of 13 times. The pulses are temporally and spatially overlapped with the pump pulses, to obtain a gain of about  $10^5$ . The amplified pulses are then compressed with a gratings compressor to obtain 30 fs, 1 mJ pulses.

### 3.1.2 HHG chamber

The pulses from the Dragon amplifier are then steered into the rectangular vacuum chamber, indicated as HHG chamber in Fig. 3.1. This chamber while containing the XUV source also contains the setup for realizing two-colour XUV-IR experiments. In brief, the IR pulses enter the chamber through a glass window (lower left in Fig. 3.2). In the chamber the pulses are split using a thin 30% beam splitter (**B**) (Thor Labs Inc.) into the two arms, which form a Mach-Zehnder arrangement, eventually meeting at the gas target of the Reaction Microscope. The arm of the interferometer with maximum energy is used to generate the XUV pulses, while the other arm which forms the IR branch is matched exactly in optical length, so that the XUV and the IR pulses overlap in time and space at the gas target.

We note here that the main challenge in conducting two colour XUV-IR experiments is not in the least the generation of XUV pulses, but more so in ensuring control and stability in the interferometric arms against mechanical drifts on the level of hundred nanometers. This is especially the case if APTs or single attosecond pulses are used to study time-resolved processes, where the pulse duration of 300 as would require us to have precise mechanical control on the level of at least 100 nm. To achieve this the HHG chamber is endowed with many unique features. Since the XUV pulses are rapidly absorbed in atmosphere, the HHG chamber is in vacuum. By including the two arms of the interferometer in the vacuum chamber we eliminate dispersion due to propagation in air, which would introduce an element of uncertainty<sup>1</sup>. The optical breadboard for the optics is mounted using three posts on the optical table of the laser system, with no mechanical connection to the vacuum chamber, thus isolating the optics from vibrations of the pumps connected to the chamber. The chamber as such is supported by an external aluminum scaffolding. The vacuum sealing on the lower side where three ports are provided for the

---

<sup>1</sup>for example drifts due to local air currents

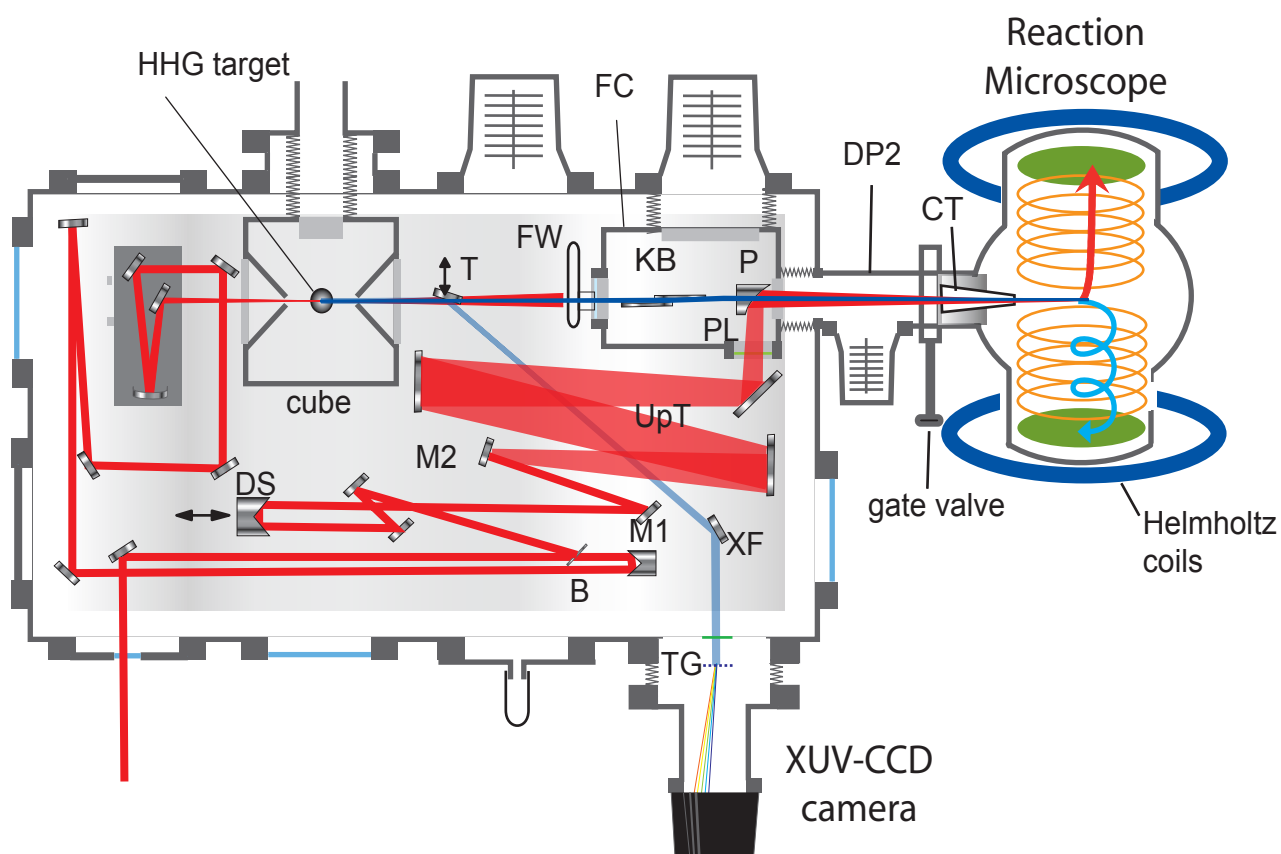


Figure 3.2: A schematic of the HHG chamber housing the HHG target and also the optics of the Mach-Zehnder interferometer for the two-colour XUV-IR experiments.

posts of the optical breadboard is through bellows mounted on the laser optical table. The bellows, therefore, prevent vibrations from being transferred to the laser optical table. The entire chamber is pumped by a 500 l/s turbo-molecular pump and reaches a best vacuum of  $\sim 1 \times 10^{-4}$  mbar. Here we refer to [Rie06] for more details.

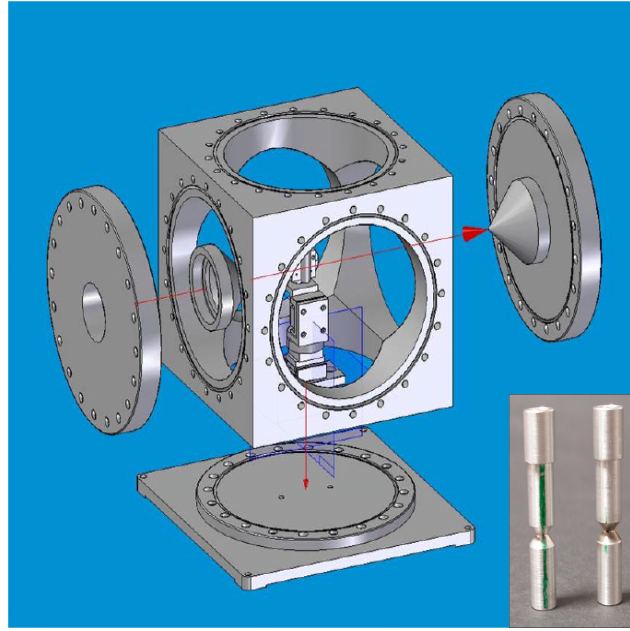


Figure 3.3: (a) The cube houses the gas cell for harmonics generation which is depicted in the inset.

In Fig. 3.2, the two paths of the Mach-Zehnder interferometer are shown schematically. Considering the HHG path for now, the beam is focused by a 350 mm focal length mirror into a 'cube' as shown in Fig. 3.2. The 'cube' is a 'chamber in a chamber' (Fig. 3.3) containing the gas target for high harmonic generation and is elaborated below.

The gas target as shown in the inset of Fig. 3.3 is essentially an aluminum gas cell with pre drilled entrance and exit apertures ( $\phi < 3$  mm) for the light beams. The gas cell is connected to an external gas bottle with stagnant pressures of about 100 mbar. The region surrounding the gas cell is evidently a region with a high gas density, which through absorption will quickly extinguish the XUV radiation emitted in the high harmonic process. Therefore, to minimize the propagation of the XUV through these high density regions, a chamber in chamber arrangement, the 'cube', constrains the gas load. Optical access for the in-coming and out-going laser beams is through a pair of oppositely oriented cones perforated at the apices with bores of diameter  $\phi \sim 250 \mu\text{m}$ . The cones extend all the way to the gas target, so that on the exit side the HHG beam traverses only a few cm of high density region. Furthermore, the conical geometry reduces the conductance of gas particles from the cube to the surrounding regions. Thus, a pressure difference of nearly two orders of magnitude between the cube and the outer chamber can be maintained. For

example, with a typical stagnant pressure of 100 mbar in the gas cell, in the cube one reaches a pressure of  $\sim 4 \times 10^{-2}$  mbar, while the ambient pressure remains at  $\sim 8 \times 10^{-4}$  mbar. The high gas load within the cube is pumped out by a side channel pump (Ontool Booster, Pfeiffer Vacuum GmbH). Additionally, the apertures of the cones along with two external apertures essentially fix the XUV beam line.

The intense IR laser pulses give rise to coherent XUV radiation in the gas target through HHG as described in Sec. 2.3. The XUV beam emerges collinear with the rest of the IR beam. A grazing incidence gold mirror at 60 degrees to the normal mounted on a translation stage **T** optionally picks off the radiation and directs it to a focusing mirror **XF**. The focused beam, with the IR and the lower harmonic components filtered off using a  $0.6 \mu\text{m}$  Al foil is incident on a transmission grating **TG** optimized for XUV radiation. The first order diffracted light, therefore, is recorded using a CCD camera, providing the HHG spectrum. The XUV spectrometer is discussed in detail in [Rie06]. In experiments, the HHG spectrum is thus obtained in real time (Fig. 3.4) to optimize the photon flux and spectrum. Following this the pickoff mirror is moved out to allow the HHG beam to be then focused onto the target in the Reaction Microscope (Fig. 3.2).

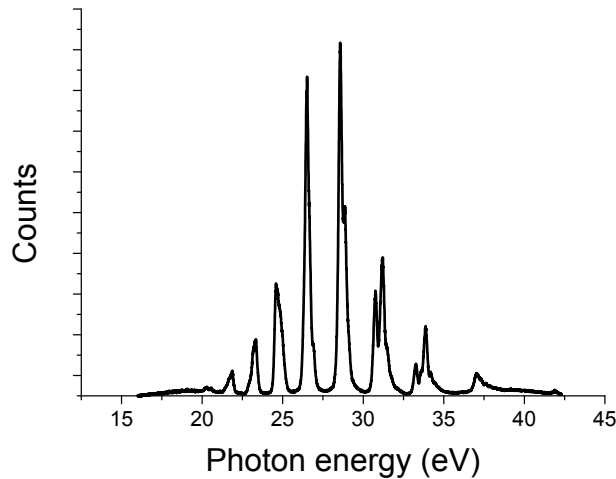


Figure 3.4: A typical photon energy spectrum obtained from the XUV spectrometer.

### The IR branch

The second arm of the Mach-Zehnder interferometer is constructed from the second branch at the beam splitter. It contains a retro reflecting element mounted on a precision, piezo stage (MS 30, Mechonics AG), which provides in a closed loop configuration a positioning precision of 50 nm, over a travel range of 30 mm (**DS**). The smallest optical delay that can be generated between the two arms of the interferometer is 100 nm which corresponds to a time delay of 330 as. The piezo element is controlled by an external hardware device

which can be interfaced with a computer. An in-house written LABVIEW program with a GUI [Sim09], provides a control over the movement of the Mechonics translation stage. Furthermore, the entire piezo based translation stage is mounted on a micrometer screw translation stage to allow for a manual rough translation in the range of a few centimeters. Since focusing optics are also housed in the same chamber, the geometry, particularly the large Helmholtz coils of the Reaction Microscope (see Fig. 3.2) imposes an minimum focal distance. Therefore, we are constrained on the maximum intensity of the IR pulses that can be reached at the target, not only because most of the IR energy is used in creating the harmonics, but also on account of the increased focal distance. Hence, we introduced an up-telescoping (**UpT**) optical setup to increase the diameter of the laser beam, to have a smaller focal spot size, and, therefore, larger intensities. An additional advantage is that the effective IR focal distance can be controlled by adjusting the divergence of the beam.

The two branches, the IR beam and the XUV enter the focusing chamber as shown in Fig. 3.2.

### Focusing Chamber

Continuing on the principle of having all the optics mechanically connected, the focusing optics for both the XUV and IR beams are also mounted on the same breadboard, but housed in another 'chamber in a chamber'. This focusing chamber (**FC**), which is independently pumped, thus also acts as the first differential pumping stage between the poor vacuum conditions in the HHG chamber ( $4 \times 10^{-4}$  mbar) and the UHV chamber of the Reaction Microscope ( $5 \times 10^{-10}$  mbar). The **FC** is pumped by a 300 l/s turbo pump, which is connected to it through a large bellow, to again isolate vibrations from the pump. The **FC** reaches pressures of  $1 \times 10^{-6}$  mbar. The XUV beam enters the FC through a window which is hermetically sealed on the high pressure side by a motorized 'filter-wheel' (**FW**) which can house up to 8 filters. In § 2.4, we had elucidated the role of a high band pass filter in the XUV in suppressing not only the IR but also the lower order harmonics in the HHG beam. Depending on the requirement of the experiment a filter can be chosen, but in the context of this thesis, the filter wheel housed Al filters with varying thickness of 200 nm, 400 nm, 600 nm and 800 nm. At least one of the slots was left blank, so as to allow throughput for the rest IR beam during alignment (see § 3.2). The XUV beam is then focused onto the target in the Reaction Microscope using a pair of mirrors at grazing incidence **KB**, in a modified Kirkpatrick-Baez (K-B) configuration [Kir48].

As illustrated in Fig. 3.5, a spherical mirror (Sph) with a radius of curvature of 5000 mm ( $R_s$ ) is aligned at an angle of  $\sim 6^\circ$  to the incoming XUV beam. A single spherical mirror focusing at grazing incidence produces a line focus. In the conventional K-B set up the focusing in the other dimension is achieved using a second spherical mirror whose axis is perpendicular to the first (left panel of Fig. 3.5). In our modified set up, we do the same using a 'half-pipe' cylindrical mirror with an radius of curvature of 60 mm ( $R_c$ ) placed with its axis parallel to that of the spherical mirror at an inter-mirror separation of  $\sim 30$  mm. Using the known formulae for focusing at a grazing incidence [Ton79] it is easy to show that the design values for the radius of curvature of the two mirrors are such

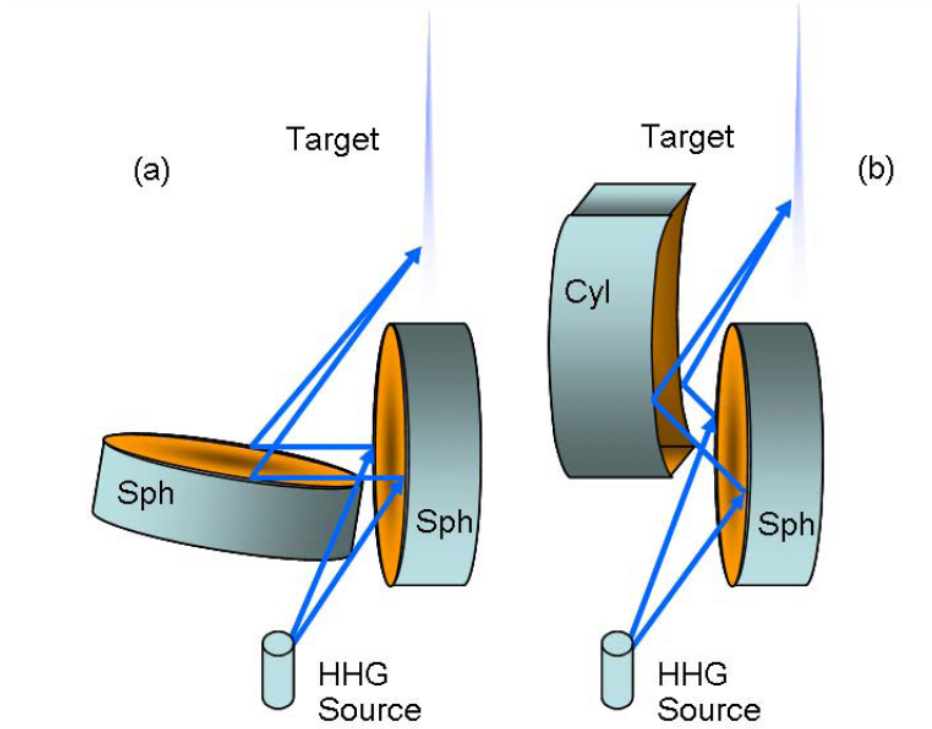


Figure 3.5: (Left) Conventional K-B setup of two spherical mirrors (Sph) aligned with their axes perpendicular to each other. In the modified K-B setup used here (right), the second mirror focusing the sagittal rays is replaced by a cylindrical mirror (cyl) as shown.

that the focal spot of the two mirrors coincide at the target in the Reaction Microscope. For the spherical mirror, the meridional rays (which lie in the plane containing the radius of curvature of the mirror at the point of incidence on the mirror) are focused according to [Ton79]

$$\frac{1}{d_{sm1}} + \frac{1}{d_{m1t}} = \frac{2}{R_s \cos i} \quad (3.1)$$

With the measured source to mirror distance,  $d_{sm1}$  as 451 mm, and mirror to target distance,  $d_{m1t}$  as 765 mm, this translates to an angle of incidence  $i$ , (with respect to the normal) as  $6.5^\circ$ . For the cylindrical mirror, the sagittal rays (in the plane perpendicular to the meridional rays) are focused according to

$$\frac{1}{d_{sm2}} + \frac{1}{d_{m2t}} = \frac{2 \cos i}{R_c} \quad (3.2)$$

With the distances,  $d_{sm2}=481$  mm and  $d_{m2t} = 735$  mm (to the target), we get the angle of incidence  $i$  to be  $5.9^\circ$ . Thus, the emergent XUV beam is nearly parallel to the incoming

beam, albeit with a slight angle. The mirrors are coated with gold for maximum reflectivity. At an angle of  $\sim 6^\circ$ , we have a reflectivity of  $\sim 80\%$  in the photon energy range of 30-50 eV [CXRO].

There is also a lateral displacement of the out-going beam of  $\sim 2$  mm after the focusing mirrors, with respect to the in-coming beam, corresponding to the lateral displacement of the mirrors with respect to each other. This close arrangement of the mirrors limits the spatial extent of the XUV beam to  $\sim 2$  mm. A useful consequence of this spatial filtering is a suppression of the contribution to the harmonics due to the long paths of the recolliding electron, thereby providing compression of the HHG to attosecond pulse trains (APT).

The IR beam enters the **FC** through a window which is sealed by thin pellicle (2  $\mu\text{m}$ , Thor Labs) made of Nitro Cellulose **PL**. The beam is then focused using an off-axis parabolic mirror (**P** in Fig. 3.2) with a nominal focal distance of 600 mm. The parabolic mirror is bored (dia. 3mm) along its axis to allow the XUV beam to come through. In the first differential pumping stage **FC**, a pressure of  $1 \times 10^{-6}$  mbar is reached which is still not optimal to be directly coupled with the ultra-high vacuum (UHV) spectrometer chamber of the Reaction Microscope. Therefore, a further differential pumping stage is provided, indicated as **DP2** in Fig. 3.2. **DP2** is separated from **FC** through a pellicle with a 3 mm hole<sup>2</sup> so that there is nearly no gas conduction, and is pumped with a 30 l/s turbo pump. The pressure reached in the **DP2** is at best  $5 \times 10^{-8}$ . Finally a connection with low gas conductance between **DP2** and the spectrometer chamber of the Reaction Microscope is provided through a conical tube tapering into the UHV side **CT**. Furthermore a gate valve is provided in **DP2**, to completely isolate the Reaction Microscope from the **FC** when required. The gate valve is equipped with a glass window, so that even when it is closed, there is optical access into the Reaction Microscope. Thus, the optical alignments could be performed with the Reaction Microscope fully in vacuum. In the following section we shall elaborate on the initial alignments performed so as to have an overlap of the XUV, IR and the atomic beam.

## 3.2 Aligning the XUV and IR beam line

Prior to connecting the **FC** with the Reaction Microscope, the photon beam line was fixed. A He-Ne laser beam was aligned onto the apertures provided by the cones in the Cube. The filter wheel was positioned to allow the He-Ne beam to be focused by the grazing incidence mirror pair. Here, we note that the distance from the mirrors to the reaction zone is fixed. At this position the CCD chip of an inexpensive video camera was placed. The two mirrors were adjusted such that the focal spot on the camera had the least size and was most symmetric and circular. Since we know the position of the atomic beam in the reaction microscope to within 1-2 mm of the center of the reaction chamber, the Reaction Microscope was moved so as to coincide the atomic beam with the reaction zone. Minor adjustments in the transverse jet position had to be made by moving the entire Reaction Microscope on the scale of a few mm. To achieve this, the Reaction Microscope is hoisted on

---

<sup>2</sup>The XUV is not transmitted through by the pellicle.

a frame fitted with roller guides in a C-Rail configuration (item Industrietechnik GmbH). The translation is effected by an inexpensive in-house constructed lead screw with a nut and screw mate, providing a minimum translation of 1 mm. Finally the actual XUV beam was used and ionization of the atomic beam was observed. The overlap was optimized by maximizing the counts from ionization of the target gas, relative to the counts from rest gas ionization.

Next, to adjust the focus of the IR beam line an optical setup was constructed such that the focus in the Reaction Microscope was imaged onto a CCD camera (Fig. 3.6). An additional complication in aligning with an off-axis parabolic mirror is that when the incoming incident beam is not at  $90^\circ$  to the outgoing axis of the parabolic mirror, the reflected beam is astigmatic and, therefore, two focii corresponding to the horizontal and vertical directions are seen. So first by carefully aligning the beams, and monitoring the focal spot using the camera to converge the two focii, an optimum alignment for the parabolic mirror was found. Fine adjustments to the divergence of the IR beam, such that the focus was in the center of the spectrometer, were made later by looking at the position spectra (Sec. 3.9.1 and Fig. 3.16(b)) of the ionized rest gas. The optimum overlap with the atomic beam was confirmed by the maximization of the counts of the cold target (Argon) relative to the counts from the rest gas.

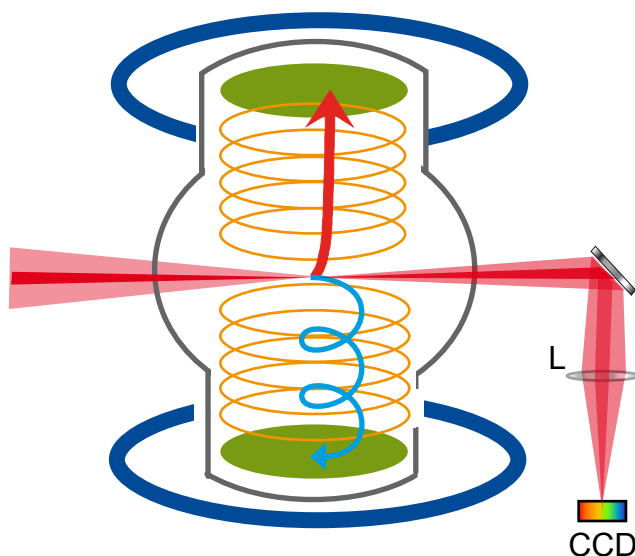


Figure 3.6: An illustration of the setup to image the focus of the XUV and IR branches. The filter wheel is opened so that the rest IR on the HHG branch forms the central part and the IR branch forms the annular part of the beam. The common focus is imaged by the lens L in a 1:2 magnification ratio onto the CCD chip of an inexpensive video camera.

To finally obtain a spatial and temporal overlap of the XUV and IR beams, we looked at

the annular IR branch and the central IR coming through the hole in the parabolic mirror, at the image of their focus in the CCD camera. The central IR is the rest IR unused in the generation of HHG, and comes through to the **FC** when an empty slot on the filter wheel is used. While the path length between the XUV and the IR branches were made equal to within a few cm in the design of the two paths, the fine adjustment was done with the help of the micrometer translation stage and finally the piezo translation stage (Mechonics). When the central IR pulse and the annular IR pulse are temporally overlapped, a fringe pattern is observed whose contrast rapidly falls away as the delay between the two branches of the Mach-Zehnder interferometer is changed. To have optimum spatial overlap, and also collinearity of the two beams, we used a pair of motorized mirrors in the IR beam line, **M1** and **M2**, to iteratively align the IR beam. At the best spatial overlap, the centers of the annular IR beam and the central IR beam coincide when observed at a point far away from the focus, while simultaneously the image of the two foci in the camera coincide. At the end of the optical alignment procedure a uniform concentric distribution of the high contrast fringes attests to the wavefronts being parallel and an optimum temporal overlap.

Having described how the photon beams were made to focus into the atomic beam in the Reaction Microscope, we now proceed to elaborate on the construction and specifications of the cold gas target.

### 3.3 The gas target

A schematic of the gas jet target is shown in Fig 3.7. The target gas at room temperature is obtained from the gas line or bottle at a stagnation pressure of 5-10 bar( $p_0$ ) and allowed to expand through a 30  $\mu\text{m}$  (diameter) nozzle into a chamber in vacuum in the  $10^{-3}$  mbar range maintained by a 500 l/s turbo pump. Nozzle geometries ranging from sharp edged orifice to a long tube capillary [Mur84] have been used to generate cold atomic and molecular beams, but a typical nozzle (Plano GmbH) used in the present set up has a geometry as shown in Fig. 3.7. The target gas atoms with low velocity before the nozzle are accelerated along the axis of the nozzle up to the speed of sound at the exit of the nozzle, provided the pressure ratio  $P_b/P_0$  is greater than 2.1 [Sch97, Mil88]. In this process we convert a random 3D distribution of velocities (due to the internal thermal energy and compressional energy) to a distribution with a preferred direction and a near- zero velocity spread in the transverse plane. The interaction of the supersonic flow with the low-pressure ambient gas environment produces a well-defined free-jet shock wave-system [Cam84], thus efficiently separating the cold ( $\ll 5\text{mK}$ ) isentropic jet from the warm background gas. Thus the supersonic expansion occurs in a 'zone of silence' as illustrated in Fig. 3.7. To achieve a supersonic gas beam a skimmer is placed inside this zone of silence which also limits the transversal jet size and the temperature distribution, thereby preventing the supersonic beam from collapsing. The nozzle mounted on a 3D piezo motion stage is, hence, aligned to be about 4-10 mm in line with the axis of a skimmer (Beam Dynamics Inc) with a dia. 200  $\mu\text{m}$ . The jet then expands into the second stage maintained at  $10^{-7}$  mbar with a 300 l/s pump followed by a second collimating skimmer (dia 400  $\mu\text{m}$ ) and finally into

the reaction chamber. The jet leaves the reaction chamber being guided through a conical cylinder into a dump chamber pumped by a separate 300 l/s pump.

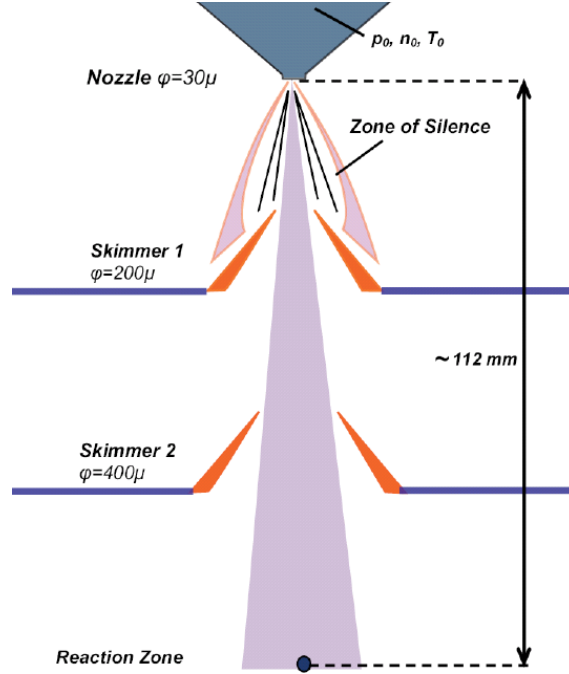


Figure 3.7: Schematic of the jet.

We begin with a reservoir of a mono atomic gas, just behind the nozzle with a stagnation pressure of  $p_0$ , a number density  $n_0$ , at a constant temperature  $T_0$ . As elucidated in [Sch97] a simple one-dimensional model can be used to derive the thermodynamic parameters, density,  $n_n$ , pressure,  $p_n$ , temperature  $T_n$ , and also the flow velocity,  $v_n$  at the exit of the nozzle:

$$n_n = \frac{3\sqrt{3}}{8}n_0, \quad (3.3)$$

$$p_n = \frac{9\sqrt{3}}{32}p_0, \quad (3.4)$$

$$T_n = \frac{3}{4}T_0, \quad (3.5)$$

$$v_n = \sqrt{\frac{5}{3} \frac{kT_n}{M}} \quad (3.6)$$

$$(3.7)$$

where  $k$  is the Boltzmann constant and  $M$  is mass of the target gas. The total number

of particles passing through the nozzle per second is, therefore, given by

$$N_n = v_n \cdot n_n \cdot A_n = \frac{3}{16} p_0 \sqrt{\frac{15}{kT_0 M}} A_n, \quad (3.8)$$

where  $A_n$  (the area of the nozzle) =  $\pi \cdot (R_n)^2$ . With  $T_0 = 273$  K,  $p_0 = 5$  bar and  $R_n = 15 \mu\text{m}$  we get  $N_n = 5.1 \cdot 10^{19} \text{ s}^{-1}$ .

The gas jet has the least cross sectional area at the nozzle and in the section following the nozzle, it achieves a final velocity  $v_{jet} = \sqrt{5kT_0/M}$ . In the case of helium, we may express this in terms of momentum as  $p_{jet} = 5.9$  a.u.. The jet expansion is assumed to be adiabatic and considering the flow using continuum theory as in [Mil88], the on axis density at a distance  $z$  down stream from the nozzle is related to the density in the reservoir  $n_0$  as follows:

$$n(0, 0, z) = n_0 \frac{z_{ref}}{z^2} \quad (3.9)$$

where  $z_{ref}$  is a scaling length obtained from the radius of the nozzle as  $z_{ref} = 0.806 \cdot R_n$  [Mil88]. At the reaction zone  $z = 112$  mm and for the pertinent parameters we obtain  $n = 1.5 \times 10^{12} \text{ cm}^{-3}$ . While it is clear that the temperature of the jet along the expansion direction is greater than in the plane perpendicular to it, obtaining estimates for them is a subject of long-drawn analysis, not in the least complicated by the existence of two skimmers. So it suffices to say in general [Mos09] that the temperatures measured are less than a few Kelvin along the jet direction, and in the order of few hundred mK perpendicular to the jet expansion direction.

### 3.4 The spectrometer

The guiding principle of the spectrometer is to extract the charged particles formed during the photon-target collision process, accelerate them through a constant homogeneous electric field such that the reconstructed trajectory yields the initial momenta with high accuracy and resolution. Any inhomogeneity of the field especially near the reaction zone, therefore, degrades the resolution of the spectra obtained. In the present spectrometer (Fig. 3.8), the electric field is provided by a series of 32 appropriately biased disk like laser-machined spectrometer plates separated by 7mm. The biasing voltages are provided by a resistor chain each with a resistance of  $180.2 (\pm 0.01) \text{ k}\Omega$ . At the end of the spectrometer plates, on either side is a 12 mm wide ring, separated from the last electrode by 10 mm. This ring serves to prevent the field lines from the grounded support (**S**) to penetrate into the homogeneous field region. The ring is biased such that we have a total acceleration region on either side of the reaction region to be 134.5 mm, from the reaction region to the edge of the ring. To note is that for each spectrometer plate the conducting area (metal filled part) is more than twice the transmitting area, thereby ensuring homogeneity in the transverse plane. We performed field lines and trajectory simulations (using TRICOMP) for the given geometry. Using protons with kinetic energies of up to 2 eV,

and with potentials applied to the electrodes so as to create a constant electric field of 9.36 V/cm in the accelerating region, we plot in Fig 3.9 the electric field lines (blue) and the ion trajectories (brown). At the end of the spectrometer, the high fields resulting from the high voltages applied on the detector (see section) lead to an unavoidable distortion of the field, leading to lensing effects on the trajectories of the charged particles. This is minimized by "closing" the spectrometer with a high transmission ( $\sim 85\%$ ) copper wire mesh which forces an equipotential surface to be formed at the transition region, shielding the spectrometer from the electric fields at the detector. Nevertheless, from the simulations we arrive at an electric field inhomogeneity of  $\Delta E/E$  on the order of  $10^{-4}$ , which is also borne out in the visual inspection of the trajectories in Fig. 3.9.

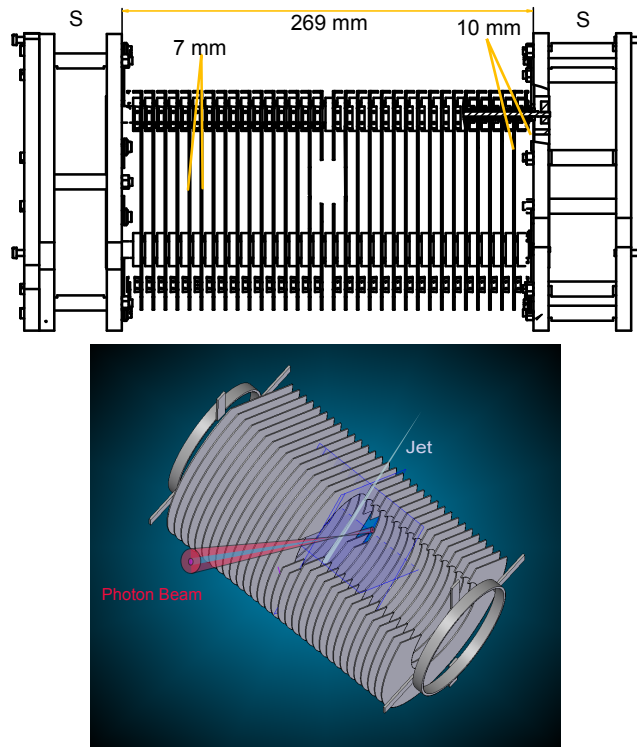


Figure 3.8: An illustration of the spectrometer. In the upper panel the side view of the CAD drawing of the spectrometer is shown.

Assuming the target atom (He,  $I_P = 24.5$  eV) is at rest, in a photoionization process with a 40 eV photon, an electron is liberated which carries away all the energy (nearly!), leaving the He ion with an energy in the meV range, making it essential to have a  $\mu\text{eV}$  resolution on the ion side of the spectrometer. Hence, one applies low extraction fields of few V/cm. While this is sufficient to obtain a  $4\pi$  acceptance for the ions, it is not sufficient to directly image the electron momentum. A detector diameter of 70 mm at a distance of about 135 mm, with an extraction voltage of 20 V has a  $4\pi$  acceptance for electron energies only up to 0.33 eV, which is at least 50 times lower than the typical electron energy

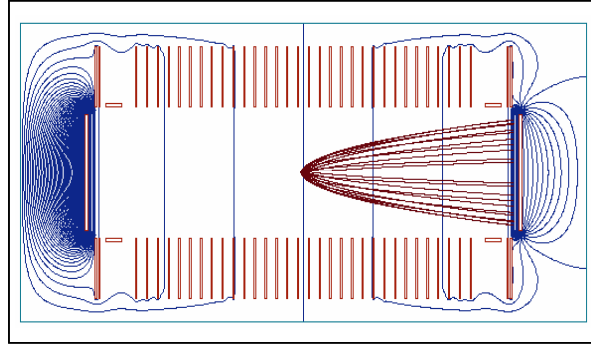


Figure 3.9: Field lines and trajectories simulation for the geometry of the spectrometer. Note that in the simulation we have neglected the entrance and exit holes for the photon beams. The brown curves indicate trajectories for 2 eV protons in an electric field of 9.36 V/cm. The blue lines are the field lines calculated from the simulation.

expected here. Increasing the extraction voltage is not a solution as it would destroy the momentum resolution for the ions and electrons. Therefore, an additional homogeneous magnetic field parallel to the spectrometer axis is applied to confine the electron motion to helical trajectories whose radii are determined solely by the initial transverse momenta and the magnetic field. Thus, we can increase the transverse acceptance of the electrons, which can be calculated from the magnetic field and the geometrical dimensions of the spectrometer as in 3.8.

The homogeneous magnetic field is provided by a set of circular Helmholtz coils, having an average diameter of 710 mm, and separated by 400 mm. The individual coils are composed of a long hollow copper tube (dia 8 mm) wound into 9 turns, in a 3 x 3 cross sectional matrix. Driven by a power supply (Delta Elektonika BV, SM 52-AR-60) capable of giving up to 60 A with a ripple of 15 mV pp we can expect to have a steady magnetic field of up to 18 Gauss. The tubings are cooled by running water flowing through them. The coils are placed outside the vacuum chamber, which is built of a non permeable steel (1.4429 ESU), to ensure no distortions of the magnetic field. Similarly, all the metallic components of the spectrometer and the detector are designed to be non-magnetic. With the spectrometer aligned nearly North-South, the magnetic field deviation due to the Earths Magnetic field is easily countered by slightly aligning the Helmholtz coils off-axis with respect to the spectrometer. Any residual distortions can be diagnosed from the spectra and corrected for in the off-line analysis. To be noted is that the design of the spectrometer omits a drift region, present in earlier versions to implement the so-called 'time focusing' [Fis03, deJ04] in the Wiley-McLauren condition. However, in this design the potential<sup>3</sup> loss of resolution

<sup>3</sup>Time-focusing plays an important role when a finite interaction width along the spectrometer axis leads to the same ionic species created at different points having different TOF, and thus a loss of resolution. Here, of course, we estimate the focal spot size of the XUV radiation to be  $\sim 200 \mu\text{m}$ , for which the effect is negligible

is offset by the smaller longitudinal extent of the spectrometer resulting in a more compact design for the Helmholtz coils. As seen in Fig. 3.2, the compactness of the Reaction Microscope allowed a shorter focal length for the focusing optics.

### 3.4.1 Detector

Recoil-ion and electron momentum imaging require large area position sensitive detectors with added capabilities of good position resolution ( $0.1 \text{ mm}$ ) and good time resolution ( $<1 \text{ ns}$ ). The first stage of the detector is the charge multiplication section, usually employing a large area Micro Channel Plate or MCP (Fig. 3.10). The MCP is essentially a micro fabricated array of several million channels, each with a diameter of a few tens of microns and working as an independent electron multiplier. The inner surface of the channel is coated with a semiconducting material, which serves as a secondary electron multiplier. The inner surface of the channel is coated with a semiconducting material, which serves as a secondary electron multiplier. A charged particle entering the channel releases secondary electrons from the wall of the channel. An applied electric field accelerates the secondary electrons, traveling in parabolic trajectories until they strike the channel surface repeatedly, thus producing a cascade of secondary electrons. Successive strikes yield a cloud of around  $10^7$ - $10^8$  electrons which emerge from the rear end of the MCP. The gain is further enhanced by firstly aligning the channels at an angle to the surface and, hence, to the incoming charged particle, and also by stacking a pair of such plates oriented in a so-called Chevron or Z-stack configuration.

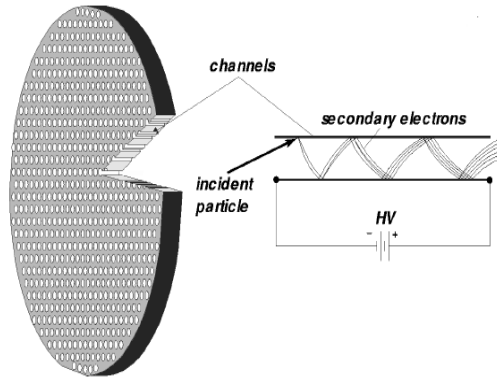


Figure 3.10: An illustration of a Micro Channel Plate (Taken from [Dur06])

### 3.4.2 Delay-line anodes

For both, ion and electron imaging, the position encoding is provided by a delay line anode. The basic principle of the delay-line anode is as follows. The electron cloud from the rear

of the MCP stack is accelerated through a homogeneous electric field to be imaged on a positively biased delay-line anode (DLA). The delay line, visualized in Fig. 3.11 is a bare copper wire wound across opposite edges of an insulating plate. Two crossed pairs of lines, isolated from each other form a tight 2D grid in x-y directions as shown in Fig. 3.11(b)). The electron shower on the grid causes image charge pulses to travel to the two ends of the delay lines, yielding four pulses for each particle hit, two on each delay line. The signal from the primary electron shower of the MCP is used to time the arrival ( $t_0$ ) of the charged particle. Let the propagation of the two pulses on the crossed delay lines be given by  $t_{x1}$  and  $t_{x2}$  and  $t_{y1}$  and  $t_{y2}$ . Given an effective signal velocity  $v_{signal}$  (close to speed of light) the position coordinates can be calculated as

$$x = v_{signal} \cdot ((t_{x1} - t_0) - (t_{x2} - t_0)) = v_{signal} \cdot (t_{x1} - t_{x2}) \quad (3.10)$$

$$y = v_{signal} \cdot ((t_{y1} - t_0) - (t_{y2} - t_0)) = v_{signal} \cdot (t_{y1} - t_{y2}) \quad (3.11)$$

$$(3.12)$$

The largest time for signal propagation is typically 70 ns for a square anode with 80 mm width. Since the propagation time from one end of the delay line to the other is a constant for a given delay line, the quantities

$$t_{xsum} = ((t_{x1} - t_0) + (t_{x2} - t_0)) = t_{x1} + t_{x2} - 2t_0 \quad (3.13)$$

$$t_{ysum} = ((t_{y1} - t_0) + (t_{y2} - t_0)) = t_{y1} + t_{y2} - 2t_0 \quad (3.14)$$

$$(3.15)$$

are constants. These sums are used as a consistency test for genuine events.

### 3.5 Signal processing and data acquisition

As elucidated in the preceding sections the extraction of TOF and position information of the charged particles reduces to accurate retrieval of the timing of the MCP and the corresponding DLA signals for each hit. The electron avalanche in the MCP leads to a drop in the applied voltage, which has a typical duration of 10 ns. The resulting pulse still needs to be amplified by a high bandwidth fast amplifier and further processed by a Constant-Fraction-Discriminator (CFD), before the timing information is digitized by a multi-hit Time-Digital-Converter (TDC), CAEN 1790 in our case.

The CFD is an electronic device which produces a standardized NIM<sup>4</sup> output, if the voltage exceeds an adjustable threshold. The CFD plays a major role in providing a near-jitter-free timing output which is independent of the original pulse height. Though the CFD is irreplaceable when it comes to obtaining the timing of the signals, it also severely affects the processing of two pulses arriving within a short time window. When the two

---

<sup>4</sup>Nuclear Instrumentation Module

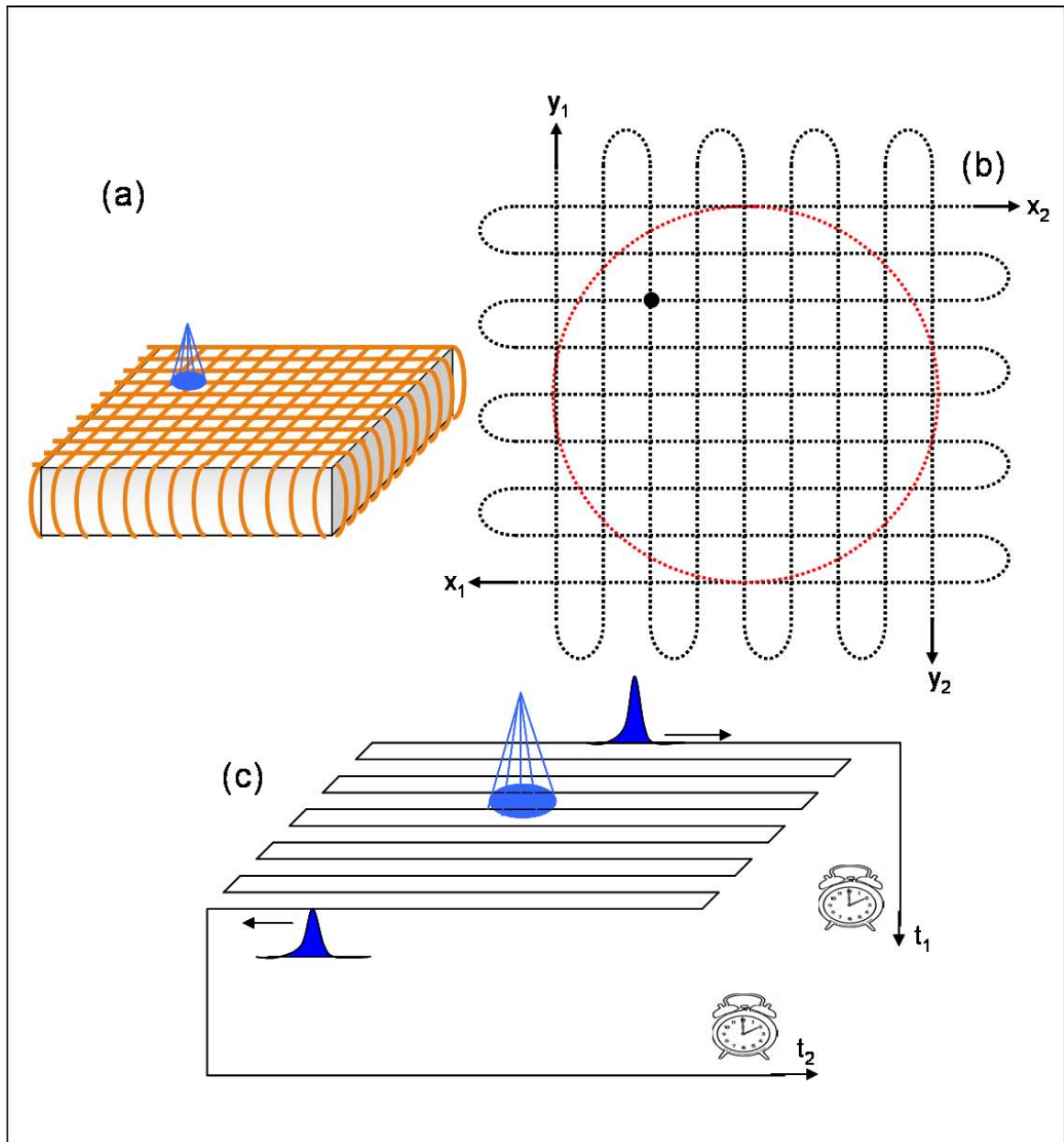


Figure 3.11: Illustration of the Delay Line.

pulses overlap, only the first pulse is processed properly. In the worst case situation the interference of the two pulses may altogether inhibit any output at all. As multiple hits are not being analyzed here, this limitation does not play any role in the present work.

The signals from the DLA are a bit more complicated as each delay line is actually a pair of isolated parallel wound wires which are spaced apart by 0.5 mm. The 'signal' wire is biased positively (by 50 V) with respect to the reference wire and, hence, the electron cloud is preferentially deposited on this wire. Any noise is picked up by both, the signal wire and the second 'reference' wire, and is eliminated by transformatively coupling the difference signal from both the wires. These DLA signals are then amplified, processed by CFD and digitized in separate channels of the TDC as shown in Fig. 3.12.

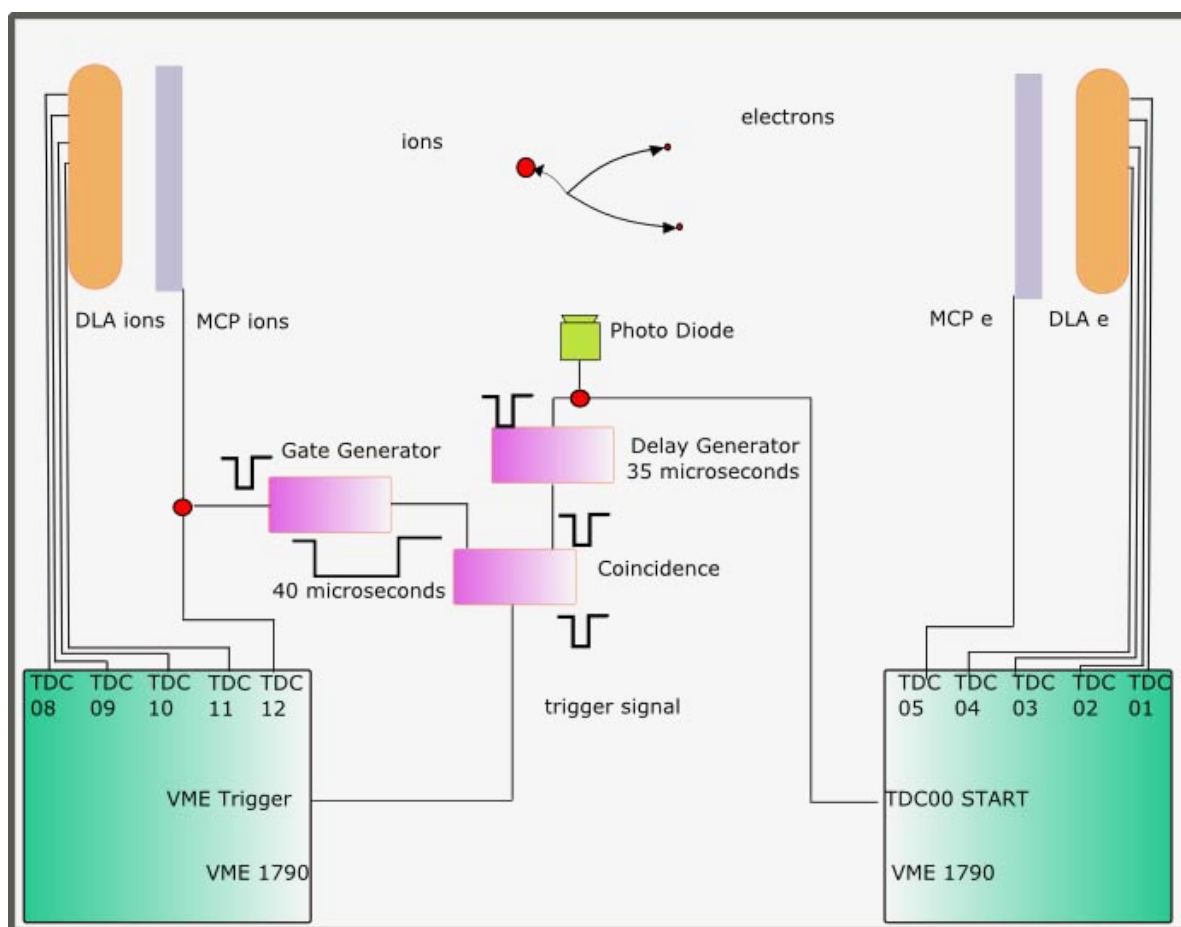


Figure 3.12: Electronics.

For all the hits which are processed by the electronics, the timing information is stored and buffered by the VME controller only if it is triggered. To generate this trigger, we note that the meaningful hits recorded by the detectors are those which follow the arrival of the photon pulse at the target. So the trigger to the the TDC is generated by the laser

photodiode signal, delayed by about  $35 \mu\text{s}$ . On the other hand, if an ion is detected, the ion MCP signal opens a gate of about  $40 \mu\text{s}$ . The delayed laser signal is compared with the gate in a logic AND circuit to finally provide the trigger signal. If the trigger signal is received, the VME controller looks into the stored hits of the TDC in a (programmable) time window of  $40 \mu\text{s}$  preceding the trigger. All the timing signals are stored as number of clock cycles from a common start (TDC channel 0) with each hit providing the stop signal on the channels. The timing signals from the MCPs and DLA signals from both the detectors are fed into separate channels as shown in the figure, providing the stop for each channel, while the common start is provided by the photodiode signal. The trigger signal, delayed by a few  $\mu\text{s}$  also initiates the transfer of the buffered data to an external PC through a network connection. In our case a dedicated PC then stores the data in a List Mode File format. The data can be processed on line or off line using a GUI-based program called Go4 developed by GSI, Darmstadt, capable of sorting the data from events, performing complex calculations, transformations, histogramming events and displaying the processed data

### 3.6 Reconstructing the momentum vector

The TOF of a charged particle ion or electron in the spectrometer, with charge  $q$  and mass  $M$  depends on the initial velocity, the length of the acceleration region,  $a$ , the length of the drift region,  $d$ , and the extraction voltage  $U$ . If the particle has an initial momentum,  $p_{\parallel}$ , along the spectrometer axis and  $p_{\perp}$  in the plane perpendicular to it, we may write the initial kinetic energy of the charged particle as it emerges in the reaction region as

$$E = \frac{p_{\perp}^2}{2M} + \frac{p_{\parallel}^2}{2M} = E_{\perp} + E_{\parallel} \quad (3.16)$$

with  $E_{\perp} = \frac{p_{\perp}^2}{2M}$  and  $E_{\parallel} = \frac{p_{\parallel}^2}{2M}$ . It is easy to show, solving Newton's equations of motion for a charged particle that the TOF is given by

$$t_{\pm} = \sqrt{M} \left[ \frac{\sqrt{2}a}{\sqrt{E_{\parallel} + qU} \pm \sqrt{E_{\parallel}}} + \frac{d}{\sqrt{2}\sqrt{E_{\parallel} + qU}} \right] \quad (3.17)$$

The ' $\pm$ ' sign denotes ions/electrons initially emitted in the direction, and opposite to that of acceleration. While being exact, eq. 3.17 is not very helpful in retrieving the initial longitudinal momentum. For ions a simplification of the above equation is possible, since the initial energy from the reaction is in the range of only a few meV, as compared to the energy gained in acceleration, which is in the order of a few tens of eV. Or stated in other words:  $E_{\parallel} \ll qU$ . We can then employ a Taylor expansion of the time-of-flight for the recoil ion ( $t_r$ ), about the time-of-flight for zero longitudinal momentum of the ion,  $p_{\parallel} = 0, E_{\parallel} = 0$  such that [Fis03]

$$t_r(p_{\parallel}) = t_0 + \left\{ \frac{dt_r(E_{\parallel})}{dE_{\parallel}} \cdot \frac{dE_{\parallel}}{dp_{\parallel}} \right\} \cdot p_{\parallel} \quad (3.18)$$

where

$$t_0 = \sqrt{M} \left[ \frac{\sqrt{2}a}{\sqrt{qU}} + \frac{d}{\sqrt{2}\sqrt{qU}} \right] \quad (3.19)$$

Now one may easily obtain from the above equations, the longitudinal momentum of the recoil ion in a.u. as

$$p_{\parallel} = 8.043 \times 10^{-3} \frac{qU}{a} [t_r - t_0] \quad (3.20)$$

While  $t_r$  is the measured quantity in ns,  $a$  is precisely obtained from the known geometry given in cm and  $U$  is the applied extraction potential in V. Finally, the symmetry of the reaction process allows us to choose the center of the TOF distribution for the ion in question as  $t_0$ .

The transverse momentum of the ion is encoded in the arrival positions of the ions  $(x_r, y_r)$  on the detector. Again, the position at which an ion with zero transverse momentum is detected is taken as the centroid  $(x_{r0}, y_{r0})$  of the distribution, which has an 'offset' due to the jet velocity (see Fig. 3.16). A helpful approximation would be to regard the arrival position to be independent of the longitudinal momentum. This is indeed true, as the relative TOF are of the order of few ns, as compared to the absolute TOF, which is in the order of few  $\mu$ s. Then the displacement of the ion with respect to the centroid can be written as

$$r = \sqrt{(x_r - x_{r0})^2 + (y_r - y_{r0})^2} = (2a + d) \sqrt{\frac{E_{\perp}}{qU}} \quad (3.21)$$

which can easily be inverted to obtain the transverse momentum

$$p_{\perp} = 11.6 \frac{\text{a.u.}}{\sqrt{\text{amu eV}}} \frac{r}{2a + d} \sqrt{qU.M} \quad (3.22)$$

The emission angle in the xy-plane can be calculated by  $\phi_r = \arctan((y_r - y_0)/(x_r - x_0))$ , and the momentum distributions along the x,y axis obtained:  $p_x = p_{\perp} \sin(\phi_r)$  and  $p_y = p_{\perp} \cos(\phi_r)$ .

### 3.6.1 Electron momenta

The retrieval of electron momenta is complicated by a) the helical trajectories of the electron in the magnetic field and b) the initial energy of the electron being of the same order as the acceleration energy. The latter implies that the linearity approximation used in eq. 3.20 to extract the longitudinal momentum is no longer valid, while the former implies that eq. 3.21 and eq. 3.22 to calculate the transverse momenta has to be modified for the electrons. The nonlinear equation for the longitudinal momentum is, therefore, solved numerically using the so-called Newton-Raphson's method. We begin by using the transformations  $T = (t/a)\sqrt{qU/2m_e}$ ,  $T_0 = d/2a$   $x = \sqrt{E_{\parallel}/(qU)}$ , where  $m_e$  is the mass of the electron to obtain

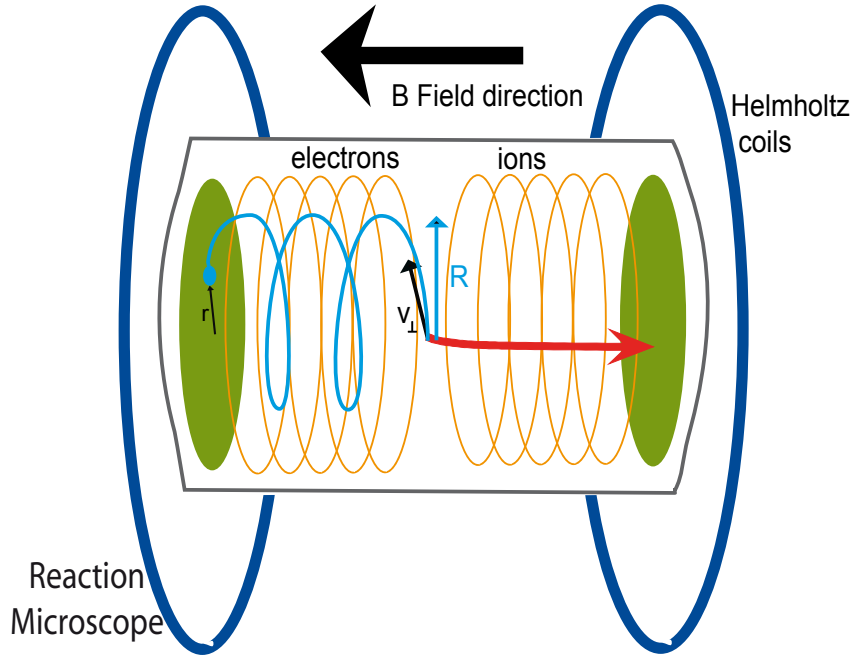


Figure 3.13: The helical trajectories of the electrons in blue, have a radius of  $R$  for an initial transverse component of the velocity  $v_{\perp}$ . Finally, the electron is detected on the detector at a radial displacement of  $r$  with respect to the center (of the distribution).

$$T = \frac{1}{\sqrt{1+x^2}+x} + \frac{T_0}{\sqrt{1+x^2}} \quad (3.23)$$

The idea behind the method is then to numerically find the zero-crossing value  $x$ , for the function  $f(x)$  defined by

$$f(x) = T - \frac{1}{\sqrt{1+x^2}+x} + \frac{T_0}{\sqrt{1+x^2}} \quad (3.24)$$

for each of the measured electron TOF values. Following an initial guess  $x_0$ , the function  $f(x_0)$  and the derivative  $f'(x_0)$  is iteratively used to obtain the new estimate  $x = x_0 - f(x_0)/f'(x_0)$ . The longitudinal electron momentum is then simply obtained in a.u. as ( $U$  in volts),

$$p_{\parallel} = x \cdot \sqrt{\frac{U}{13.6}} \quad (3.25)$$

The cyclotron motion of the electrons in the magnetic field ( $B$ ), while confining the electron to a transverse radius  $R$ , befuddles the initial transverse momentum information. Nevertheless, one can still recover it by simple equations based on the the familiar Lorentz Force Law. Equating the centrifugal force to the Lorentz Force we have (Fig. 3.13)

$$\frac{m_e v_{\perp}}{R} = qB \quad (3.26)$$

$$p_{\perp} = \frac{BR}{12.4} \text{ (in a.u.)} \quad (3.27)$$

$$(3.28)$$

with the magnetic field,  $B$ , in Gauss, and  $R$  in centimeters. If  $r$  is the radial displacement of

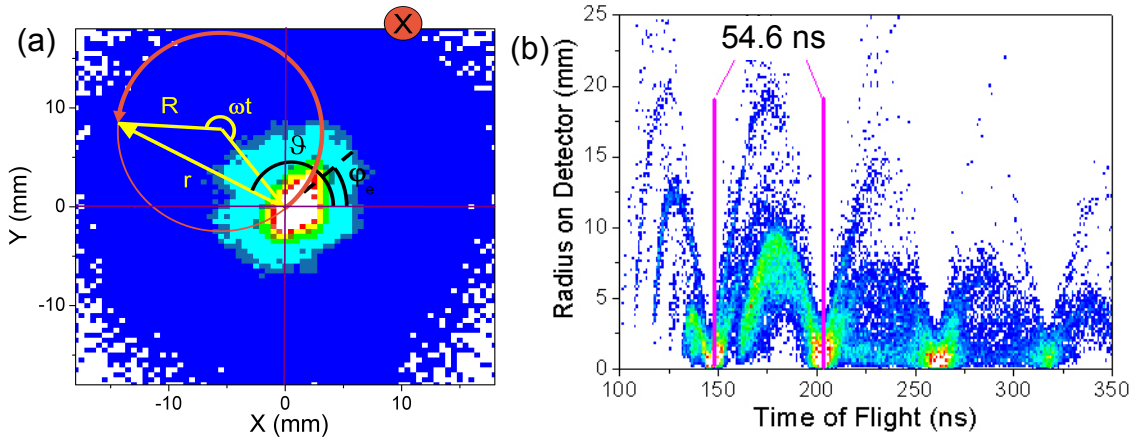


Figure 3.14: (a) The position spectra of the electrons in a linear colour-coding scheme. For an electron detected at  $r$ , the projection of the helical trajectories onto the detector plane gives the trace (bold orange) with a net radial angle of  $\omega t$ . The initial angle of emission is given  $\phi_e$  and the polar angle in the detector plane is  $\vartheta$ . (b) The spectrum of the detected radial position of the electron (linear scale) as function of its time-of-flight indicates equispaced nodes on the TOF axis, where the helical trajectories for different initial momenta of the electron end up on the spectrometer axis at the position of the detector. At these nodes, which are given by TOF values which are an integer multiple of the cyclotron time period of the electron, all information about the initial transverse momentum is lost.

the position  $(x_e, y_e)$  the electron strikes the detector, then  $r = \sqrt{(x_e - x_{e0})^2 + (y_e - y_{e0})^2}$ , where  $x_{e0}, y_{e0}$ , is the centroid of the position distribution on the electron detector. As shown in Fig 3.13, the electron arrives at this point passing through  $\omega.t/(2\pi)$  turns in the magnetic field. Here,  $t$  is the TOF of the electron and  $\omega$  is the cyclotron frequency given by

$$\omega = \frac{qB}{m_e} \quad (3.29)$$

Then one can relate the radial position on the detector to the cyclotron radius as follows

(see Fig. 3.14(a))

$$r = \frac{R}{2 |\sin(\omega t/2)|} \quad (3.30)$$

allowing us to calculate the magnitude of the transverse momentum as

$$p_{\perp} = \frac{rB}{24.8 |\sin(\omega t/2)|} \quad (\text{in a.u}) \quad (3.31)$$

Further, from the angle on the detector  $\vartheta = \arctan(y_e/x_e)$ , the azimuthal angle of emission  $\phi_e$  is easily obtained by  $\phi_e = \vartheta - \omega t/2$ .

A glance at the above equations reveals that while  $r$  and  $\vartheta$  are directly measurable from the position spectra of the electrons, one only needs to precisely measure the magnetic field in the spectrometer to obtain the transversal momentum of the electron. The apparently formidable task of precisely measuring the magnetic field within the spectrometer is overcome using the knowledge of the trajectory of the electrons and is described in the next section. Another expected bottleneck would be obtaining the absolute TOF of the electron  $t$ , the solution to which is also described in the following section.

## 3.7 Calibration

The accurate calculation of the ion momenta hinges on the precise knowledge of the homogeneous electric field. While one can expect that close to the detector region, the field lines deviate from homogeneity as seen in the Fig. 3.9, of significance to the calculation of the ion momenta is the value of the electric field at the center of the spectrometer, where one can assume it is homogeneous to a much better precision. The electric field generated at the center of the spectrometer is only decided (to a good approximation) by the voltages ( $U$  in eq. 3.20) applied at the ends of the accelerating region and a precise knowledge of the length of the accelerating region ( $a$ ). Since the acceleration region on the ion side is known to be 134.5 mm, we only need to accurately note the value of  $U$ . As discussed earlier, the values of  $x_{r0}, y_{r0}, t_0$  in eq. 3.21 and eq. 3.20 are obtained from the centroid of the distribution in the position spectra of the ions, and the TOF respectively. This constitutes the calibration step for the ions.

On the electron side the first step is to determine the cyclotron time period of the helical motion ( $t_{cyc} = 2\pi/\omega$ ) of the electron. This is done by plotting the radial position of the electron as a function of the electron TOF as in Fig 3.14(b). The helical motion of the electron has the following consequence: electrons with flight times which are integer multiples of the cyclotron time period ( $t = n \times t_{cyc}$ ) return to the spectrometer axis (dubbed as 'magnetic focusing'). As seen in Fig 3.14(b), they appear as 'nodes' in the spectrum close to  $r = 0$ . While all information about the initial transverse momenta of these electrons is lost, there is, however, an advantage of these nodes. The 'nodes' are spaced by  $t_{cyc}$ , and using eq. 3.29 one can obtain the magnetic field to a precision of less than 1%. What still remains to be determined is the absolute TOF of the electrons, or corollarily the absolute zero of the measured TOF. Since the absolute zero of the measured TOF also corresponds

to a node in the spectrum in Fig. 3.14(b), we can extrapolate the time positions of the nodes in steps of the cyclotron time period to earlier times, to arrive at the absolute zero of the measured TOF( $t_{inf}$ ). In other words  $t_{inf} + n \times t_{cyc}$  should be a position of a node on the measured TOF.

The values of  $U, a, d$  in eqs. 3.23-3.31, are to the first approximation obtained from the applied potential and known spectrometer geometry. But this is still not precise enough to reconstruct the electron momenta. The reason is that since the electron momenta is arrived at using the absolute TOF, the field the electron experiences all through its trajectory in the acceleration region and the short drift region before the MCP, needs to be accounted for in the calibration. Obtaining a precise value of the different potentials is not feasible, but this is circumvented using the knowledge of the physical process at hand. In collisions with photons, the momentum transfer by the photon is negligible so that the ion and electron momentum balance each other. For example, in single ionization with photons, the spectrum of the sum of the longitudinal momentum of the singly charged recoil ion and the coincident electron,  $p_{||}^r + p_{||}^e$  should be strongly peaked around  $\sum p_{||} = 0$ , as in Fig. 3.15(a). Furthermore a spectrum of  $p_{||}^e$  vs  $p_{||}^r$  (Fig 3.15(b)) should be strongly distributed around an imaginary straight line inclined at  $-45^\circ$  to the vertical. The parameters are then fine-tuned to optimize these two spectra and thus finally calibrate the spectrometer.

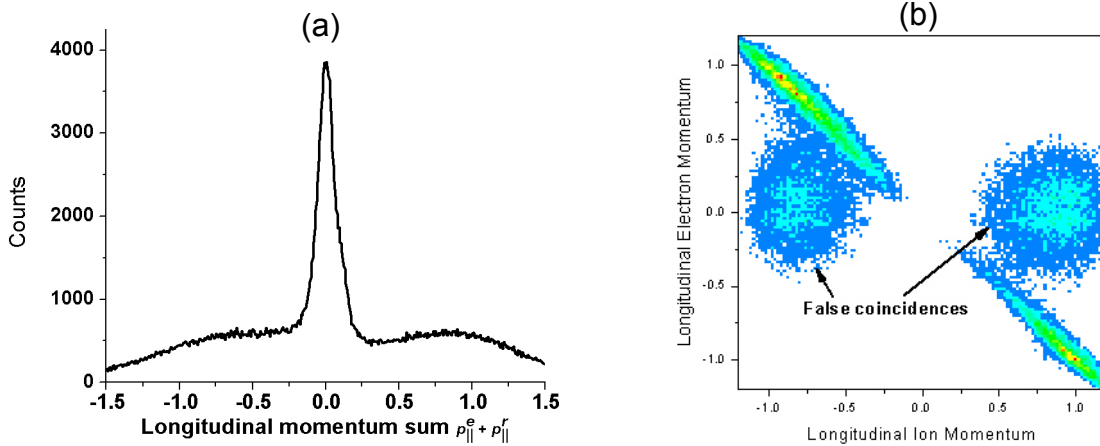


Figure 3.15: (a) The sum momentum spectrum for the longitudinal ion and electron momenta is sharply peaked around  $\sum p_{||} = 0$ . (b) The longitudinal ion momentum plotted versus the longitudinal electron momentum is strongly distributed about a line with a slope of -1. The other events which do not lie on this slope are false coincidences arising from electrons ionized from the rest gas.

### 3.8 Resolution and acceptance

The maximum kinetic energy of a fragment, emitted in a particular direction, that can be detected by the spectrometer, defines its acceptance. The acceptance is mainly limited by the geometry of the spectrometer and the applied fields. For example, there is no restriction on fragments emitted in the direction of the detector, along the spectrometer axis. However, if an ion (or electron) is emitted away from the ion (electron) detector, then it is easy to see that if the initial longitudinal momentum exceeds a certain value  $p_{\parallel}^{max}$  for a given extraction voltage  $U$ , then the field can no longer turn the ion (electron) back towards the detector within the acceleration region. Thus, a charged particle with negative longitudinal momentum greater than

$$p_{\parallel}^{max} = \sqrt{2mqU} \quad (3.32)$$

can no longer be detected. However, even for a very low electric field of 1 V/cm,  $U = 13.45$  V, and the upper limit on the detected longitudinal momentum,  $p_{\parallel}^{max}$  is  $\sim 10$  a.u. for helium ions. This is easily sufficient as the longitudinal momentum of singly charged ions created in photoionization of atoms considered in this work hardly crosses 2 a.u. (Chap. 4). But in molecules, for example with fragmentation energies of 10 eV in  $H_2$ , the protons emerge with momenta of about 40 a.u., and accordingly the extraction voltage has to be increased. Similarly, it can be shown that the transverse acceptance of the spectrometer for ions, with a detection radius of  $R_{det}$  and extraction voltage  $U$  is given by

$$p_{\perp}^{max} = R_{det} \frac{\sqrt{2mqU}}{2a} \quad (3.33)$$

For example, in dissociation of deuterium, with an extraction voltage of 400 V, and a detection radius of  $R_{det} = 3.5$  cm, we obtain a maximum transverse acceptance of  $p_{\perp}^{max} = 52$  a.u.. So deuterons with kinetic energies of up to 10 eV can be detected in all directions, which is of interest in the experiments described in Chap. 5. The electrons are radially confined by the magnetic field, so that the maximum transverse momentum detected for a given magnetic field  $B$  and detection radius  $R_{det}$  is given from eq. 3.31

$$p_{\perp}^{max} = BR_{det} \quad (3.34)$$

For a magnetic field of 15.6 G, we can, therefore, detect electrons up to a maximum of 64.6 eV.

The momentum resolution of the spectrometer is limited by a couple of factors. An obvious sources of error would be inhomogeneities in the electric field, which, however, we may ignore as seen from the field simulations for this spectrometer. However, in the detection of ions, it is clear to see that the initial thermal velocity of the atomic beam would translate to a momentum uncertainty. For example, as mentioned before, the temperature of the jet being about 1 K in the jet direction ( $y$ ), it corresponds to an energy width of  $\Delta E_{therm} = 3/2k_B T = 0.13$  meV. For Helium, this would lead to momentum uncertainty  $\Delta p_{therm}^x = 0.26$  a.u.. From geometric considerations it is easy to see that for a jet width of

$\sim 1$  mm at a distance of  $\sim 10$  cm downstream from the nozzle, the maximum momentum uncertainty along the  $x$  and  $z$  axes, would, therefore, be  $\Delta p_{therm}^x = \Delta p_{therm}^z = 0.12$  a.u. [Fis03].

The detection uncertainty of about  $\delta t = 1$  ns for the time-of-flight, and  $\delta r = 1$  mm for the position on the detector further degrades the momentum resolution as follows [Fis03]:

$$(\Delta p_z)^2 = (\Delta p_{therm}^z)^2 + (8.039 \times 10^{-3} \frac{\text{eV}}{\text{a.u. c.m}} \frac{qU}{a} \delta t)^2, \quad (3.35)$$

$$(\Delta p_x)^2 = (\Delta p_{therm}^x)^2 + (11.6 \frac{\text{a.u.}}{\text{amu eV}} \frac{\sqrt{qUM}}{2a} \delta r)^2, \quad (3.36)$$

$$(\Delta p_y)^2 = (\Delta p_{therm}^y)^2 + (11.6 \frac{\text{a.u.}}{\text{amu eV}} \frac{\sqrt{qUM}}{2a} \delta r)^2. \quad (3.37)$$

So for the experimental conditions leading to results detailed in Chap. 5, i.e., extraction voltage 403 V and for deuterons, we would finally expect

$$\Delta p_z \approx 0.25 \text{ a.u.}, \quad (3.38)$$

$$\Delta p_x \approx 1.2 \text{ a.u.}, \quad (3.39)$$

$$\Delta p_y \approx 1.2 \text{ a.u.} \quad (3.40)$$

The experimental longitudinal momentum resolution for the recoil ion is obtained using the sum-momentum spectrum of Fig. 3.15, where the FWHM of the distribution around  $\Sigma p_{||} = 0$  a.u. corresponds to the recoil-ion momentum resolution  $\Delta p_z$ <sup>5</sup>. For an extraction voltage of 403 V the longitudinal momentum resolution for the deuterons was found to be 0.3 a.u., closely corresponding to the predicted value. Similarly, the experimental resolutions in the transverse directions,  $x$  and  $y$ , were also obtained from the sum-momentum spectra,  $\Sigma p_x$  and  $\Sigma p_y$ , respectively, and confirmed to match with the theoretical predictions.

The electron momentum uncertainty due to the thermal motion of the atoms is negligible. Rather, the origin of widths in the distributions is due to detection uncertainty and has been analyzed in great detail in [Fis03, Dur06]. Summarizing the salient points here, we have for a large range of electron TOF from 100-250 ns,  $\Delta p_z \sim 0.02$  a.u., as applicable for the experimental conditions in Chap. 4. For TOF less than 100 ns, the resolution worsens exponentially. So for the experimental conditions leading to the results in Chap. 5, with a TOF of 64 ns for the electron with zero longitudinal momentum, the resolution is  $\sim 0.06$  a.u.. The transverse momentum resolution for the electrons [Fis03, Dur06] depends on not only the instrumental widths, but also on the position on the detector and the time-of-flight. Nevertheless, for the experiments we are considering here, with  $B = 15.6$  Gauss, we estimate the transverse momentum resolution at best to be  $\sim 0.1$  a.u., between the nodes, while the resolution diverges at the nodes.

---

<sup>5</sup>as seen later in this section, the contribution of electron momentum resolution is negligible when compared to that of the ions

### 3.9 Performance and experimental procedure

In this section we use the example of an experiment we carried out using the setup described till now to illustrate its performance and also to highlight the procedure followed in experiments at the MPI-K HHG laboratory. In brief, 25 fs (FWHM) pulses at 776 nm, with a pulse energy of 1 mJ, at a repetition rate of 8 kHz were obtained from the Dragon amplifier. The beam was split with a 30% beam splitter. The more energetic part of the beam was focussed into a Ar-gas cell at stagnant pressures of ranging from 40 to 170 mbar to generate the XUV harmonics. The harmonics passing through a 200 nm Al filter were spectrally filtered to suppress the lower order harmonics, allowing only harmonics within a window with a sharp lower energy cut off at 20 eV. The higher energy part of the XUV pulses is limited by the HHG cut off ( $3.17U_p + I_p$ ), and was determined to be  $\sim 42$  eV in the XUV spectrometer. The XUV light was then focussed using the grazing incidence mirror pair onto the target gas, helium, in the Reaction Microscope. Since the XUV beam line is fixed, the overlap of the XUV beam and the atomic beam is optimized by translating the Reaction Microscope in the direction perpendicular to the XUV beam direction. At optimum conditions, we record a count rate of  $\sim 2$  kHz for the recoil ions (target gas : He). From the areal density of the gas target  $10^{11}$  cm $^{-2}$ , and the cross section for photoionization for He at 30 eV photon energy  $\sim 5$  Mb [Mar08], it is easy to calculate the photon flux at the target to be  $\sim 5 \times 10^9$  photons in a second.

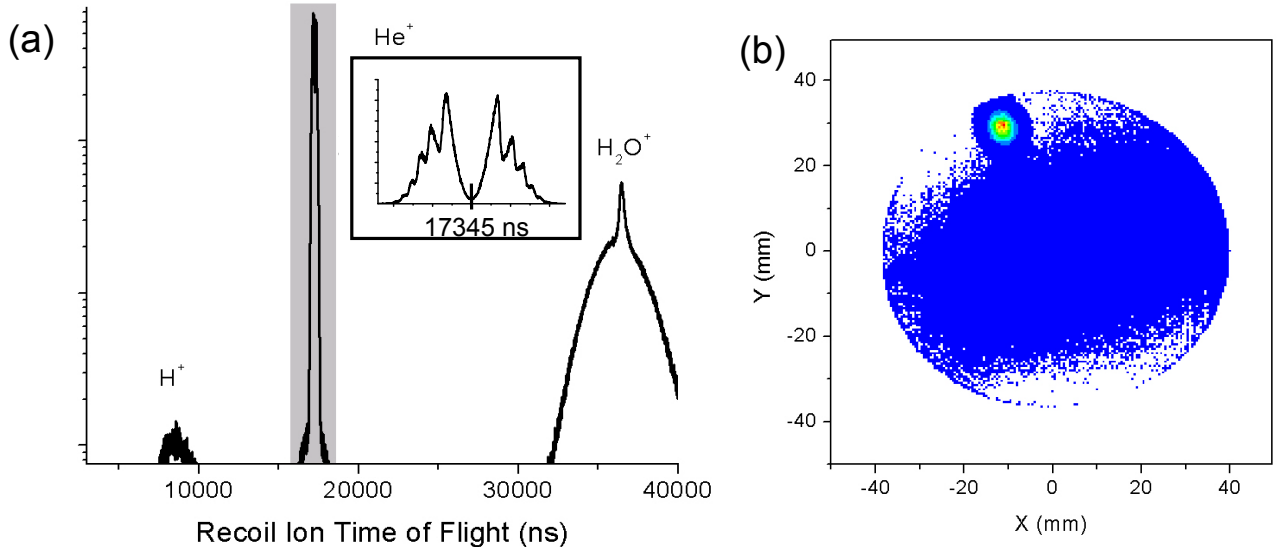


Figure 3.16: (a) The recoil-ion time-of-flight spectrum. In the inset the distribution within the shaded region is expanded and plotted with greater resolution. (b) The position spectrum of the recoil-ions.

A low electric field of 0.44 V/cm is applied in order to extract the ions with maximum acceptance and best resolution (see § 3.8 for details on the acceptance

of the spectrometer). In Fig. 3.16(a) we plot the TOF spectra of the recoil ions and depending on the mass over charge ratio various ionic species can be identified. The sharp peak around TOF  $\sim 17345$  ns corresponds to  $\text{He}^+$  ions, where ions which initially flew towards the recoil-ion detector following photoionization are detected at a TOF less than  $t_0 = 17345$  ns (see inset). The ions which flew away from the recoil-ion detector are turned around by the electric field and detected at greater TOF values. Having correctly identified  $t_0$ , the TOF for ions with zero initial longitudinal momentum, we can obtain the longitudinal momentum spectrum  $p_{\parallel}$  (or  $p_z$ ) for  $\text{He}^+$  ions through eq. 3.20 and plot it in Fig. 3.17(a). It is easy to see that the spectrum consists of peaks, where, the spacing of the peaks  $\Delta p_{\parallel} \propto \sqrt{2\omega}$ ; here  $\omega \sim 0.06$  a.u corresponds to 775 nm, the fundamental wavelength of the driving IR laser field. This confirms that the momentum spectrum is indeed a mapping of the XUV photon spectrum onto the photoelectrons, modified by the cross section of the target atom  $\text{He}$ .

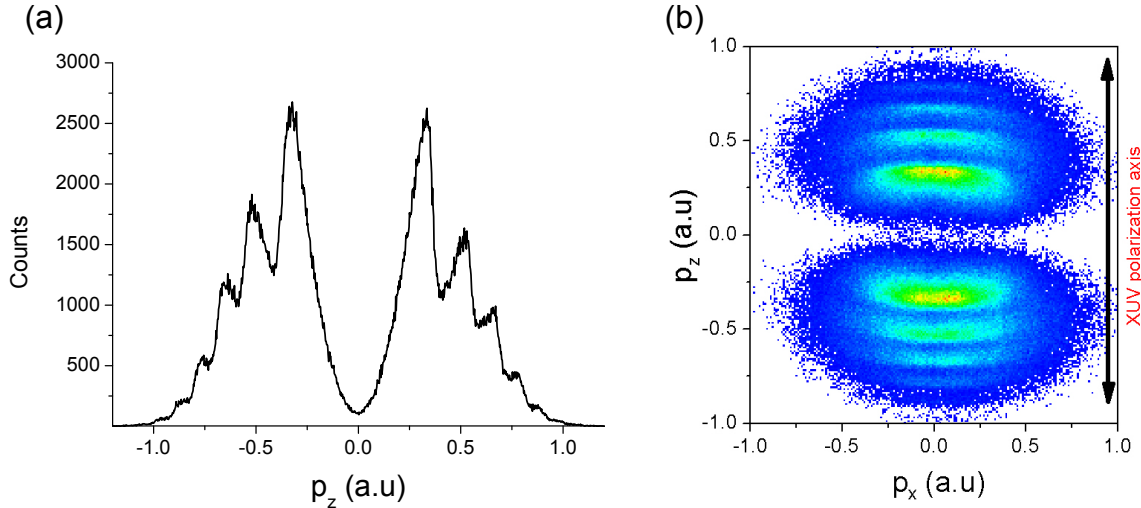


Figure 3.17: (a) The projection of the recoil-ion momentum distribution onto the spectrometer axis, or the longitudinal momenta  $p_z = p_{\parallel}$ . Five Harmonic peaks are seen above the ionization threshold of He, 24.6 eV, implying the observed cut off in the Reaction Microscope is  $\sim 42$  eV. (b) The projection of the recoil-ion momentum distribution onto the plane containing the polarization axis of the XUV pulses, and an axis in the plane perpendicular to it.

To obtain the 3D recoil-ion momentum spectra, we inspect the position spectra of the recoil ions in Fig. 3.16(b). The ionization of the rest gas is visible as a broad line of events across the detector image. At the top left we notice an intense elliptical distribution. By selecting events in the TOF spectra which correspond to  $\text{He}^+$  (shaded area in Fig. 3.16(a)), we can confirm that this elliptical distribution is indeed of  $\text{He}^+$  ions. The displacement of the distribution from the center of the detector is easily understood as the supersonic atoms in the jet have an initial velocity of  $p_{jet} = 5.9$  a.u. in the transverse direction at

the time of the photoionization. The electric field being longitudinal does not affect this component of the initial velocity, and the ions from the jet are detected off center. This allows a basic filtering of the true events from the background based on their position of the detector. Now, the transverse momentum components are calculated simply through the eq. 3.22 and the 3D momenta are obtained. Finally in Fig. 3.17(b), we plot a projection of the 3D momentum distribution onto the plane  $xz$ , where to reiterate,  $x$  is an axis in the plane perpendicular to the spectrometer axis, and  $z$  is along the spectrometer axis<sup>6</sup>.

As discussed in Sec. 3.6.1, the helical trajectories of the electron in the magnetic field introduce 'nodes' in the transverse momentum spectra where the electron TOF is equal to an integer multiple of the cyclotron frequency of the electrons in the magnetic field of the Reaction Microscope and, accordingly, the transverse resolution diverges. The number of nodes in the spectrum can be controlled by applying appropriate electric and magnetic fields. So, to present the electron momentum spectra here, we applied an electric field of 9.2 V/cm, with a magnetic field of 15.6 Gauss<sup>7</sup> such that only a single node is present in the spectra.

An important point should be noted in experiments with the Reaction Microscope involving coincident detection of more than one fragment in a single event. That is, for example, if we aim to detect both the ion and the electron in a photoionization process, we need to be sure that the coincident electron-ion pair emerge from the same photoionization event. A simple thumb rule to ensure this is to have ion count rates to be less than one-third the repetition rate of the laser pulses [deJ04]. However, with XUV pulses, if the pressure in the reaction chamber is high ( $> 5 \times 10^{-9}$  mbar), then ionization from the rest gas along the path of the XUV can lead to further false coincidences. This would require us to work at lower count rates.

To analyze the electrons, we need to first select only those electrons which were detected in coincidence with the ionic species of interest, here  $\text{He}^+$ . A further filtering of the electrons is done applying the zero momentum sum condition on the spectrum Fig. 3.15. In Fig. 3.18(a) we plot a 2D representation of the momentum distribution, where on the horizontal axis is the longitudinal momentum  $p_z$  and on the vertical axis is the radial transverse momentum  $p_{\perp}$ , i.e., in the plane perpendicular to the spectrometer axis. Once again, the hemispherical rings correspond to the photoelectrons from ionization by the harmonics. The single node in the spectrum, at around  $p_z = 0.2$  a.u. manifests as vertical artifacts in the spectrum, where the transverse resolution vanishes. On closer inspection, one also notices that the resolution for  $p_z < 0$  a.u. is better than for  $p_z > 0$  a.u.. This highlights the discussion in the previous section, where the longitudinal momentum resolution for the electrons depends on the actual TOF of the electrons. Therefore, for electrons with  $p_z > 0$  a.u. which have lower TOF values, the resolution is worse as compared to the resolution for electrons with higher TOF, i.e., for  $p_z < 0$  a.u.. We can now also obtain the electron energy distributions  $E_e = 13.6 * (p_z^2 + p_{\perp}^2)$  in eV, which is plotted as the black curve in Fig. 3.18(c).

<sup>6</sup>here it is also the polarization axis of the radiation

<sup>7</sup>determined through the cyclotron frequency

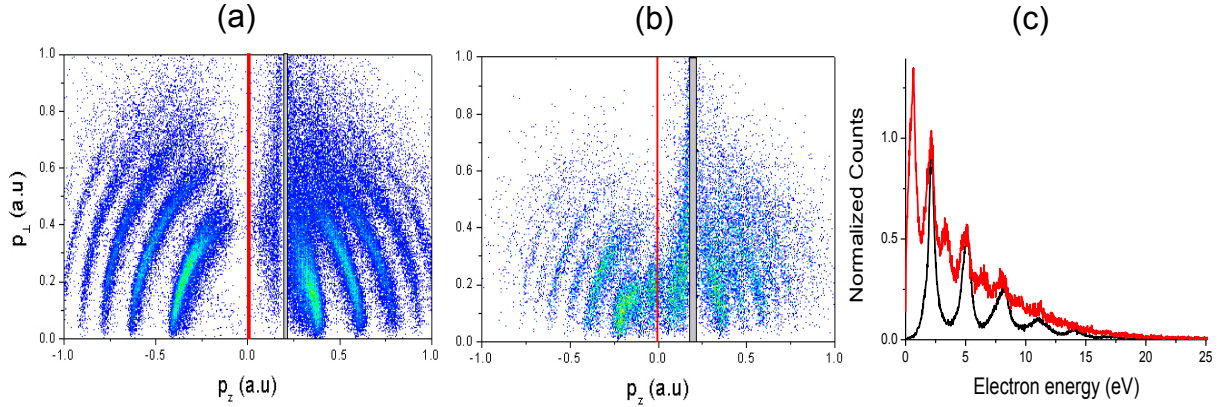


Figure 3.18: (a) The 2D electron momentum distribution for ionization with only HHG pulses and (b) with a time overlapped IR dressing pulse. (c) The electron energy distribution for photoelectrons with only HHG pulses shown in black. In red the electron energy distribution is plotted for XUV+IR pulses, normalized to the first main line at  $\sim 2.1$  eV.

### 3.9.1 Two-colour photoionization

In § 2.5 we pointed out that photoionization using APTs in the presence of a dressing IR laser field, leads to the production of sidebands exactly between the fundamental harmonic peaks in the photoelectron spectrum. In the experiment, the XUV pulses and moderately intense ( $\sim 10^{13}$  W/cm<sup>2</sup>) IR pulses were spatially and temporally overlapped to the nearest approximation through the optical method described in § 3.2. The overlap was optimized in the Reaction Microscope by maximizing the intensity of the sidebands observed in the electron energy spectrum. In Fig 3.18(b), we plot the 2D electron momentum distribution, where, when compared to Fig 3.18(a), the sidebands are clearly visible. In Fig 3.18(c) the corresponding electron energy spectrum is plotted in red.

From the discussion in § 2.5 it is clear that the two-colour photoionization experiment gives a method to characterize the XUV pulses, through the behavior of the sidebands when the relative delay,  $\tau$ , between the XUV and the IR pulses is varied. Plotted in Fig. 3.19(a), is the experimental longitudinal ion momentum spectra as a function of the XUV-IR delay. The transverse momentum is limited to 0.1 a.u.. Negative delays correspond to the IR pulse arriving ahead of the XUV pulse. The time delay is introduced by moving the Mechanics stage in steps of 0.5  $\mu$ m, corresponding to an optical delay of 3 fs, through the LABVIEW program interfacing the hardware controller of the Mechanics translation stage. The instantaneous position signal from the Mechanics controller is read by the same LABVIEW program and converted to voltage signal between 0.2 and 3.8 V, by interfacing with a USB controlled digital function generator Handyscope HS3 (TiePie Engineering). The ion and electron acquisition are not synchronized with the movement or position of the translation stage. Rather, the position signal from the TiePie Function Generator is read

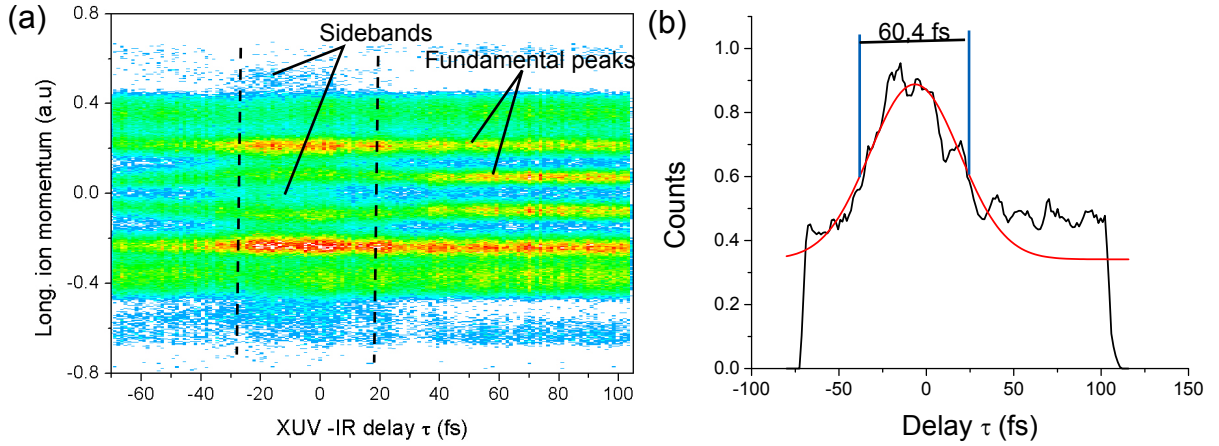


Figure 3.19: (a) The longitudinal ion momentum spectra as a function of the XUV-IR delay identifying the sidebands and the fundamental peaks. (b) A projection of the spectrum between  $p_{\parallel} = 0.1$  a.u. and 0.2 a.u. on to the delay axis (black), with a corresponding Gaussian fit (red).

into the ADC channel 0 of the ADC module CAEN 785N, with a 12 bit resolution, triggered by the same signal as the TDC (see § 3.5). Thus, for every event, the corresponding relative position of the translation stage is recorded in the ADC signal. The plot is essentially the plot of the ion spectra as a function of ADC signal, rescaled to represent in the plot, the time delay.

In the overlap region,  $\tau = -25$  fs to 20 fs, the sidebands are indicated in the Fig. 3.19(a), between the fundamental peaks. The fundamental lines are independent of delay, except, in the overlap region, where the intensity of the fundamental peaks are redistributed between the sidebands and the fundamental peaks. The projection of the sideband between  $p_{\parallel} = 0.1$  a.u. and 0.2 a.u. onto the delay axis is shown in Fig. 3.19(b), and has a Gaussian width of 60.4 fs.

The data presented here were acquired over 12 hours, attesting to the long term stability of the interferometric setup. However, we fail to see any sub-cycle oscillation of the sidebands as expected from § 2.5. In order to investigate the cause for this, we tested the Mach-Zehnder interferometric setup using an IR-IR experiment, recording the variation of the intensity as the delay between the two branches is varied. In particular, the CCD chip of the camera was replaced by a photodiode, so that the intensity variation of the fringes with delay could be recorded. In Fig. 3.20(a), we plot the intensity on the photodiode (red) acquired continuously as the position is varied. The feedback signal indicating the measured position of the stage by the controller is also displayed in black. The photodiode signal show random jumps, which indicates that the movement of the delay stage is unreliable especially when moved in short steps of less than 500 nm. That the random jumps were indeed caused by the overshoot of the Mechonics piezo of the delay stage was confirmed, when we compared its performance with an expansion piezo stack. To be noted

is that the Mechanics stage uses a linear piezomotor, providing translation in controlled steps. On the other hand by continuously ramping the voltage on the expansion piezo provides a smooth translation. The photodiode signal now shows the classic  $\cos^2$  variation of the intensity with delay as shown in Fig. 3.20(b). Thus we conclude that in the present setup using the Mechanics stage, we are limited to a minimum step size of  $0.5 \mu\text{m}$ , thereby precluding experiments on delay time scales of less than 3 fs. However, the experiments described in Chap. 5 were single pulse measurements, thereby independent of the performance of the delay stage. At the time of writing of this thesis, the delay stage setup was being modified so as to include a high precision, translation stage (Physik Instrument GmbH, Model:Hera) for future experiments.

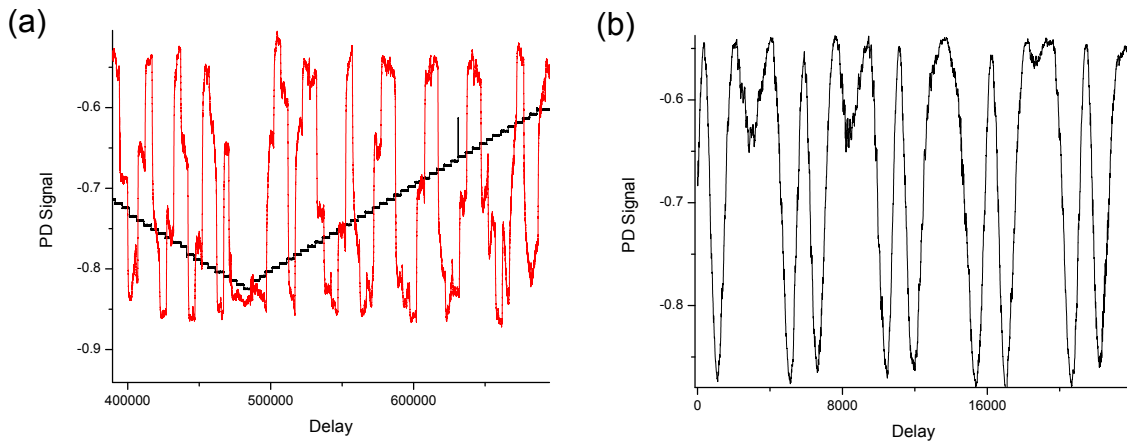


Figure 3.20: (a) The movement of Mechanics piezo stage is tested by observing the IR-IR Mach-Zehnder interference fringes using a photodiode. In the plot, the photodiode signal is plotted in red, as a function of the delay. Simultaneously the position of the stage as measured by the Mechanics Controller is plotted in black. (b) The photodiode signal when the translation is provided by a piezo stack element.

### 3.10 Experimental setup at Max-Planck Institute for Quantum Optics (MPQ), Garching

A part of the work presented in this thesis was carried out at the attosecond beam line AS-1 in MPQ, Garching under the aegis of a collaboration. Essentially, a Reaction Microscope was transported from MPI-K and coupled with the AS-1 beam line [Sch07] delivering ultrashort IR pulses. The setup generating waveform-controlled, intense, sub-5 fs IR laser pulses is described in detail in [Gou05]. Here, a brief description will be given with the aid of Fig. 3.21.

Essentially, pulses with energy  $\approx 900 \mu\text{J}$  with pulse durations of about 25 fs were obtained from a commercial femtosecond laser system (Femtolasers GmbH). The IR pulses

with a central wavelength of 805 nm were loosely focused into a hollow core silica fiber with an entrance diameter of  $260\ \mu\text{m}$ , filled with neon gas at a stagnant pressure of  $\sim 2$  bar. At the exit, the spectrally broadened, but chirped pulses are compressed by 4 pairs of chirped mirrors to obtain nearly transform limited  $\sim 5$  fs pulses at  $\sim 400\ \mu\text{J}$ . An interesting facet of this ultrashort laser setup is the control over the waveform of the pulses. For such ultrashort pulses, as will be discussed in the next chapter, control over a parameter known as the Carrier Envelope Phase (CEP) allows control on the magnitude and sign of the electric field at the peak of the envelope of the pulse. The laser system here employs active feedback loops to stabilize the CEP of the pulses with a stability better than 15% over a few hours.

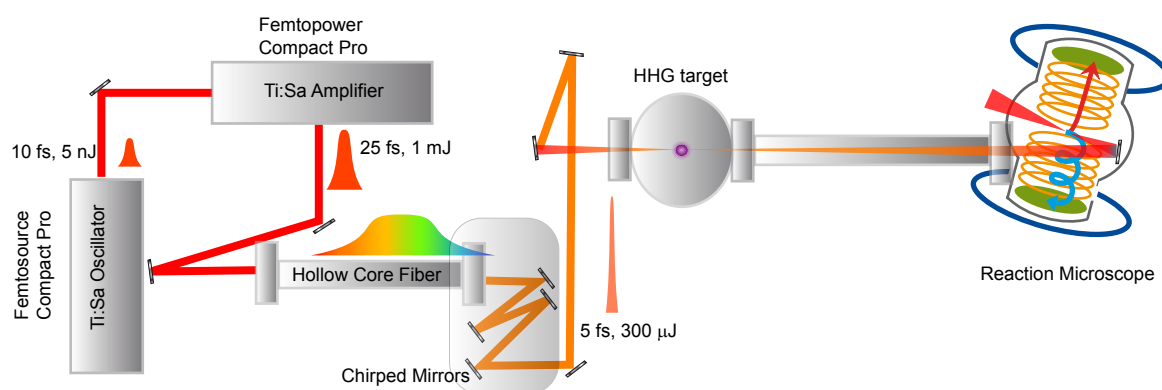


Figure 3.21: The experimental setup at MPQ, Garching. For the experiments described in Chap. 4, the gas flow to the HHG target was cut off, so that no harmonics were generated, and the unused IR was focused into the gas target of the Reaction Microscope.

The IR pulses propagated in vacuum to be intercepted by a focusing mirror about 3 m downstream (Fig. 3.21). At the focus of the 126 mm focal length silver mirror, the IR beam crossed the supersonic atomic beam of the Reaction Microscope. This REMI, designed and built at MPI-K, Heidelberg and used in Garching is similar to the one described earlier in this chapter. In fact, as mentioned before, the present design was based on this prototype so the description so far in Sec. 3.3 and Sec. 3.4 is valid in general. However, for exact details on the construction we refer to [Dew06].

# Chapter 4

## Electron Wave Packet interference in ionization with few-cycle laser pulses

Ionization of rare gas atoms such as helium at laser intensities in the range of  $10^{14}$ - $10^{15}$  W/cm<sup>2</sup> is usually described by the tunneling process as introduced in §2.2.1. In brief, the valence electron tunnels through the field suppressed barrier, at the peak of the electric field. The electron then undergoes an oscillatory motion in the electric field to achieve a final momentum, also known as the drift momentum. The process known as Above-Threshold-Ionization (ATI) has been widely studied in detail [Bec02] over the years, for a large variety of laser fields with different pulse lengths, intensities and photon energies. However, the study of this process assumes contemporary importance with the availability of few-cycle laser pulses [Mil06]. In this chapter we present the results of the first three-dimensional momentum imaging of Electron Wave Packet (EWP) interference observed in the ATI of helium with sub-5 fs pulses. We begin by describing ionization dynamics in the intense field of a few-cycle laser pulse, leading to the mechanism for EWP interference in ATI.

### 4.1 Strong field dynamics using few-cycle laser pulses

For a few-cycle laser pulse [Bra00] e.g. sub-5 fs at 800 nm with a single cycle time period of 2.7 fs, there is only one full oscillation of the electric field within the FWHM of the envelope. Therefore, there exist two extreme possibilities for the electric field within the pulse. In the first case Fig. 4.1(a), the local maxima (absolute) in the oscillation of the electric field coincides exactly with the maximum of the envelope of the field. The other extreme is when the maximum of the envelope coincides with the zero-crossing of the electric field, as illustrated in Fig. 4.1(b). Naturally, one can imagine fields between these extremes and also fields where the sign of the electric field is reversed (Fig. 4.1(c) and (d)). In a more formal sense, we can assign a parameter to each of these fields, a phase factor,  $\phi_{CEP}$ , or Carrier Envelope Phase (CEP) varying continuously between 0 and  $2\pi$ . Then, in the Slowly Varying Envelope Approximation (SVEA) [Bra00], the electric field can be

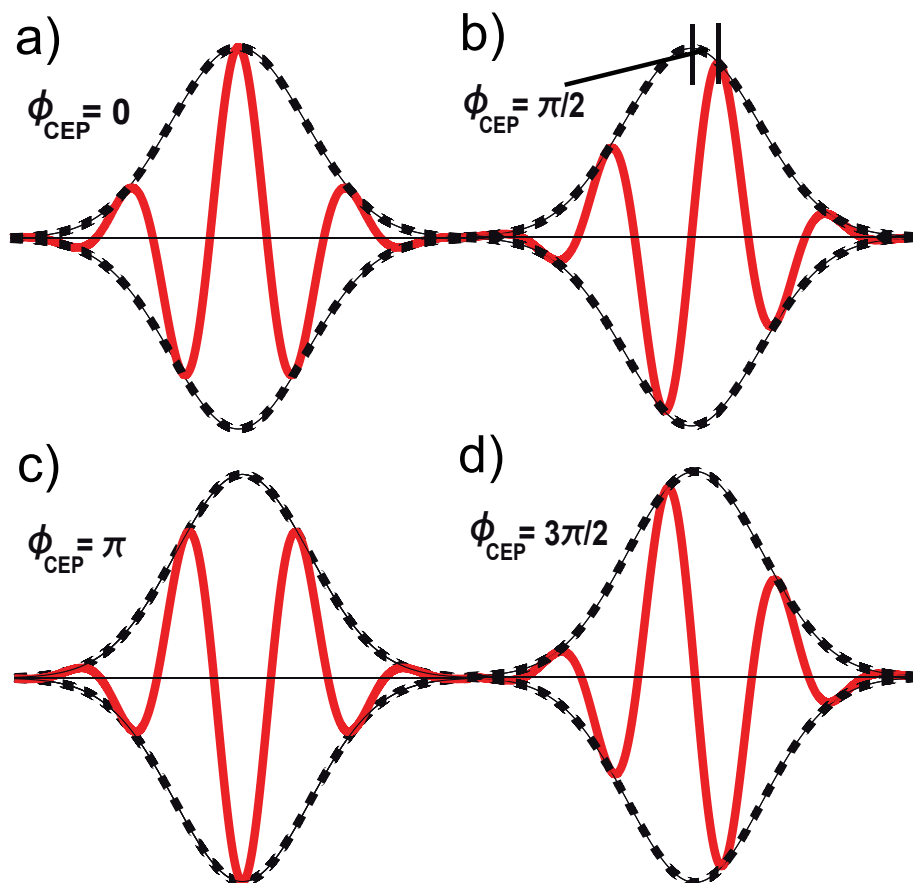


Figure 4.1: The electric field (red) for an ultrashort pulse with a FWHM of 5 fs for the pulse envelope (broken black curve) can be described as  $E(t) = E_0(t) \cos(\omega t + \phi_{CEP})$ . (a) The field is said to be cos-like when  $\phi_{CEP}$  is zero, and the maximum of the field coincides with the maximum of the envelope. (b) When the maximum of the envelope coincides with the zero-crossing of the field,  $\phi_{CEP} = \pi/2$  then the field is said to be sine-like. (c) and (d) are examples of pulses which are cos-like and sine-like, respectively, except for a change in the sign of the electric field.

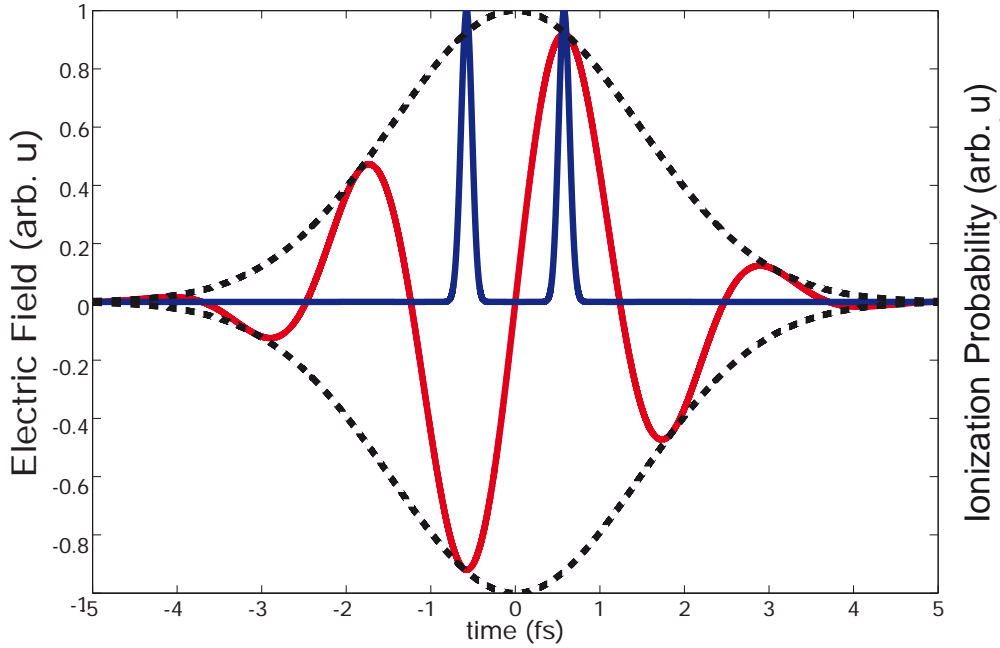


Figure 4.2: The relative, instantaneous, contributions to the ionization probability (blue) from different cycles of a few-cycle pulse scales nonlinearly with the instantaneous intensity  $I(t) = E(t)^2$  as  $I(t)^{I_p/\hbar\omega}$  (2.22), where  $I_p$  is the ionization potential, which for He is 24.6 eV, while  $\hbar\omega = 1.62$  eV. In a linear scale the contributions from the field maxima, other than the most intense ones, are not visible.

written as  $E(t) = E_0(t) \cos(\omega t + \phi_{CEP})$ . The CEP,  $\phi_{CEP}$ , thereby is defined as the phase difference between the envelope maximum and the nearest maximum of the electric field and represents a new parameter which not only offers a control on the amplitude but also the sign of the electric field at the maximum of the envelope.

The development of laser technology leading to intense few-cycle laser pulses with control over the CEP [Gou05], has opened up a plethora of possibilities in strong field physics. For example, the ionized electron can be steered in a direction dependent on the CEP of the pulse, which is the principle of the stereo-electron spectrometer [Pau03], or stereo-ATI, a device used to measure the CEP of a few-cycle laser pulse. This control over the electron motion in the continuum using CEP controlled sub-5 fs pulses has been used to generate the world-record 80-attosecond pulses [Gou08] through the process of HHG (see § 2.3). Furthermore, to name a few applications in atomic and molecular physics, CEP stabilized few-cycle laser pulses have also been demonstrated to control the localization of electrons in molecular dissociation [Kre09a, Kli06].

In particular, for a highly nonlinear process such as tunneling in the field of a few-cycle laser pulse, we are justified (Fig. 4.2) in confining the discussion to a single cycle around

the maximum of the pulse envelope. As introduced in §2.2.2, within a single cycle of the pulse, electrons emitted at different times are detected with drift momenta (eq.2.32) that depend on the vector potential at the time of birth of the electrons. Within the same cycle two tunneling phases, symmetrically spaced around the zero-crossing of the field, for a sine-like pulse, will lead to the same momentum (red, blue curves in Fig. 4.3). In reality, there are no two electrons being emitted at different times. Rather, in quantum mechanics, we speak of contributions to the probability amplitude of detecting the same final momentum state. It can, however, be shown, that associated with a single final momentum state, say,  $p$  (in Fig. 4.3), are two main contributions, which in fact, correspond to the two classical trajectories<sup>1</sup>,  $p(t_1)$  and  $p(t_2)$ , sketched in Fig. 4.3. The interference of these two contributions, therefore, modulates the probability of detecting an electron in different momentum states, i.e., the momentum spectrum. In a semi-classical picture, within a single cycle we can imagine Electron Wave Packets (EWPs), associated to the same final momentum, being created at two different times, which interfere in the momentum domain, at the detector. It is pertinent to contrast this with the case of ionization with a multiple-cycle pulse considered in §2.2.2, where the periodicity of the laser pulse leads to interference of the EWPs from different periods. The interest in sub-cycle interferences goes beyond mere curiosity to the possibility of developing a very novel technique in interferometric imaging of ultrashort dynamics in atoms and molecules. As first outlined in [Spa04] and detailed in [Arb06], the electron wave packet  $EWP_1$  that was launched at  $t_1$  - red curve in Fig. 4.3 - collides with the ionic core thereby being modified in phase and wave-front direction (often dubbed "Coulomb-focusing") and overlaps with an unaffected "reference" wave  $EWP_2$  (of the same electron!) launched at  $t_2$  (blue curve in Fig. 4.3) and leading to the same final momentum. A 3D momentum image of this EWP interference, therefore, represents a time-dependent hologram of the modulations imposed onto  $EWP_1$ . Since, as will be shown later, this interference is sensitive on  $t_1$  and  $t_2$  on an attosecond time scale, the ultrafast dynamics of the electron cloud bound to the ion might be imprinted and can potentially be reconstructed for atomic, molecular and cluster targets.

In direct analogy, the interaction of the returning  $EWP_1$  with the parent ion core to retrieve atomic or molecular structure and dynamics through High Harmonic Generation, has been the basis for experiments in, for example [Ita04] and [Bak06]. In a molecule such as  $N_2$ , the electron predominantly tunnels through the Highest Occupies Molecular Orbital (HOMO), and when is driven back to the molecule, the emitted HHG spectrum contains spatial Fourier components of the orbital. In the so-called tomographic reconstruction process, the angular distribution spectrum of the harmonics is inverted to retrieve the shape of the orbital. Alternatively, the angular distribution of of the returning electron, back-scattered off the parent ion, can be used extract the elastic scattering cross sections [Oku08, Mor09]. More recently, interferences with EWPs generated by attosecond pulse trains and steered by an infrared laser pulse [Rem06] have been demonstrated to image the coherent scattering of electrons from the parent ion [Mau08].

---

<sup>1</sup>in case we neglect the presence of the Coulomb field, (see §2.2.2), which is the premise of the Strong Field Approximation

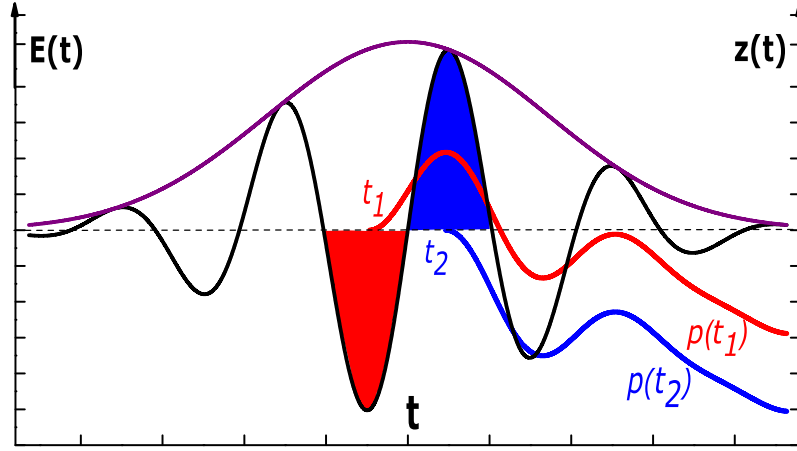


Figure 4.3: Electron trajectories in an ultrashort pulse, with  $\phi_{CEP}=\pi/2$ . Electrons born at times  $t_s$ , ( $s = 1, 2$ ), symmetrically placed with respect to the zero-crossing, end up with the same momentum  $p(t_s)$  following the example-trajectories given by the red and blue curves respectively :  $p(t_s)=-\int_{t_s}^{\infty} E(t)dt$ , in atomic units. The right hand axis is the displacement of the electron from  $z=0$ .

In this chapter we report on the first demonstration of sub-cycle EWP interferences seen in high-resolution, 3D low-energy electron (ion) momentum distributions for single ionization of He by CEP-stabilized few-cycle pulses, investigated by a Reaction Microscope. Momentum distributions along the laser polarization axis ( $p_{||}$ ), not only show a CEP-dependent preferential emission to either hemisphere, but also a corresponding asymmetric occurrence of interference peaks. The spacing between the peaks, significantly smaller than  $\Delta p_{||} \propto \sqrt{1 \cdot \hbar\omega}$  as observed for longer pulses (see Sec. 2.2.1), is compared with a simple Strong Field Approximation (SFA)-based model. This model invokes the interference of only two quantum paths for wave-packets EWP<sub>1</sub> and EWP<sub>2</sub> leading to the same final drift momentum, hence, capturing the basic mechanism of holographic imaging. 2D electron spectra ( $E_e < 15$  eV) reveal regular interference stripes, parallel to the transverse momentum ( $p_{\perp}$ ) axis in the hemisphere of enhanced emission, and radial structures in the opposite hemisphere, in good qualitative agreement with theoretical predictions [Arb06].

## 4.2 The experiment

In the experiment, linearly-polarized CEP stabilized 5 fs pulses at 740 nm with a repetition rate of 3 kHz were obtained at the AS-1 attosecond beamline at the Max-Planck-Institute for Quantum Optics (MPQ), Garching [Sch07]. The experimental setup for the production of such ultrashort laser pulses has been covered in detail in [Gou05]. The laser beam, with intensities up to  $0.4 \text{ PW/cm}^2$  ( $I_0$ ) at the focus of a 125 mm spherical Ag-mirror was crossed with a supersonic, cold He jet ( $\sim 10^{11}$  atoms/cm<sup>2</sup>) in the ultra-high vacuum chamber

( $\sim 2 \cdot 10^{-10}$  mbar) of the Reaction Microscope. As detailed in the preceding chapter, the created ions and electrons were guided to two position sensitive channel plate detectors by weak electric ( $\sim 2$  V/cm) and magnetic ( $\sim 0.8$  mT) fields, applied along the laser polarization axis. An important fact in experiments involving the CEP of the laser is the acquisition of a Gouy-phase shift [Lin04] of  $\pi$  in traversing through the focus of a Gaussian laser beam. This would imply that we cannot associate a single CEP at any given time. However, the washing away of the CEP can be minimized by having the focal position slightly before the actual jet position, so that in the interaction volume there is no slipping of the phase. Superior momentum resolution along the polarization axis (the spectrometer axis) was achieved reaching  $\Delta p_{\parallel} < 0.02$  a.u. for both, ions and electrons. Along the transverse directions (i.e. in the plane perpendicular to the laser polarization), the ion momentum resolution varied from  $\sim 0.5$  a.u. along the gas jet direction to  $< 0.1$  a.u. in the direction perpendicular to the jet. The transverse momentum resolution for electrons was on the level of 0.05 a.u.. The CEP of the laser field was varied in steps over a range of  $2\pi$  radians. For each of the phases, the two dimensional position and time-of-flight spectra for the ions and electrons were recorded in coincidence, and 3D momentum distributions were obtained.

### 4.3 Results

Depending on the CEP, the projections of the recoil ion (electron) momentum distributions along the laser polarization axis show an asymmetry about  $p_{\parallel} = 0$ . We can parameterize this asymmetry using

$$a(\phi_{CEP}) = \frac{(P_+(\phi_{CEP}) - P_-(\phi_{CEP}))}{(P_+(\phi_{CEP}) + P_-(\phi_{CEP}))}. \quad (4.1)$$

$P_{\pm}$  is simply the number of ions detected, which initially flew towards, or away from the detector so  $a(\phi_{CEP})$  indicates the 'left-right' asymmetry [Pau03]. While we do not measure the absolute CEP, we fix the phase  $\phi_{CEP} = 0$  for the CEP with the most symmetric distribution and in the inset of Fig. 4.4, plot  $a(\phi_{CEP})$  against  $\phi_{CEP}$ . There is a clear progressive shift of the asymmetry from negative to positive and back, demonstrating the consistency of these measurements. In particular, a change of phase by  $\pi$  inverts the distribution ( $a(\phi_{CEP}) = -a(\phi_{CEP} + \pi)$ ), and a shift by  $2\pi$  reproduces the original distribution ( $a(\phi_{CEP}) = a(\phi_{CEP} + 2\pi)$ ). Having identified the points of maximum (and opposite) asymmetry, we proceed to plot in Fig. 4.4 (a), (b) recoil-ion momentum distributions  $p_{\parallel}$  for these phases. In Fig. 4.4 (a), for  $p_{\parallel} > 0$ , we see peaks, which mostly disappear for  $p_{\parallel} < 0$ . When we change the phase by  $\pi$  in Fig. 4.4 (b), the visibility of the peaks is almost exactly mirrored about  $p_{\parallel} = 0$  (black line) as illustrated by the thin blue curve, an exact mirror image of Fig. 4.4 (a), highlighting the quality of the ion (and electron) momentum measurement as well as the CEP stabilization over time. For intermediate phases (Fig.4.5)

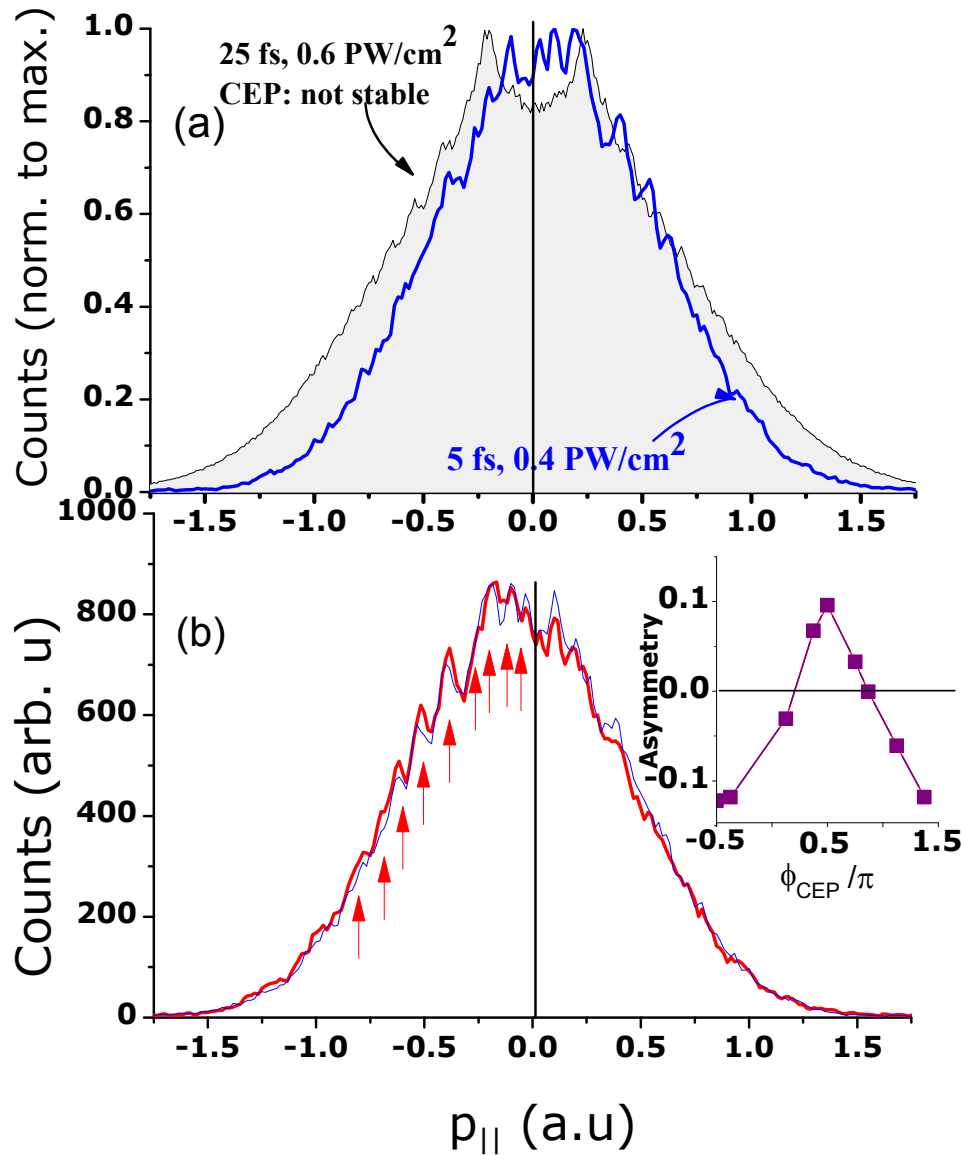


Figure 4.4: (a) Recoil-ion ( $\text{He}^+$ ) momentum distributions along the laser polarization axis for CEP with maximum asymmetry towards positive momenta and (b) at  $\phi_{CEP} = \pi/2$ . Shaded curve: ion momentum distribution at a similar intensity but for longer, 25 fs pulses normalized to the integral under the blue line. The thin blue curve in (b) is a mirror image of the blue curve in (a). (Inset) Asymmetry parameter  $a(\phi_{CEP})$  at discrete CEP phases.

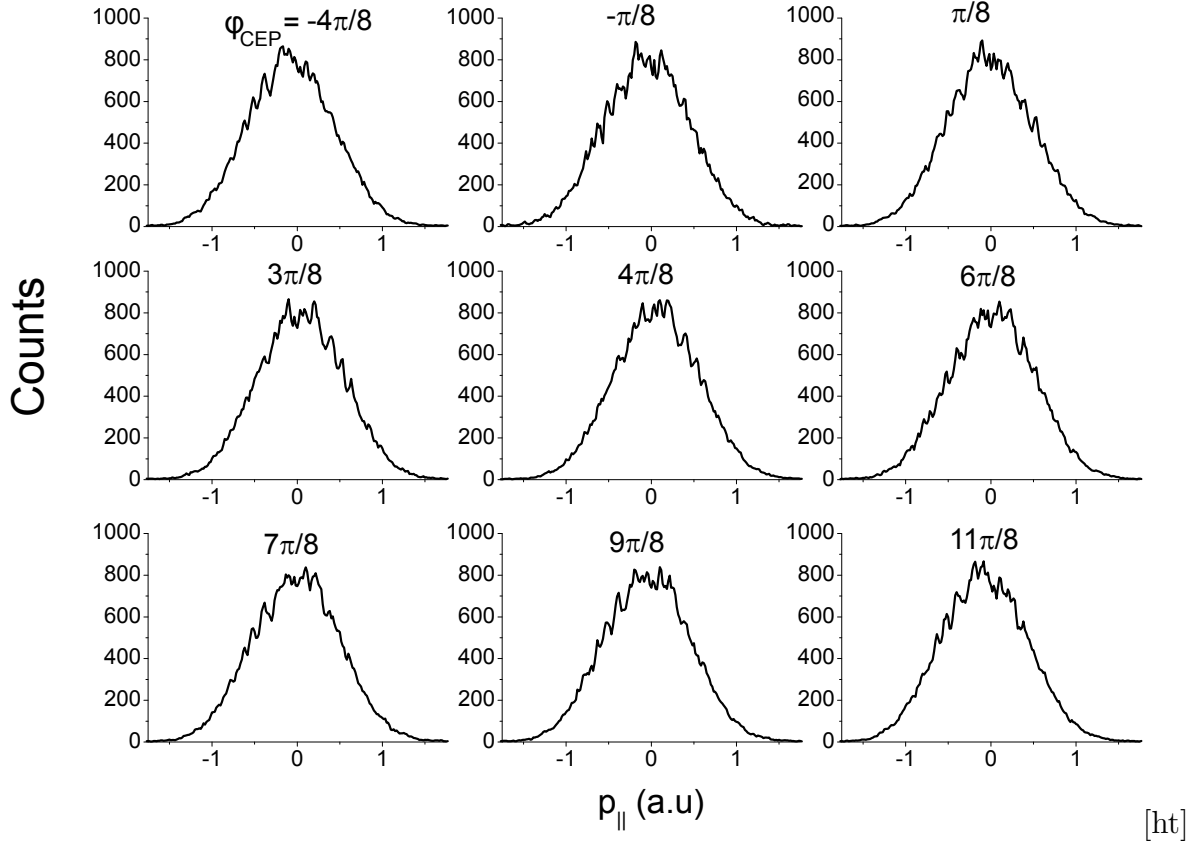


Figure 4.5: Recoil-ion ( $\text{He}^+$ ) Momentum distributions ( $p_{||}$ ) along the laser polarization axis for different CEP. The spectra show a continuous progression from an asymmetric spectrum, with the peaks on the  $p_{||} < 0$  side for  $\phi_{CEP} = -4\pi/8$ , to a symmetric spectrum for  $\phi_{CEP} = -\pi/8, \pi/8$  and finally to a mirrored asymmetry for  $\phi_{CEP} = 4\pi/8$ . The visibility of the peaks is reduced for the phases with least asymmetry, though the positions remain the same

the visibility of the peaks becomes progressively less pronounced and symmetric about  $p_{||} = 0$  for  $\phi_{CEP}=0$ , while maintaining their positions.

The momenta ( $p_{||}$ ), where interference peaks occur in Fig. 4.4, are plotted in Fig. 4.6 (red full circles) and compared to the results of previous measurements for 25 fs, non-CEP stabilized pulses (blue open circles) at 790 nm [Rud04]. The latter structures have been intensively discussed in the literature and were found to be stable in position over large intensity ranges, clearly visible deep into the tunneling regime [Rud04]. Obviously, the slope of the progressive peaks in this experiment differs drastically from the 25 fs data, which are in excellent agreement with a square-root Above Threshold Ionization (ATI)-like behavior (black curve) where the spacing between peaks corresponds to the photon energy, i.e. to 0.057 a.u. (790 nm). The spacing between the here-observed peaks, however, is much smaller pointing to the fact that in ultra-short pulses interferences emerging from

wave-packet emission at the maxima of the oscillating electric field, i.e. at the carrier frequency corresponding to the photon energy of  $\hbar\omega$ , is widely suppressed! Instead a new, quite regular spacing emerges which now turns out to be nearly linear as a function of  $p_{\parallel}$ .

The 2-D electron momentum distribution, presented in Fig. 4.7 for a phase with maximum asymmetry, reveals quite parallel interference stripes along the momentum transverse to the polarization direction for  $p_{\parallel} > 0$ . Close to  $p_{\parallel}, p_{\perp} = 0$  (red line) we see signatures of radial structures for  $p_{\parallel} < 0$ , indicating enhanced emission at certain angles, rapidly transforming into a more stripe-like pattern for  $p_{\parallel} > 0$ . These spectra are in excellent qualitative agreement with TDSE calculations for a pulse with only a single cycle within the FWHM of the pulse Fig. 4.7(b). Furthermore, recent theoretical work on ionization with two-cycle pulses [Arb06] have also predicted similar 2-D electron momentum distributions. In their work, Arbó *et al.* [Arb06], compare the electron momentum distributions generated from a full TDSE calculation, with those calculated in the Strong-Field Approximation (SFA, see section. 2.2.2), where the effects of the Coulomb Potential of the parent ion are neglected once the electron is in the continuum. As seen in Fig. 4.8, the absence of radial structures for  $p_{\parallel} < 0$  in the SFA calculations indicate that they are related to Coulomb-focusing effects of the parent ion. On closer inspection, one also finds that the positions of the stripe-like fringes are shifted in the TDSE calculations relative to those in the SFA calculations.

## 4.4 SFA-based model

To provide a more intuitive understanding of these results, we have developed a simple one-dimensional model based on the SFA. In the model, the ionization is confined to the most intense cycle of a sine-like ( $\phi_{CEP} = \pi/2$ ) pulse, and the electron motion is confined to the laser polarization axis only. The interference term arising from the superposition of the two quantum paths leading to the same momentum  $p$  (Fig. 4.3), referenced by their classical birth times  $t_s$  ( $s = 1, 2$ ), can be expressed by the  $p$ -dependent transition amplitude

$$T(p) = \sum_s C_s(p) \exp\left(\frac{i}{2}p^2 t_s\right) \exp(i\Phi_{IR}(t_s)), \quad (4.2)$$

where

$$\Phi_{IR}(t_s) = \frac{1}{2} \int^{t_s} dt' \{2A(t')p + A^2(t')\}, \quad (4.3)$$

with  $E(t) = -\frac{1}{c} \frac{\partial}{\partial t} A(t)$ . Here  $A(t)$  is the vector potential of the laser field and  $C_s$ , the amplitudes for wave packets created at  $t_s$ . In fact the same expression can be arrived from the stationary phase approximation of the SFA model in eq. 2.49. Ignoring the contribution due to Coulomb effects, the final momentum distribution is interpreted as arising from the superposition of these two EWPs, shifted in time, and with additional phases,  $\Phi_{IR}(t_s)$ , accounting for the classical action of a free electron in a strong laser field, as in the Volkov wave equation.

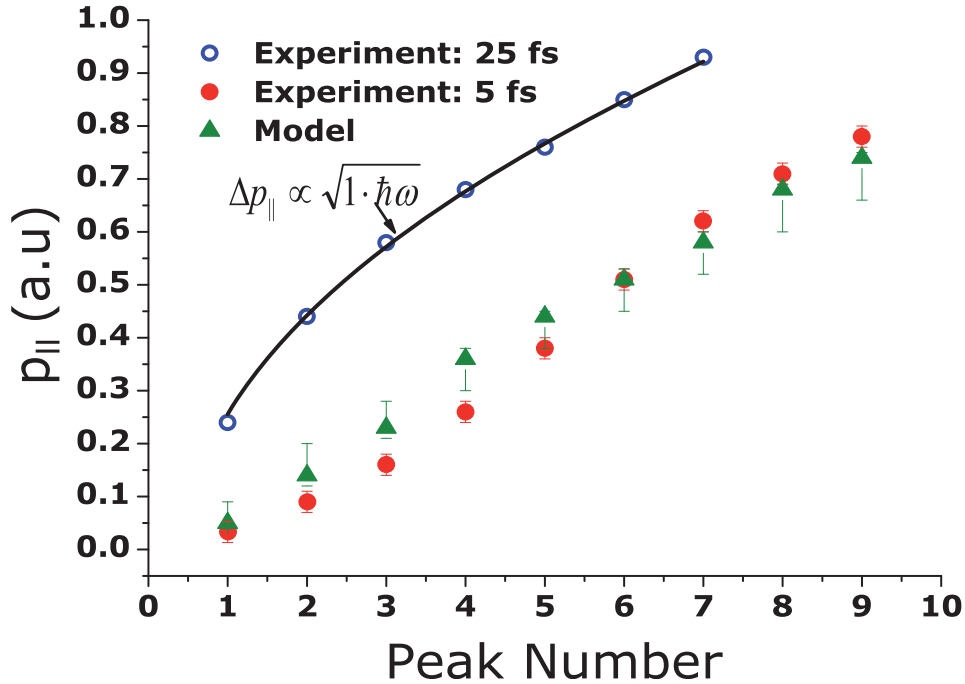


Figure 4.6: Positions of peaks in the parallel momentum  $p_{\parallel}$  for 5 fs, 0.4 PW/cm<sup>2</sup> pulses at a phase of maximum asymmetry as extracted from Fig.4.4 (red full circles). Blue open circles are from previous results for 25 fs, 0.6 PW/cm<sup>2</sup> (shaded area in Fig.4.4(a)) [Rud04]. The black curve simulates a square root ATI-like behavior. Green triangles: SFA model calculation (see text).

For example, in the SVEA, we may consider the electric field of the laser pulse to be of the form  $E = E_0 \cos(\omega t + \pi/2) = E_0 \sin(\omega t)$ , where  $E_0$  is considered to be a slowly varying function of  $t$ , and, hence, assumed to be a constant. Neglecting the action of the Coulomb field of the parent ion, the measured drift momentum  $p$  of the electron is related to its time of birth ( $t_0$ ) through the Newtons equation as:

$$p + A(t_0)/c = 0, \quad A(t_0) = \frac{c}{\omega} E_0 \cos(\omega t_0) \quad (4.4)$$

Within a single cycle, i.e in the interval  $[-\pi/\omega, \pi/\omega]$ ,  $t_0$  has the following solutions

$$\frac{1}{\omega} \cos^{-1} \left( \frac{\omega E_0}{p} \right) \quad \text{and} \quad \frac{2\pi}{\omega} - \frac{1}{\omega} \cos^{-1} \left( \frac{\omega E_0}{p} \right) \quad (4.5)$$

Designating the two solutions as  $t_1$  and  $t_2$ , these are indeed the two possible tunneling phases which lead to the same momentum  $p$ . What remains is to evaluate the expression eq. 4.2 for each set of  $p, t_1, t_2$  and obtain the probability amplitude through  $P(p) = T(p) \cdot T^*(p)$ , where  $T^*(p)$  is the complex conjugate of  $T(p)$ . In this specific case, the expression can be

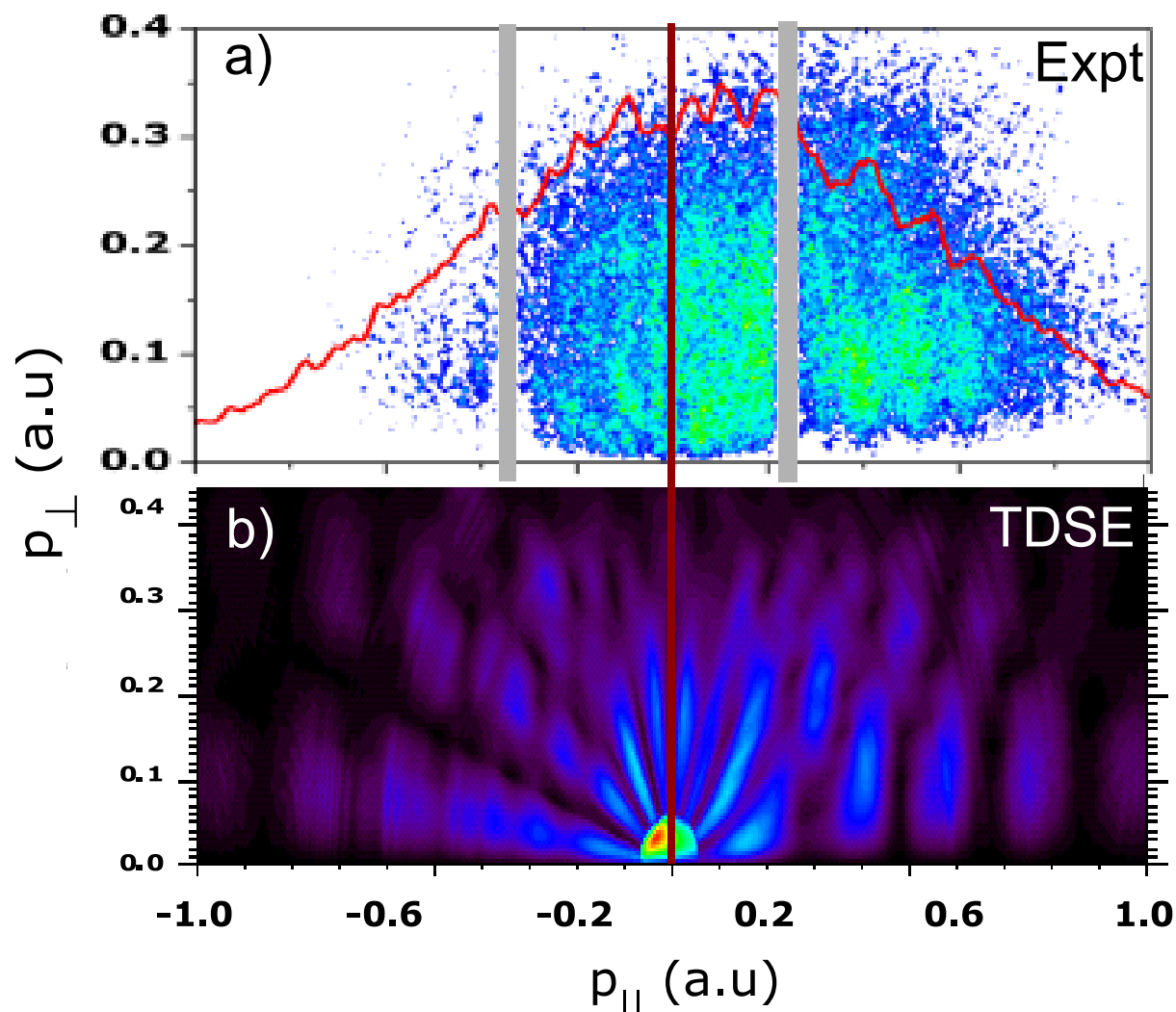


Figure 4.7: (a) 2D electron momentum distribution (linear scale) for a CEP with maximum asymmetry. The x-axis is the longitudinal momentum, the y-axis is the momentum transverse to the polarization direction. The (thick) brown line indicates the position of  $p_{||} = 0$ . The projection onto the  $p_{||}$ -axis is indicated as a red curve. Events below the grey bar have been cut out since here the electron TOF is equal to an integer multiple of the cyclotron frequency of the electrons in the magnetic field of the Reaction Microscope and, accordingly, the transverse resolution diverges (see Sec. 3.6.1) (b) TDSE calculations for ionization of He, with a Gaussian pulse,  $I_0 = 0.3 \text{ PW/cm}^2$ , at 740 nm and FWHM  $\sim 2.7$  fs.

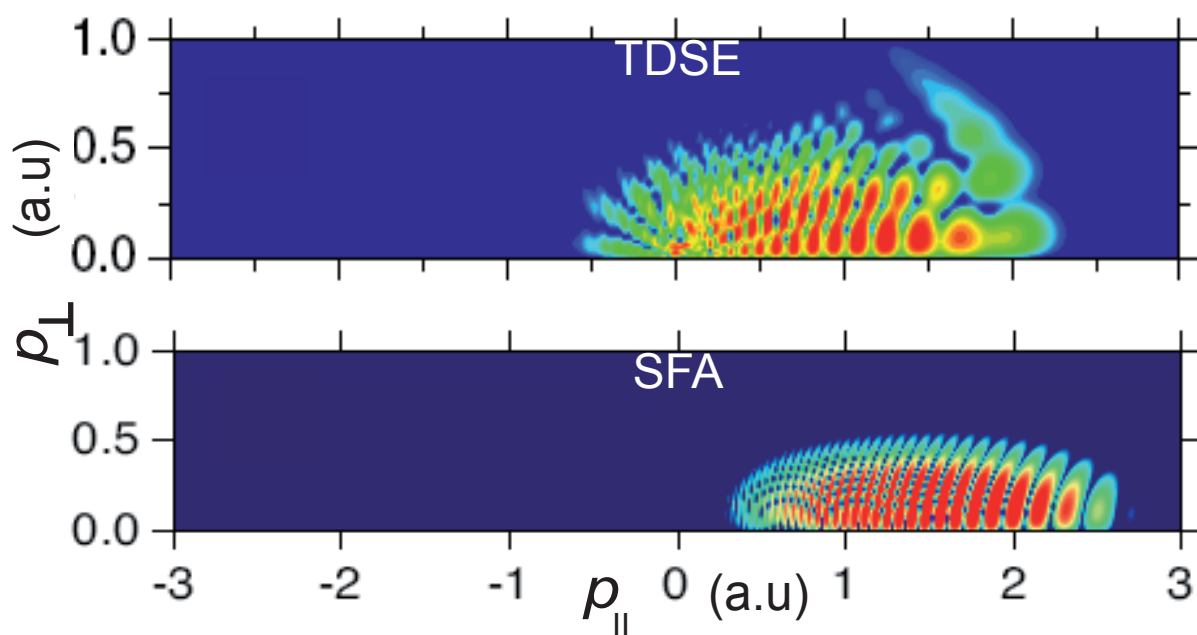


Figure 4.8: TDSE and SFA calculations for two-cycle pulses taken from [Arb06].

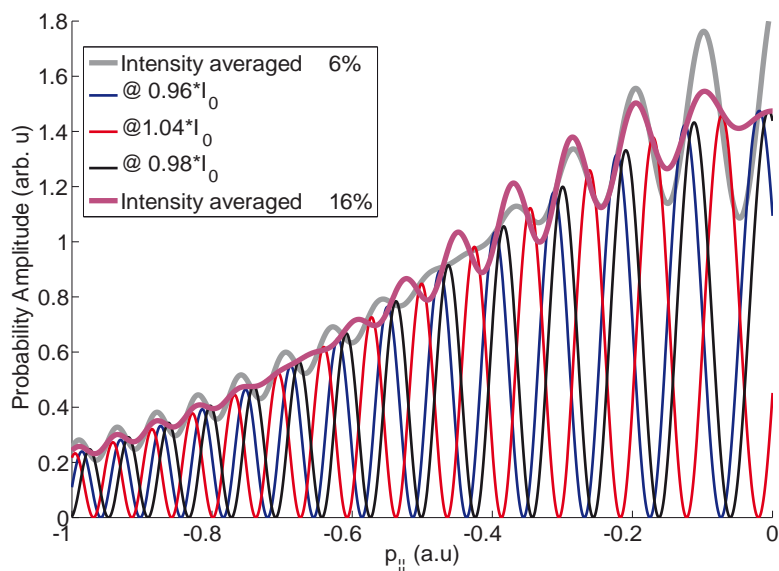


Figure 4.9: The calculations using the one-dimensional model for different peak intensities. Plotted here is also the intensity averaged calculations in grey and purple (see text).

simplified as follows :

$$T(p) = C_1(p) \exp\left(\frac{i}{2}p^2 t_1\right) \exp(i\Phi_{IR}(t_1)) + C_2(p) \exp\left(\frac{i}{2}p^2 t_2\right) \exp(i\Phi_{IR}(t_2)), \quad (4.6)$$

$$P(p) = C_1^2(p) + C_2^2(p) + 2C_1(p)C_2(p) \cos\left[\frac{p^2}{2}\Delta t + \Delta\Phi_{IR}(t_1, t_2)\right], \quad (4.7)$$

$$\text{where, } \Delta t = t_2 - t_1 \text{ and } , \quad (4.8)$$

$$\Delta\Phi_{IR}(t_1, t_2) = \frac{E_0^2}{4\omega^2}(t_2 - t_1) + \frac{E_0^2}{8\omega^3}(\sin(2\omega t_2) - \sin(2\omega t_1)) + \frac{E_0 p}{\omega^2}(\sin(\omega t_2) - \sin(\omega t_1)) \quad (4.9)$$

While the above expressions are obtained for the case of a near-continuous wave laser pulse, the experimental conditions require us to obtain the same for the case where the pulses are sub-5 fs. This was in fact done and expressions similar to the one above were obtained for the case where the envelope function  $E_0$  was approximated by a  $\cos^2$  intensity envelope with FWHM of 5 fs. The probability amplitude was, therefore, numerically evaluated for the following parameters :  $E_0 = 0.105$  a.u, which corresponds to an intensity of  $I_0 = 0.4$  PW/cm<sup>2</sup> and  $\omega = 0.061$  a.u, which corresponds to a central wavelength of 740 nm.

It is evident that any modulation in the momentum distribution strongly depends on the intensity and, hence, any comparison with the experiment would require us to obtain intensity averaged distributions. In fact, it is intriguing that structures from the sub-cycle interferences actually can be observed [Bec02], as the trajectories leading to the interferences sensitively depend on the intensity. In an experiment the measured momentum spectra does not arise from only a single point in space, making it erroneous to associate a well-defined intensity for the measured spectra. We, therefore, speak of an effective focal volume for ionization. This, however, implies that within the focal volume, different spatial points experience different intensities, and the averaged spectra from all the points in the focal volume would possibly wash out the sub-cycle interferences. It is, therefore, imperative to investigate this premise in some detail.

At the very outset, we introduce an argument to limit the focal volume to only the volume with the highest ionization rate. Let us consider a single point in momentum space and the contribution to the amplitude from different spatial positions in the focal volume. For example, at a position in the focal volume, which sees an intensity which is 88% of that at the peak ( $I = 0.88 * I_0$ ), the ionization probability would scale approximately as  $(I/I_0)^{I_p/(\hbar\omega)}$ . Here  $I_p$  is the ionization potential of the target and  $\omega$  the central frequency of the laser pulse. This factor then turns out to be 0.12, i.e., ionization from that point in the focal volume has only a contribution of 12% to the final amplitude in momentum space.

In our model calculations we take a total intensity variation of 12% owing to various factors (laser fluctuations or finite focal volume effects), and sum over without weighting the relative contributions to the final amplitude (i.e averaged over intensities in a range of  $\pm 6\%$  of  $I_0$ ). Even in this extreme case, the structures do survive. As an example we provide here a plot of our model calculations Fig. 4.9. The probability amplitude

(arbitrary units) is plotted against the longitudinal momentum, for individual intensities (in red, blue and black) and two intensity averaged cases:  $\pm 6\%$  in grey, and  $\pm 16\%$  in purple. On closer inspection, we note that, for the two intensity averaged cases, the first four maxima coincide, followed by a phase shift in the peak positions. Finally, for larger  $p_{\parallel}$  values, the peaks are identical in position for both the cases, demonstrating the principle robustness of the interference pattern against intensity fluctuations.

In Fig. 4.6 the respective positions of the interference maxima as seen in the model calculations at a phase of maximum fringe asymmetry, are indicated as green triangles with uncertainty bars. The upper and lower ends of the bars indicate the peak positions for intensities with  $\mp 6\%$  of  $I_0$ , respectively. For a given intensity (e.g. upper and lower bounds of the error bar) the evaluated peaks lie on a monotonous curve with a general behaviour (slope) drastically different from the ATI-like structure, and nearly linear with  $p_{\parallel}$ . With increasing intensity the spacing between the fringes reduces, such that the interference maximum number 3 for the lower intensity overlaps with interference maximum number 4 of the higher intensity, thereby introducing some ambiguity in the counting procedure. This is reflected in the averaged results (green triangles) as a slight discontinuity between peaks number 3 and 4 in shifting from the lower to the upper end of the error bar. Actually, a similar behaviour is observed in the experimental data between peaks number 4 and 5 (see also Fig. 4.4). Taking into account this unavoidable source of uncertainty in the experiment, we find excellent agreement between the experimental data and the results of our simple model, exactly predicting the positions of the maxima within the given intensity fluctuations, distinctly different from any previous measurements where essentially ATI-like structures have been observed.

## 4.5 Discussion and outlook

One might be surprised about the quality of the prediction since recent theoretical investigations (see e.g. [Mil06] and references therein), clearly emphasize the need for corrections to the SFA to more accurately describe electron momentum distributions at low energies. In particular, it has been pointed out that the long range Coulomb potential changes the behavior of the asymmetry parameter such that the maximum asymmetry does not occur at phases  $\phi_{CEP} = \pm\pi$  as predicted by SFA but rather are found to be shifted by  $\approx \pi/3$  in TDSE as well as in semi-classical calculations taking the Coulomb potential into account. This shift being in general very sensitive on the pulse parameters was found to be quite universal for intensities between  $10^{13}$  and  $10^{14}$  W/cm<sup>2</sup>.

However, in the present experiment, we have no access to the absolute CEP of the laser field. One method to resolve this ambiguity in phase would be to fix the phase of maximum asymmetry by TDSE calculations and compare the experiment with the model at this phase. But on inspection, such an analysis did not yield any more information due to the following findings:

- In the TDSE calculations, the phase of maximum asymmetry is at an absolute phase of  $\pi/3$  in line with previous theoretical findings [Mil06].

- By changing the phase in the TDSE calculations, only the visibility of the fringes is reduced, the positions remain the same.
- Similarly, in the model calculations, the fringes fade away, but the positions are maintained. So a change in phase of  $\pi/4$  would not lead to any difference. This can easily be understood since in a model such as ours, where we use only two interfering wave packets, the time delay between the two does not change with the CEP-phase of the pulse.
- Thus, in theory too, we may expect that since the time delay does not change, the phase modulations introduced by the ionic core is also CEP independent. This is borne out in our experimental results too; we find the peaks to be stable as a function of CEP over a range of  $\pm\pi/4$ . Changing the CEP further, the peaks disappear on one side, appearing at the exact same positions on the other side (Fig. 4.5)).

Nevertheless, in the present analysis we have compared the experimental spectra at phases leading to maximum asymmetry to those of the SFA calculations at maximum asymmetry (for the interference fringes), such that we implicitly have accounted for an intensity (and electron momentum) independent effective phase shift of the experimental data due to the Coulomb potential. This might, at least partly, explain the excellent agreement between experiment and model calculations.

These results provide strong evidence that we have realized a true two-slit arrangement in time, where the slits are experimentally determined (different from earlier, pioneering measurements on two-slit interferences in the emitted x-ray energy during collisions [Tse83] and also different from [Lin05] where four slits were open at a time). Analyzing the FWHM, i.e the visibility of one of the most prominent peaks (0.05 a.u for peak number 5 at  $p_{\parallel}=0.38$  a.u) and relating it to the uncertainty of the birth time of the electron, we find an effective slit width  $\Delta t < 20$  attoseconds. A similar analysis within our simple model indicates that the main sources of effective "slit-broadening" are the intensity fluctuations in the pulse. In addition, other, smaller effects fading the fringe-visibility are due to possible electron-momentum dependent phase shifts of the rescattered electron or a result of multiple recollisions since we certainly do not realize an ideal two-cycle laser pulse with zero field outside the two cycles. We have performed TDSE calculations in order to further substantiate our findings essentially reproducing the predictions in [Arb06] and, thus, the salient features in the present data. We do observe, however, that the details of the patterns - as expected from any interference arrangement - do exhibit extreme sensitivity on the pulse shape, its intensity and duration on a level not controllable in this pioneering experiment. Moreover, the exact format of the screened He scattering potential plays a crucial role. Nevertheless, for demonstration we show one example of a TDSE result in Fig. 4.7(b).

With further progress in the control of the laser pulses or by monitoring the electric field through attosecond streaking we might rapidly proceed towards a situation that we can compare the experimental results to theoretical predictions on a level of being reliably sensitive on the scattering potential chosen in the calculation. In addition, the phase shifts

in the spectra from different target atoms or molecules compared to the spectra from a suitable reference atom or molecule could be used to gain information on the atomic or molecular potential. Thus, 3D momentum imaging of the interference of the re-scattered, modulated EWP with an unaffected, directly launched EWP has the potential to obtain unprecedented information on the ultrashort time electron dynamics, on the details of the scattering potential, especially interesting if one considers molecules, as well as on the ultra-short response of the bound part of the many-electron wave-function. In essence, the re-colliding part of the wave packet will, on the time scale of less than 20 attoseconds, certainly not see a static potential, but a dynamic electron cloud moving on the same time scale, such that one might become sensitive on the attosecond correlated motion of the bound electron(s). In the present case this process is particularly intriguing, since we split the two-electron wave function, interfere it with itself and inspect the result in the single ionization channel.

Finally, with regard to the applicability of this technique to reconstruct the dynamics, in the light of the sensitivity of the interferences to laser intensity, one can envision the following technical advances in future experiments:

- Laser sources with intensity fluctuations down to 1%.
- Accurate retrieval of the laser pulse with techniques such as attosecond streaking.
- Thinner atomic jets with a diameter smaller than the focal diameter of the laser beam (which we frequently do in other experiments) to reduce focal volume averaging.
- As with HHG based tomography, comparing spectra from different atomic and molecular species with similar ionization potentials.
- Assuming data with very good statistical significance (taken with future laser systems with stable operation over days) one could Fourier analyze the momentum distributions (even in two dimensions for fixed transverse momenta) and retrieve potentially left-over contributions from different intensities.

With these advances in the foreseeable future, it is conceivable that the problems imposed by intensity sensitivity would be overcome and the technique would emerge as a powerful tool for atomic, molecular and cluster physics. It is clear, however, that in this pioneering experiment, we are still not at that stage.

# Chapter 5

## Photoionization of $D_2$ with ultrashort XUV pulses

Dynamics of outer-shell bound electrons in atoms and molecules, in general, occur on time scales of a few hundred attoseconds (as) to a few femtoseconds<sup>1</sup> (fs) [Kra09]. On the other hand, molecular processes involving nuclear dynamics like vibration and rotation occur on larger, femtosecond time scales [Zew00], which is easy to see, since the mass of the nuclei are at least 3 orders of magnitude greater than that of the electrons. However, for the lightest molecules,  $H_2$  and  $D_2$ , the vibrational dynamics in the respective singly charged species have been shown to proceed on time scales of a few femtoseconds. Indeed, in experiments, ultrashort IR pulses with durations down to  $\sim 6$ -7 fs were required to comprehensively image their dynamics [Erg06]. In these molecules there is a possibility of coupling the electronic and nuclear dynamics as the correlated dynamics of two electrons [Fan83], being mediated by the parent nuclei, can be expected to occur on the same time scales as the nuclear motion [Ced99]. For example, in the autoionization process, two electrons are simultaneously excited to a doubly excited state, which decays on the time scale of a few femtoseconds [Dre02], leading to the autoionization of one of the electrons. In molecules, this holds special interest as the nuclei are no longer stationary during the decay process implying that the electronic and nuclear dynamics are coupled [Kou97]. Therefore, the dissociation dynamics of the superexcited states of  $H_2$  and  $D_2$  has captivated researchers for the last three decades [Kou97].

In the past, synchrotron based XUV sources have been the mainstay of such kind of experiments since high photon energies are needed to access the doubly excited states. However, it is only recently, with the availability of ultrashort (sub-15 fs)<sup>2</sup> coherent XUV pulses through HHG, that time-resolved studies on XUV-induced molecular dynamics, involving doubly excited states, could be performed [Gag07, San08]. Furthermore, the possibility of controlling molecular dissociation which has been shown with CEP stabilized few-cycle IR pulses [Kli06, Kre09a] might be extended with ultrashort HHG pulses, through

---

<sup>1</sup>if Rydberg wave packets, or highly excited states are involved

<sup>2</sup>In this chapter we shall refer to the envelope of the attosecond pulse train and not to the individual pulses under the envelope.

the control of the electronic-nuclear coupling on the femtoseconds timescales.

The experimental realization of using ultrashort XUV pulses to study the time dependent photodissociation process in molecules, however, poses an interesting technical challenge. As elucidated in Chaps. 2 and 3, the production of ultrashort XUV pulses in itself is a result of demanding development of state-of-the-art techniques in laser physics. On the other hand studying the coupled electron-nuclear dynamics mandates the use of state-of-the-art coincident multi-particle imaging spectrometers such as the Reaction Microscope. In this Chapter, the combination of these two technologies, specifically, to study molecular dissociation in  $D_2$ , is presented. These first results show that the symmetry of the dissociation in  $D_2^+$  is broken through the interference of multiple ionization channels, involving autoionizing states, in qualitative agreement with theory [Fer09] and earlier experiments with synchrotron sources [Mar07]. The novelty of this demonstrative experiment is the promise of control over the duration of the XUV pulses in future experiments, to eventually study the temporal evolution of the autoionization, as envisaged in recent theoretical studies [Per09, Mor09].

## 5.1 Overview

In order to elucidate the various processes which accompany the interaction of  $D_2$  with an energetic photon, we now consider the potential energy curves in Fig. 5.1. The consequence of electronic transitions occurring much faster than any nuclear motion is the *Franck-Condon principle*, which, stated simply, says that in the potential energy diagram, electronic transitions occur along a vertical line as demarcated by broken vertical lines in Fig. 5.1, implying that the internuclear distance does not change during the transition. Considering that we start from the ground state of deuterium, for a given photon energy, we look into the overlap of the Franck-Condon region with the potential curves to ascertain which states are populated.

The threshold for photoionization of  $D_2$  is evident from the figure to be 15.8 eV. For photon energies just above the threshold, only the  $1s\sigma_g$  states are populated. Since the minimum of the  $1s\sigma_g$  curve for  $D_2^+$  is slightly displaced with respect to the ground state curve of  $D_2$ , the vertical transition populates not just the vibrational ground state, but also higher vibrational levels of the  $1s\sigma_g$  curve (Fig. 5.2(a)). The *Franck-Condon factors* which give the distribution of the population among the vibrational modes, however, do predict that a small fraction of the ground state population reach the dissociative continuum of the  $1s\sigma_g$  curve. As the photon energy is increased, at a certain threshold value of 18.1 eV ( $D_1$ ), the fraction becomes significant, such that dissociation of  $D_2^+$  into a neutral and a proton through the  $1s\sigma_g$  curve can be observed to accompany the photoionization process (Fig. 5.2(a)).

For photon energies above the Dissociative Photoionization (DPI) threshold, the ratio of the  $D^+$  ions to the  $D_2^+$  ions created flattens out, such that for  $E_{XUV}$  of up to 30 eV,  $\sim 2\%$  of the  $D_2^+$  ( $H_2^+$ ) ions in the ground state eventually dissociate to give low kinetic energy fragments [Bro73, Chu93]. For  $E_{XUV} \geq 29$  eV, the  $2p\sigma_u$  state is now

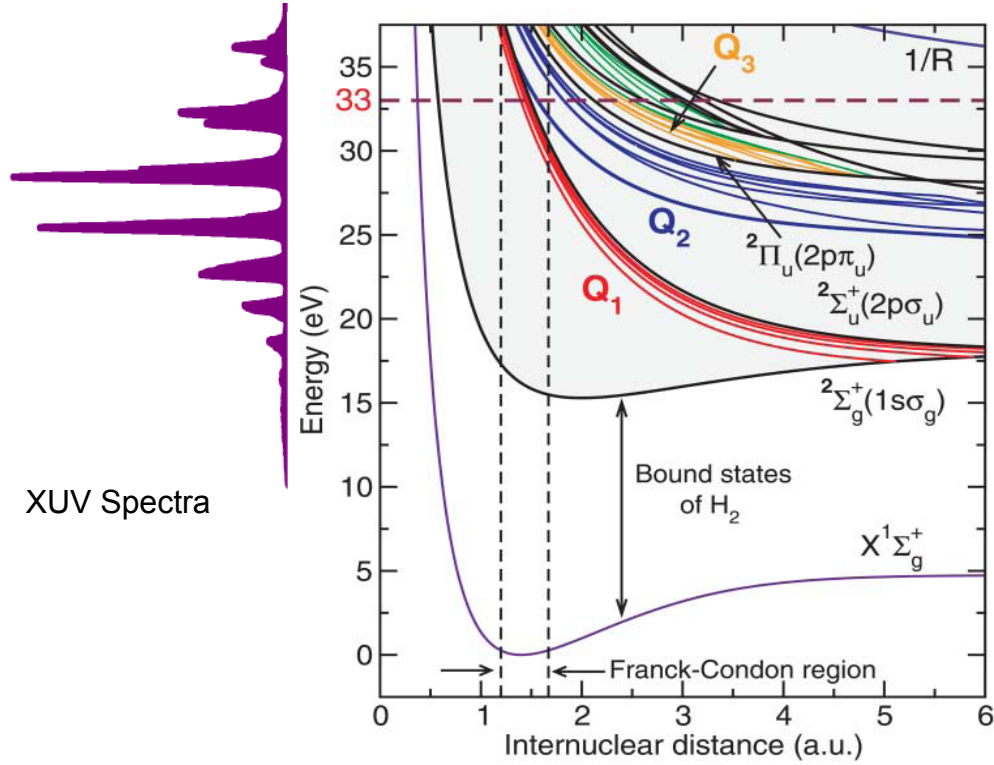


Figure 5.1: The potential curves for  $H_2^+$  with respect to the ground state of  $H_2$ . The broken vertical lines indicate the Franck-Condon region. The curves for  $D_2$  are qualitatively the same, except for slight shifts in the energy scale. However, for the purpose of illustration, the above curves will suffice. On the left panel the high harmonics spectra is illustrated so as to ascertain the possible states that can be populated by the XUV radiation (figure adapted from [Mar07]).

accessible. This being a repulsive curve, the  $D_2^+$  created directly dissociates to give energetic fragments [Ito96, Chu93], with the excess energy over the dissociative threshold  $E_{XUV} - D_1$  distributed between the Kinetic Energy Released during the fragmentation,  $KER$ , and the photoelectron energy  $E_e$  (Fig. 5.2(b)).

The above direct pathways can therefore be expressed compactly as



However, as seen in Fig. 5.1, in addition to the well-known curves of  $1s\sigma_g$  and  $2p\sigma_u$ , we note the existence of the infinite series of doubly excited states  $Q_1$  (red) and  $Q_2$  (blue) which are accessible in the photon energy range of 25-35 eV. In particular,

- In parallel transitions, the lowest  $Q_1$  state, with  $\Sigma_u$  symmetry is accessible for photon energies greater than  $\sim 25$  eV (23 eV for  $H_2$ ) [He95]. A fraction of the population

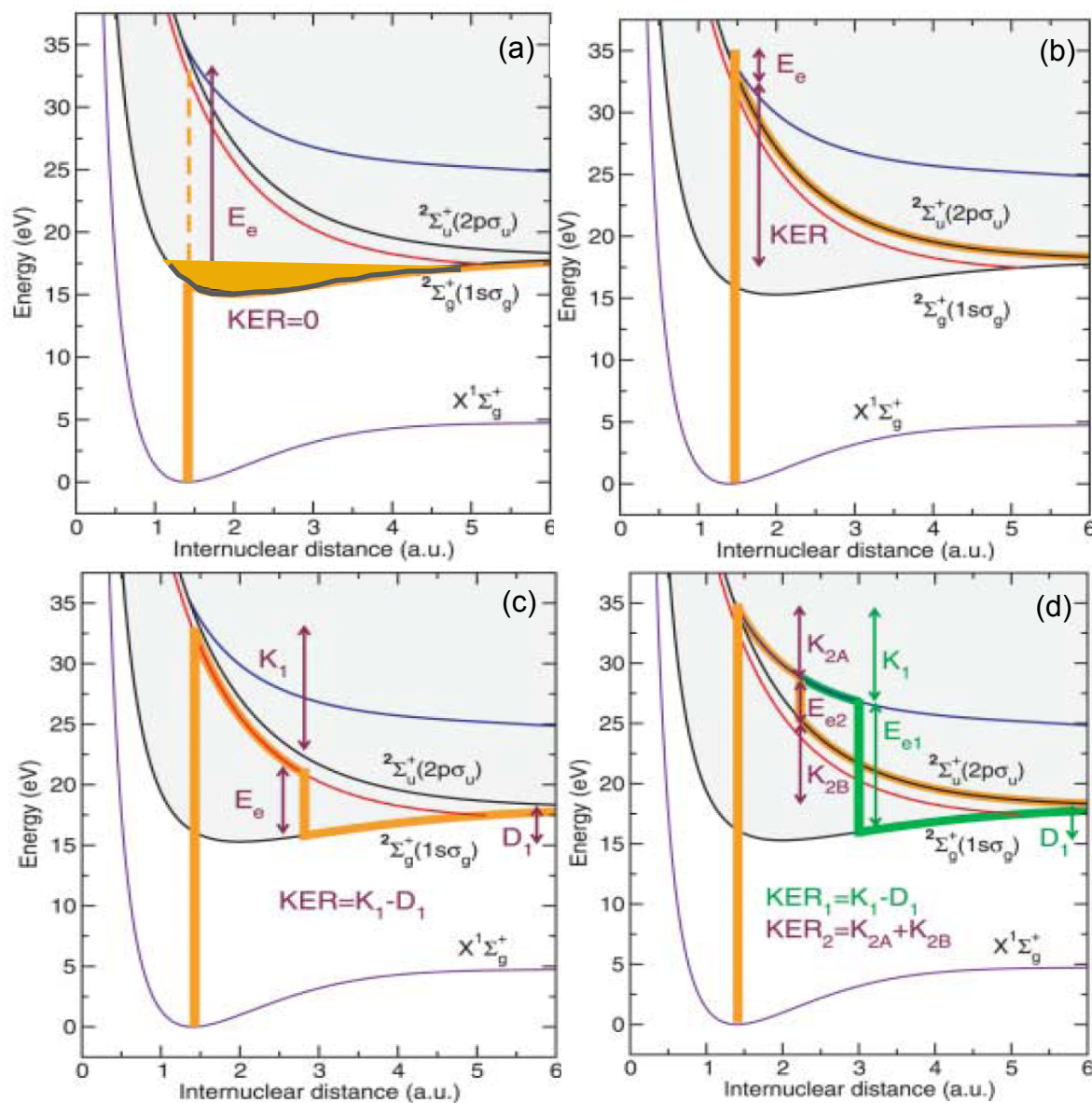
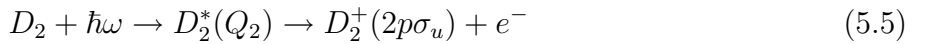
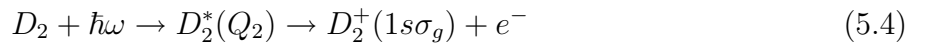
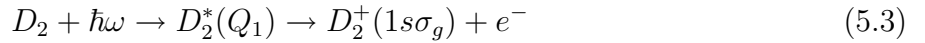


Figure 5.2: The possible semi-classical pathways for DPI are illustrated as follows: (a) Direct ionization to the  $1s\sigma_g$  curve populates the higher vibrational, dissociative states of  $1s\sigma_g$  resulting in ground-state dissociation with low kinetic energy release  $KER = 2 \cdot KE \sim 0$  eV, where  $KE$  is the kinetic energy of the  $D^+$  ion; (b) direct ionization to the  $2p\sigma_u$  repulsive state leading to high energy fragments; (c) the lowest doubly excited  $Q_1$  state is resonantly populated in a parallel transition, and can autoionize to the  $1s\sigma_g$  curve, leading to high energy ions with  $KER = K_1 - D_1$ ; (d) the lowest  $Q_2$  state can autoionize to both the  $1s\sigma_g$  and  $2p\sigma_u$  curves (figure adapted from [Mar07]).

on this repulsive state can then dissociate into two neutral atoms or, alternatively, autoionize, with the molecular ion relaxing to the dissociative continuum of the  $1s\sigma_g$  curve (see [San06] for more details about the autoionizing states of  $D_2$ ). In autoionization the photon energy,  $E_{XUV}$ , is distributed between the energy of the autoionized electron,  $E_e$  and the internal energy of the molecular ion,  $K_1$  at the time of autoionization (Fig. 5.2(c)). Finally the excess of the internal energy over the dissociation energy  $D_1$  appears as release of high kinetic energy in the fragments,  $KER = 2 \cdot KE = K_1 - D_1$ . In experiments, this resonant path was identified leading to a peak at around 3 eV [Str79, Ito96] for photon energies of  $\sim 27$  eV.

- In perpendicular transitions, for photon energies greater than  $\sim 32$  eV, the lowest  $Q_2$  ( $\Pi_u$ ) curve is resonantly populated [He95]. This state can now autoionize to either the  $2p\sigma_u$  curve or the  $1s\sigma_g$  curves as shown in Fig. 5.2(d). Again, in high resolution ion spectra acquired perpendicular to the polarization direction a number of peaks in the  $KE$  region of 2-8 eV [Ito96] were explained as (i) autoionization by the  $Q_2$  states at higher internuclear distances to  $1s\sigma_g$  curve (green curve in Fig. 5.2(e) leading to a peak between 3-5 eV ( $K_1 - D_1$ ) and (ii) autoionization to the  $2p\sigma_u$  curve (orange curve in Fig. 5.2(d) at lower internuclear distances, contributing to the spectrum around 7-8 eV ( $K_{2A} + K_{2B}$ ).

The above three resonant pathways are summarized as



While early theoretical treatment [Kir81, Kan83] could reproduce the shape of the  $KE$  spectra and positions of the peaks, a significant disagreement with theory [San97, Ten96] was seen with regard to the estimation of autoionizing widths using  $KE$  spectra [Lat93]. However, it was shown by Sanchez and Martin [San98, San99a, San99b] that the semi-classical ionization channels depicted above cannot directly be assigned to the observed peaks in the high  $KE$  ion spectra, and that interferences between the direct and resonant channels had to be incorporated to correctly explain the features. Essentially, since in the  $KE$  region of 3-7 eV, contributions from both  $1s\sigma_g$  and the  $2p\sigma_u$  states are present, the two dissociation pathways can be expected to interfere. Furthermore, since the two states are of different symmetry, the interference would manifest as an asymmetry in the photoelectron distribution in the molecular frame, thus laying emphasis on obtaining coincident electron distributions in experiments to completely characterize DPI.

Coming to the electron distributions, we first note that in contrast to atoms, the non-spherically symmetric molecular Coulomb field allows the outgoing electron wave to have partial wave contributions of  $l > 1$ . In other words, the photoelectron angular distribution in the molecular frame is a superposition of many  $l$  states. However, molecular frame electron distributions in experiments by Hikosaka *et.al.* [Hik02, Hik03] and Ito *et.al.* [Ito96] analyzed in the framework of Ref. [Dil76], showed, that for parallel transitions where the

molecular ion is finally in either the  $1s\sigma_g$  or the  $2p\sigma_u$  state, the outgoing electron wave has a predominant  $p\sigma$  character. For perpendicular transitions on the other hand, a dominant  $d\pi$  electron wave is seen. Finally, only in recent experiments [Laf03, Mar07], asymmetries in the electron distributions were observed providing experimental support to the interference picture.

While, the experimental work till date detailed above were using radiation from synchrotron sources where little or no time resolution is afforded, recent theoretical work [Per09, Mor09], indicate the possibility of studying time resolved dynamics using ultrashort XUV sources. In particular it has been shown that the interference between the channels could be studied as a function of the duration of the XUV pulse, and thereby experimentally infer the autoionization decay time of the doubly excited state,  $Q_1$  [Per09]. In this respect, the work presented here assumes significance as we report on the first 3D ion and electron momentum spectra from DPI in  $D_2$  acquired in a Reaction Microscope using ultrashort XUV sources.

## 5.2 Experimental details

In the experiment, linearly-polarized XUV pulses with a pulse width of  $\sim 15$  fs (envelope of the APT), at a central frequency of  $\sim 30$  eV and a repetition rate of 8 kHz were obtained from the HHG beamline at MPI-K. The experimental setup for production of ultrashort XUV pulses has been covered in detail in Chap. 3. The XUV pulses were loosely focused into the supersonic, cold  $D_2$  jet ( $\sim 10^{11}$  atoms/cm<sup>2</sup>) in the ultra-high vacuum chamber ( $\sim 2 \cdot 10^{-10}$  mbar) of the Reaction Microscope. The created ions and electrons were guided to two position sensitive channel plate detectors by electric ( $\sim 30$  V/cm) and magnetic ( $\sim 1.56$  mT) fields, applied along the spectrometer axis. The laser polarization was aligned along the spectrometer axis. The high harmonics spectrum was obtained from the XUV spectrometer (see Chap. 3 for details) and observed to have a lower edge cut off at  $\sim 20$  eV from an Al filter<sup>3</sup> and an upper energy cut off at  $\sim 38$  eV (Fig. 5.3). The same was confirmed by analyzing the photoelectron energy spectrum from the ionization of Ar in the Reaction Microscope. The two dimensional position and time-of-flight spectra for the ions and electrons were recorded in coincidence for a stable acquisition period of  $\approx 48$  hours with recoil-ion count rates of  $\approx 300$  Hz, and 3D momentum distributions were obtained with a resolution of  $\sim 1$  a.u. for the ion momenta and a resolution  $\sim 0.1$  a.u. for the electron momenta.

## 5.3 Results

The recoil-ion time-of-flight (TOF) spectrum presented in Fig. 5.4(a) shows that in the energy range of the photons, the most probable process is the photoionization of  $D_2$  to a bound state of  $D_2^+$ , evidenced by the prominent peak (TOF  $\sim 2240$  ns) of  $D_2^+$  on the

<sup>3</sup>to suppress the rest IR used in generating the harmonics and the lower harmonics

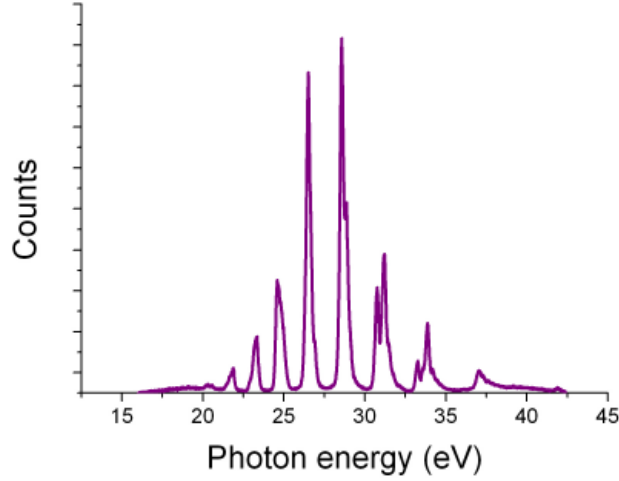


Figure 5.3: The high harmonics spectrum as seen in the XUV spectrometer [Rie06].

far right of the spectrum. The Franck-Condon principle requires that a certain fraction of the ground state wave function of  $D_2$  is projected onto the higher vibrational, dissociative states of the ground state of  $D_2^+$ . This manifests as a sharp peak at TOF  $\sim 1590$  ns, which corresponds to the TOF of  $D^+$  with near zero kinetic energy ( $KE$ ), as expected from ground-state dissociation. Distributed symmetrically about the peak are the shoulder-like structures from  $D^+$  ions with higher kinetic energy. The ions with a lower TOF relative to the peak at  $\sim 1590$  ns are those which are emitted initially towards the recoil-ion detector. The ions which arrive later are emitted initially away from the detector, but were turned around by the electric field, to finally be detected at higher TOF. We now proceed to calculate the  $KE$  of the detected ions of interest (in the shaded region in Fig. 5.4(a)) and plot in Fig. 5.4(b) the  $KE$  distribution of all the detected ions in this regime.

### 5.3.1 Kinetic energy spectrum for $D^+$

The dominant peak at zero  $KE$  we have previously assigned to the dissociative continuum of the  $1\sigma_g$  curve, coming from the direct ionization channel in eq. 5.2. The next possible state which can directly be accessed in the Franck-Condon region (Fig. 5.2) lies on the repulsive  $2p\sigma_u$  curve. From the potential energy curves it is quite easy to see that ionization to this state would lead to the release of an electron with low energy, while the excess energy of the photon over the dissociative limit would manifest itself as a high kinetic energy  $D^+$  fragment. Indeed the peak like structures at around  $\approx 7$ eV may therefore contain contributions due to dissociation along the  $2p\sigma_u$  curve [Deh78, Hik02, Ito96] following a direct ionization as in eq. 5.2.

The  $KE$  distribution of ions between 2 eV and 7 eV is of interest to the work pre-

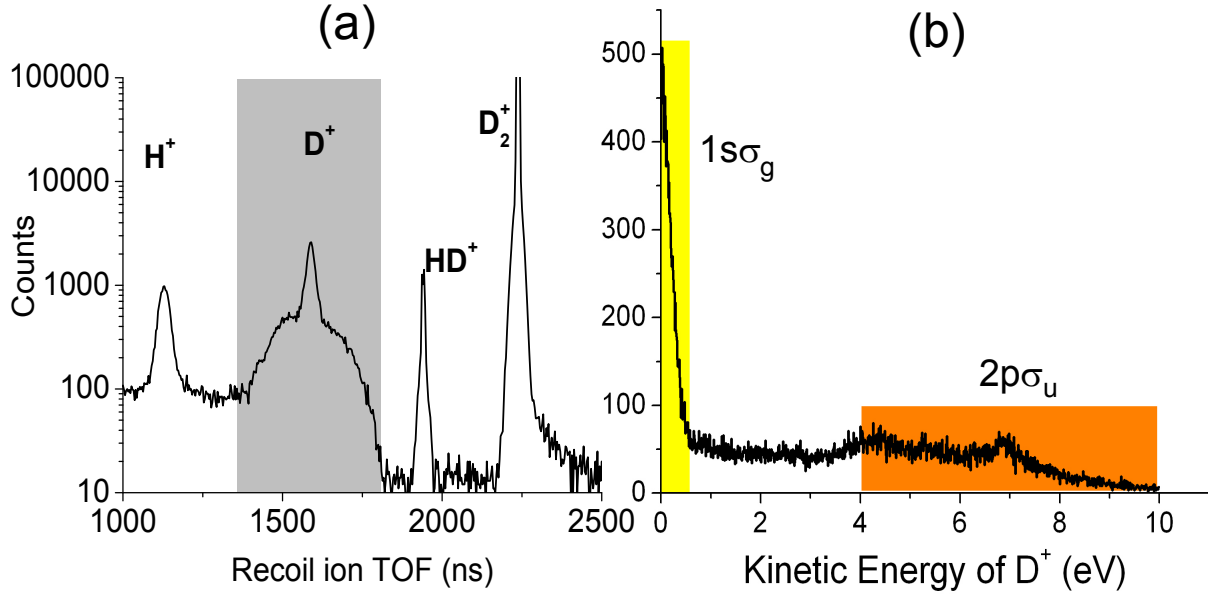


Figure 5.4: (a) The recoil-ion time-of-flight, showing the identification of various ionic species, wherein the shaded area picks out the ions of interest. (b) The Kinetic Energy spectrum for the  $D^+$  ions. The lower  $KE$  (shaded yellow) ions are mainly from ground-state dissociation along the  $1s\sigma_g$  curve. The higher  $KE$  ions (shaded orange) are predominantly through dissociation along the  $2p\sigma_u$  curve.

sented here, as they present the signature of the involvement of autoionizing states in the photoionization process. In earlier experiments with photon energies greater than 36 eV (for e.g. [Gar75]), the presence of a band centered around  $\sim 5.5$  eV was attributed to dissociation contributions from the  $2p\pi_u$  and  $2s\sigma_g$  repulsive states. In contrast, for the experimental conditions here, with a rapid XUV cut off at around 38 eV, we can in the first approximation ignore the contributions from these states. Rather, as discussed in [Ito96, Laf03] experimental evidence and theoretical work attribute the detection of ions with  $2.5 \text{ eV} \leq KE \leq 5 \text{ eV}$  and  $5 \text{ eV} \leq KE \leq 7.2 \text{ eV}$  to autoionization from the  $Q_2$  states preferentially to the  $2p\sigma_u$  curve at specific, short internuclear distances, leading to high  $KE$  fragments, and to the  $1s\sigma_g$  curve at a fixed, larger internuclear distance, leading to somewhat lower  $KE$ . Furthermore, autoionization [Ito96, Laf03] from the  $Q_1$  states to the  $1s\sigma_g$  continuum would also contribute to a  $KE$  peak around 7 eV, with a long asymmetric tail towards the lower  $KE$  side.

Since the  $KE$  spectrum has a mix of contributions from different ionization channels, many of them involving autoionizing states, it is clear that the  $KE$  spectrum alone cannot yield any more information. However, one realizes that since the symmetry of the two autoionizing states are different, we may utilize this information to disentangle the two channels. In particular, the lowest  $Q_1$  state has a  $\Sigma_u$  symmetry, and can therefore be

populated from the ground state  $\Sigma_g$ , only through a parallel transition. Thus, in the experiment, the contribution from the  $Q_1$  state can exclusively be observed if only dissociation products parallel to the polarization axis of the XUV radiation are considered. Similarly, the contribution due the lowest  $Q_2$  state, with  $\Pi_u$  symmetry can be observed by collecting the dissociation products perpendicular to the polarization axis.

Before we proceed we should however note a further complication in the spectra peculiar to the ultrashort nature of the XUV pulses used in the present experiment. The large spectral range of the pulses used here result in the observed  $KE$  spectrum to be a convolution of the independent  $KE$  spectra from the harmonics that were used to synthesize the ultrashort pulses. Fortunately, energy conservation comes to our rescue, as the energy of the photon in excess of the dissociation energy ( $D_1= 18.1$  eV), is distributed continuously between the energy of the electron ( $E_e$ ) and the fragmentation energy  $KER$  during the dissociation. Since, for the experimental conditions considered here, the dissociation products are found in their ground states <sup>4</sup>, the fragmentation energy is transformed directly to the  $KE$  of the ion and the neutral: i.e,  $KER = 2 \cdot KE$ . So, energy conservation can be expressed as  $E_{XUV} - D_1 - (E_e + 2 \cdot KE) = 0$ , where  $E_{XUV}$  is the energy of the photon. Clearly, a plot of  $E_e$  as a function of the  $KE$  would have distributions peaked around a series of parallel lines with slope of -2. Furthermore the intercepts on the  $E_e$  axis would be separated by the energy difference between the harmonics ( $2\omega$ , where  $\omega$  is the central frequency of the fundamental IR pulse used to generate HHG, see Chap. 2 for details).

### 5.3.2 Energy correlation plots

Plotted in Fig. 5.5 therefore is the so-called experimental energy correlation plot  $E_e$  vs  $KE$  generated by selecting the perpendicular and parallel transitions respectively. To be noted is that in the experiment the molecular axis is randomly oriented with respect to the fixed polarization axis. In selecting the parallel transitions, we select in our analysis, only those ions detected in a cone about the polarization axis subtending a maximum angle of 15 degrees to the polarization ( $p_z$ ) axes. In other words,  $p_r \leq 0.5 |p_z|$ , where  $p_r$  is the transverse radial component and  $p_z$  is the longitudinal component (see Chap. 3) of the deuteron momentum  $\vec{p}_{D^+}$  in the laboratory frame. We now invoke the *axial-recoil approximation*, which states that the direction of the momentum vector of the recoil ion,  $\vec{p}_{D^+}$ , essentially defines the alignment of the molecule during DPI. To elaborate, in the first step of the DPI process, the momentum of the ionized electron  $\vec{p}_e$  is balanced by the recoil momentum of the molecular ion  $\vec{p}_{D_2^+}$ . Hence, after fragmentation, the ion momentum  $\vec{p}_{D^+}$  must be corrected by  $\vec{p}_e$  to obtain the initial molecular alignment. However, a quick calculation shows that for the high  $KE$  ions, this correction is small enough to be ignored in the first approximation. Likewise, since the dissociation proceeds in fs time scales, the slow (ps) rotation of the molecule during the dissociation can be neglected. Thus, selecting ions detected along the polarization axis ensures that we have selected fragmentation events where the molecular axis was accidentally aligned along the polarization axis at the instant

<sup>4</sup>The  $2p\pi_u$  and  $2s\sigma_g$  repulsive curves leave the neutral  $D$  in the first excited state ( $n = 2$ )

of the photo absorption. To select the perpendicular transitions, however, the condition was  $|p_z| \leq 0.17p_r$ , i.e, ions detected in a cone subtending 7.5 degrees to the transverse axes.

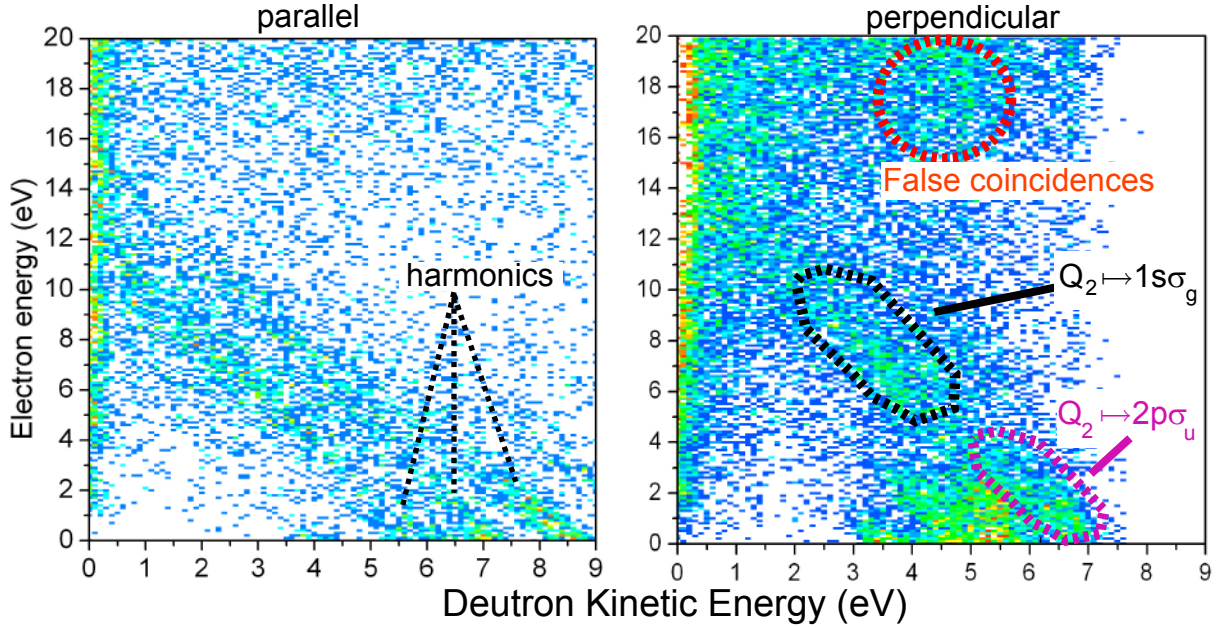


Figure 5.5: The energy correlation plots, for parallel (left) and perpendicular (right) transitions. On the horizontal axis is the kinetic energy of the deuteron, on the vertical axis, the electron energy. The 'finger-like' structures with a slope of -2 are signatures of ionization from the successive harmonics. For perpendicular transitions (right), the two islands, demarcated by black and purple broken curves, can be assigned to autoionization from the  $Q_2$  states leading to population of the dissociating states of  $1s\sigma_g$  and  $2p\sigma_u$  respectively (see text).

The harmonics are clearly identified in the energy correlation plot of Fig. 5.5 as a series of parallel distributions with slope -2 and intercepts on the  $KE$  axis which are separated by  $\sim 1.6$  eV. This implies that the photon energies can easily be obtained through the intercepts they make at the axes. Furthermore, this plot serves as an independent check of the calibration of the ion and electron spectrometers. Additionally, since the real events are only distributed around these imaginary lines with slope -2, we can filter out the false coincidences which occur from rest gas ionization, thereby improving the signal-to-noise ratio of these spectra. Finally, as in [Laf03] the various ionization channels can be identified as follows. The intense distribution close  $KE \approx 0$  eV in Fig. 5.5(a) and (b) is from the direct ionization to  $1s\sigma_g$ . The direct ionization channel  $2p\sigma_u$  appears around  $E_e \approx 0$  eV for  $\sim 4 < KE < 9$  eV. Fig. 5.5(a) the resonant channel  $Q_1 \rightarrow 1s\sigma_g$  appears along the diagonal. On the other hand the resonant channels  $Q_2 \rightarrow 1s\sigma_g$  and  $Q_2 \rightarrow 2p\sigma_u$  appear as islands in 5.5(a) demarcated by black and pink areas respectively.

### 5.3.3 Molecular Frame Photoelectron Angular Distributions (MF-PAD)

The full capability of the Reaction Microscope is exploited in the measurement of the angular distribution of the electrons. The procedure for obtaining the 3D momentum components for the electrons has been discussed in detail in § 3.6.1, where however, the momentum components are obtained in the laboratory frame. If the molecules in the gas target are randomly aligned, then the photoelectrons from ionization by a linearly polarized light source, can be shown to have an angular distribution [Dil76]

$$\frac{d\sigma}{d\Omega} = \frac{\sigma_{tot}}{4\pi} [1 + \beta \cdot P_2(\cos \theta)] \quad (5.6)$$

$$P_2(\cos \theta) = \frac{1}{2}(3 \cos^2 \theta - 1) \quad (5.7)$$

Here  $P_2$  is the Legendre Polynomial of second order, and  $\theta$  is the angle between the direction of the emitted electron and the polarization axis.  $\beta$ , defined as the anisotropy parameter of the photoelectron angular distribution (PAD), lies in the interval  $[-1,2]$ . The equivalence of this distribution with those seen in atoms (see Chap. 2) leads to the conclusion that the random orientation of the molecules with respect to the polarization axis smears out any details of the molecular origin of these electrons.

In contrast, if the molecule has some definite alignment with respect to the polarization axis, then the PAD has the form [Dil76]

$$\frac{d\sigma}{d\Omega} = \sum_{k=0}^{2l_{max}} A_k P_k(\theta) \quad (5.8)$$

where  $\theta$  is measured with respect to the molecular axis.  $l_{max}$  is the largest angular momentum component of the outgoing electron wave,  $A_k$  are the expansion coefficients of the Legendre polynomials  $P_k$ . While in principle there is no limit to the value of the angular momentum  $l$ , in practice, however partial-wave expansion converges at relatively small  $l$ .

Traditionally, *a priori* alignment of a molecule has been demonstrated where a long moderately-intense laser pulse ( $\leq 10^{12}\text{W}/\text{cm}^2$ , 3 ns), with durations longer than the rotational period of the molecule, can adiabatically align the molecule along the polarization axis of the aligning field [Sta03]. Alternatively, an intense short pulse ( $\geq 10^{13}\text{W}/\text{cm}^2$ , 0.5-5 ps) can be used to 'kick' the molecule into a coherent superposition of many rotational modes, which periodically come into phase, thereby getting aligned [Sta03]. These aligned molecules, can now be probed with the XUV pulses [Lep07]. While these methods for *a priori* alignment present a very useful tool, here, however we employed the vector correlation method [Laf01, Laf03] to obtain the PAD in the molecular frame.

In this method, using the axial-recoil approximation, the momentum vector of the deuteron  $\vec{p}_{D^+}$  defines the molecular axis. Along with the fixed polarization axis  $\hat{\epsilon}$ , the vector pairs  $(\vec{p}_{D^+}, \hat{\epsilon})$  define a frame of reference that is fixed with respect to the molecule.

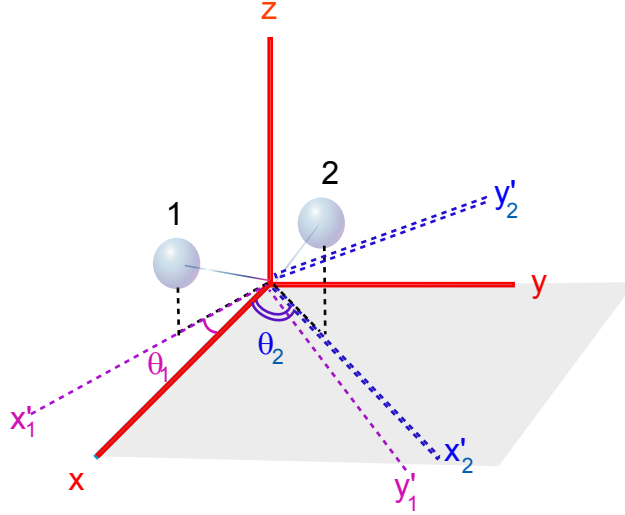


Figure 5.6: The transformation of the coordinates from the laboratory frame into the molecular-polarization axis frame. For an event **1**, the molecular axes is randomly oriented with respect to the laboratory frame (red axes,  $x, y, z$ ) While keeping the  $z$  coordinate the same, the frame of reference is rotated about the  $z$  axis by  $\theta_1$  to the current frame,  $x'_1 y'_1 z$ . For the next event, **2**, a new transformation with  $\theta_2$  is effected to all the coordinates of both, the ions and the electrons, so as to be consistently expressing all quantities in a frame, here rather a plane, containing the polarization axis and the molecular axis.

Specifically, we first obtain for every event<sup>5</sup>, the components of  $\vec{p}_{D^+} = (p_x^{rec}, p_y^{rec}, p_z^{rec})$  in the laboratory frame, in much the same way as described in § 3.6, where  $x, y$  are in the plane transverse to the spectrometer axis, and  $z$  is along the spectrometer axis. Now, since the laser polarization is along the spectrometer axis, in the transformation from the lab-frame to the instantaneous molecular frame,  $p_z^{rec}$  remains unchanged<sup>6</sup>. The transformation (see Fig. 5.6)

$$(p_x^{rec}, p_y^{rec}, p_z^{rec}) \Rightarrow (p_{x'}^{rec}, 0, p_z^{rec}) \quad (5.9)$$

therefore carries us event-by-event from the lab-frame to a frame of reference, where  $\vec{p}_{D^+}$  and  $\hat{e}$  lie on the  $x'z$  plane, in other words the molecule-fixed frame. Finally the Molecular Frame Electron Momentum Distributions (MFEMDs) are obtained by effecting the same event-by-event transformation for the electron positions in the lab-frame ( $x^e, y^e, z^e$ ), and then calculating the momentum components of the electron in this frame.

$$(x^e, y^e, z^e) \Rightarrow (x'^e, y'^e, z^e) \quad (5.10)$$

<sup>5</sup>the detection of the pair ( $D^+, e^-$ )

<sup>6</sup>Since the polarization axis  $z$  is also one of the defining axes of the molecular frame.

### 5.3.4 Molecular Frame Electron Momentum Distributions (MFEMDs) for perpendicular transitions, $E_{XUV} = 32(\pm 1)$ eV

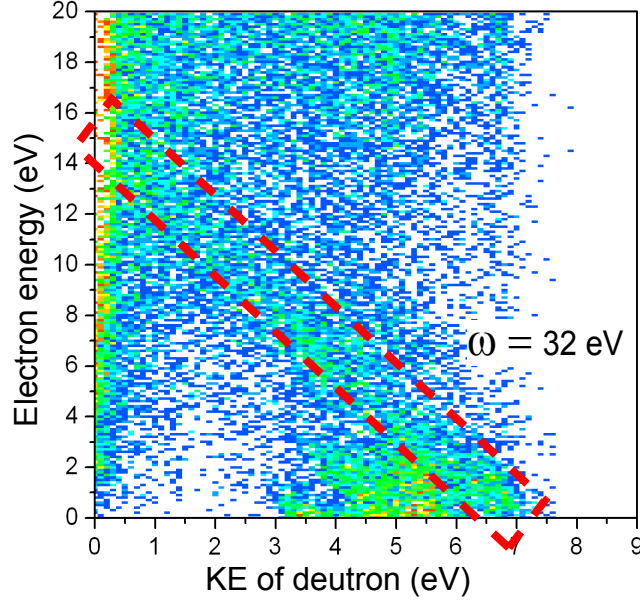


Figure 5.7: The energy correlation plot for perpendicular transitions selecting the photon energy of 32 eV.

In the energy correlation plots for perpendicular transitions, we identify the intense distribution which makes an intercept at the  $KE=0$  axis at an  $E_e = 14(\pm 1)$ eV. This corresponds to ionization by harmonics with energy  $E_{XUV} = 32(\pm 1)$  eV (Fig. 5.7). For ions with  $KE$  in the range 0-0.5 eV, which we assigned to dissociation following direct ionization to the  $1s\sigma_g$  state, the corresponding EMD (not shown here) is strongly aligned along the axis perpendicular to the molecular axis, in line with the prediction of a predominantly  $p\pi_u$  symmetry for the outgoing electron wave [Hik02, Laf03, Sem03]. However, for higher  $KE$ s the EMDs have  $d\pi$  symmetry as expected [Hik02, Laf03, Mar07]. As shown in the upper right corner of Fig. 5.8, the molecular axis is oriented such that the deuteron is observed along the positive  $x'$  axis. With respect to the deuteron emission direction, we can define  $N_{up}$  ( $N_{down}$ ) as the number of electrons which were emitted in the direction (opposite to that) of the deuteron, i.e, those which have  $p_x^e > 0 (< 0)$ . Therefore,

$$a_{\perp} = \frac{N_{up} - N_{down}}{N_{up} + N_{down}} \quad (5.11)$$

defines the asymmetry parameter of the electron distribution in the molecular frame with respect to the deuteron for transverse transitions.

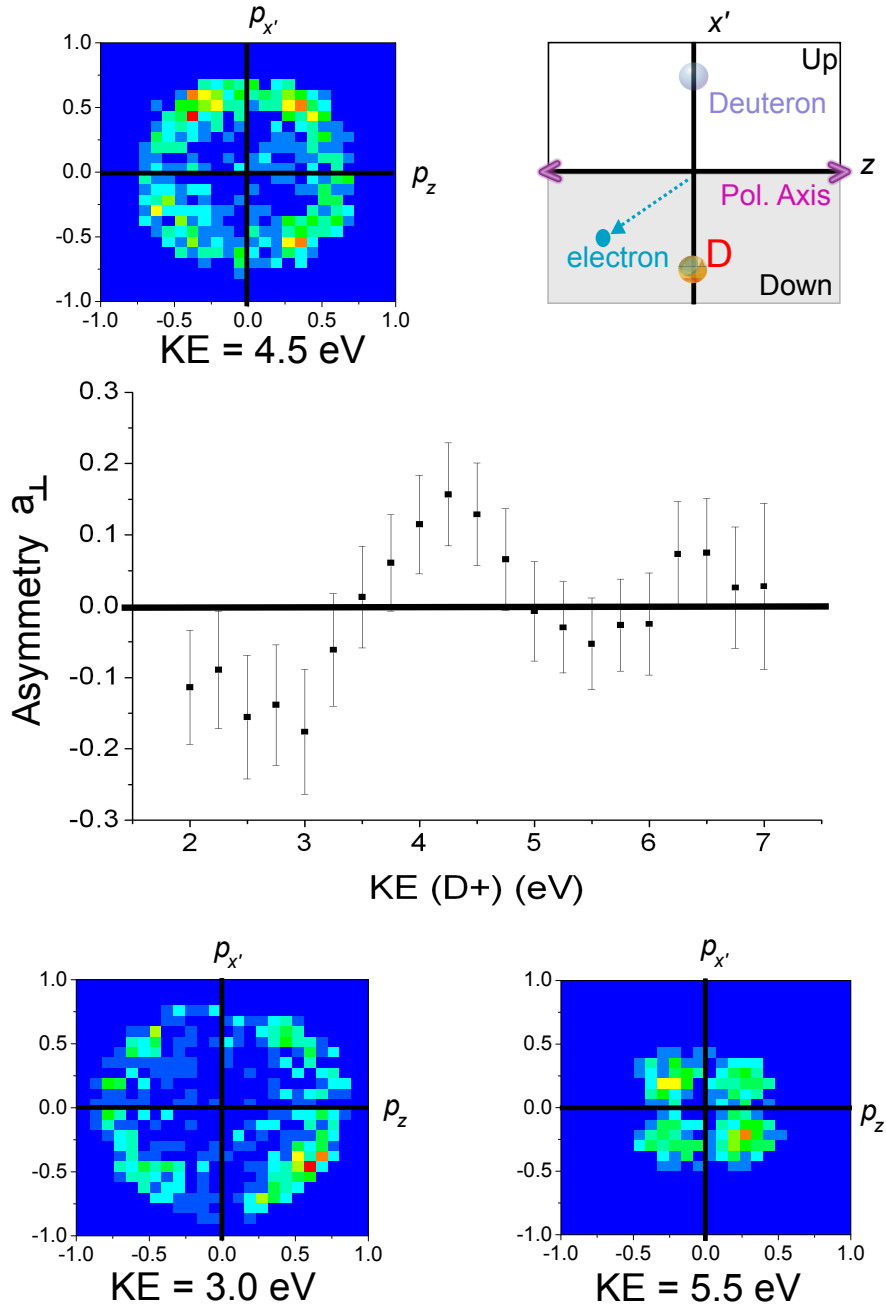


Figure 5.8: The MFEMDs for perpendicular transitions with  $E_{XUV} = 32(\pm 1) \text{ eV}$ . In the right hand corner of the upper panel the geometry of the distributions is illustrated. In the central panel the up-down electron asymmetry parameter with respect to the deuteron emission direction (upward) is plotted as a function of the  $KE$  of the ions. In the upper panel(left) and in the lower panels EMDs are plotted at select  $KE$ .

For the ions in the  $KE$  range of 2.0-7.0 eV, the corresponding electron momentum distributions were obtained for discrete energies in steps of 0.25 eV, within a window of  $\Delta KE = \pm 0.3$  eV, at each value of the  $KE$ . From these distributions, the asymmetry parameter  $a_{\perp}$  was obtained as a function of the discrete  $KE$  values. Fig. 5.8 summarizes the key results for MFEMDs for perpendicular transitions. In the central panel is plotted the  $a_{\perp}$  of the distributions against the  $KE$  of the deuteron. A positive value of  $a_{\perp}$  indicates a predominant emission of the electron in the same direction as the deuteron. A clear oscillation of the  $a_{\perp}$  parameter as a function of the  $KE$  is visible, with the largest asymmetries seen for  $KE = 3.0$  eV, at  $a_{\perp} = -0.18$  and  $KE = 4.25$  eV, at  $a_{\perp} = 0.15$ . In the upper and lower panels, the projections of the electronic distributions at the certain  $KE$  values on to the  $x'z$  plane are plotted. With increasing  $KE$  for the ions, electron emission along the  $z$  axis seems suppressed, whereas for higher  $KE$ s, the distributions have a four lobe structure with clear nodes along the  $x'$  and  $z$  axes.

### 5.3.5 MFEMD for parallel transitions, $E_{XUV} = 32(\pm 1)$ eV and $29(\pm 1)$ eV

For parallel transitions, the molecular and polarization axes coincide. Again, with respect to the deuteron emission direction, now, we can define  $N_{right}$  and  $N_{left}$  for the number of electrons with  $p_z^e > 0$  and  $p_z^e < 0$ , respectively. The asymmetry parameter for the electron distribution for parallel transitions is defined as

$$a_{\parallel} = \frac{N_{right} - N_{left}}{N_{right} + N_{left}} \quad (5.12)$$

In the central panel of Fig 5.9, we plot  $a_{\parallel}$  as a function of the  $KE$ , selecting a photon energy of  $32(\pm 1)$  eV in the energy correlation plot. Within the error bars of the statistics, an oscillation of the  $a_{\parallel}$  parameter is just visible, which is better resolved at higher  $KE$  values. In contrast to the perpendicular transitions, the maximum asymmetry shifts to higher  $KE$  values,  $a_{\parallel} = 0.18$  at  $KE = 5.5$  eV and  $a_{\parallel} = -0.18$  at  $KE = 6.75$  eV. The projections of the electron distributions on the  $x'z$  plane plotted at selected  $KE$  values now are aligned along the polarization/molecular axis, as expected, indicating a  $p\sigma$ -like behavior for the outgoing electron wave. Finally in Fig. 5.10, we plot the  $a_{\parallel}$  parameter for a photon energy of 29 eV, where for the asymmetry parameter, vis-à-vis the  $KE$  of the ions, being greatly reduced, no trend is discernible within the error bars.

## 5.4 Discussion and analysis

To understand the origin of the asymmetry in the electron distributions, let us consider the  $\sigma_g$  and  $\sigma_u$  wave functions in Fig. 5.11. Since all physical observables are proportional to the square of the wave function or the transition matrix elements, the negative (positive) parity of the wave function for the  $\sigma_u$  ( $\sigma_g$ ) does not manifest in an experiment where in the final state only a pure  $\sigma_u$  ( $\sigma_g$ ) wave function is involved. On the contrary, if the final state

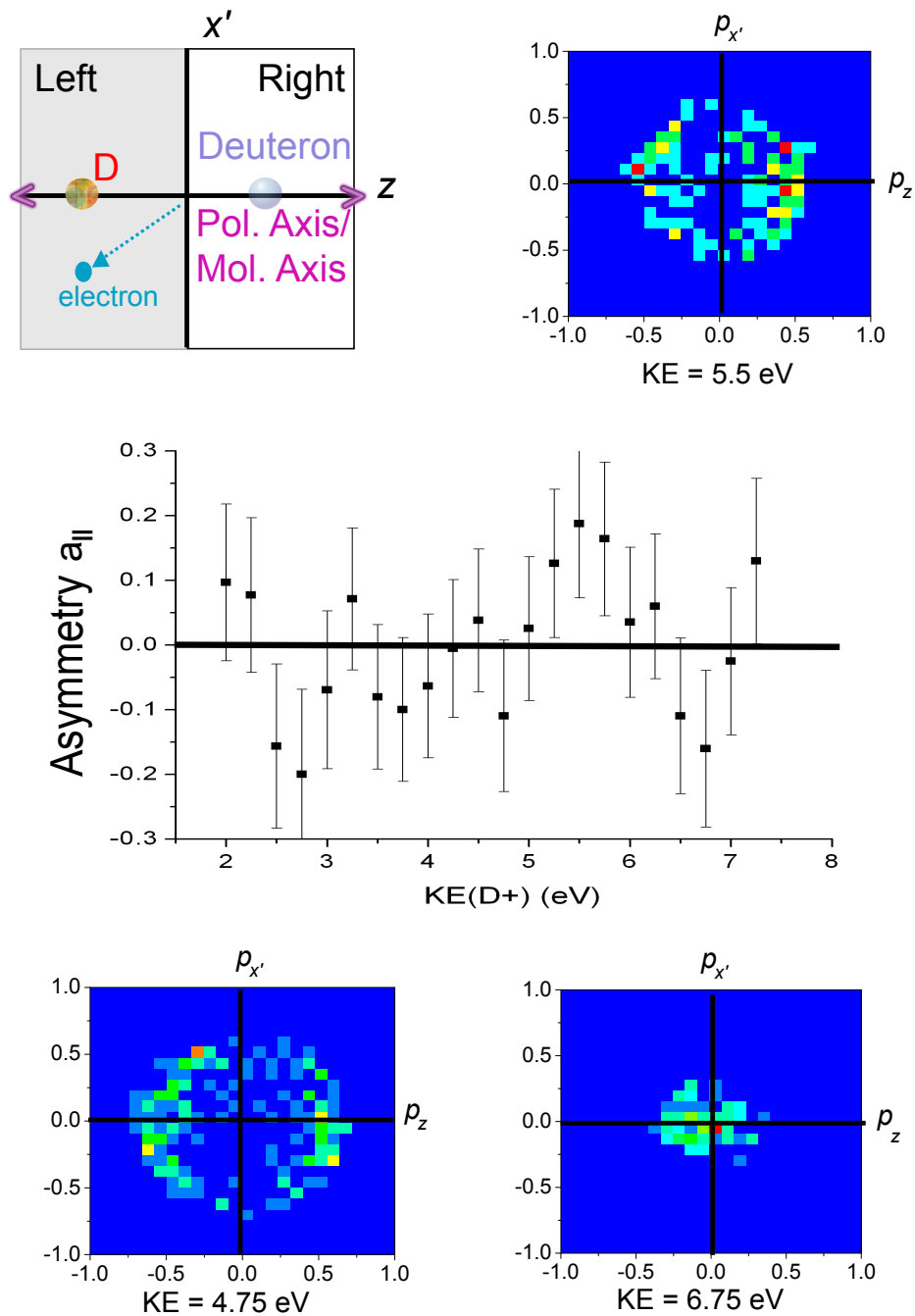


Figure 5.9: The MFEMDs for parallel transitions with  $E_{XUV} = 32(\pm 1)$  eV. In the left hand corner of the upper panel the geometry of the distributions is illustrated. In the central panel the left-right electron asymmetry parameter with respect to the deuteron emission direction (towards the right) is plotted as a function of the  $KE$  of the ions. In the upper panel (right) and in the lower panels EMDs are plotted at selected  $KE$ .

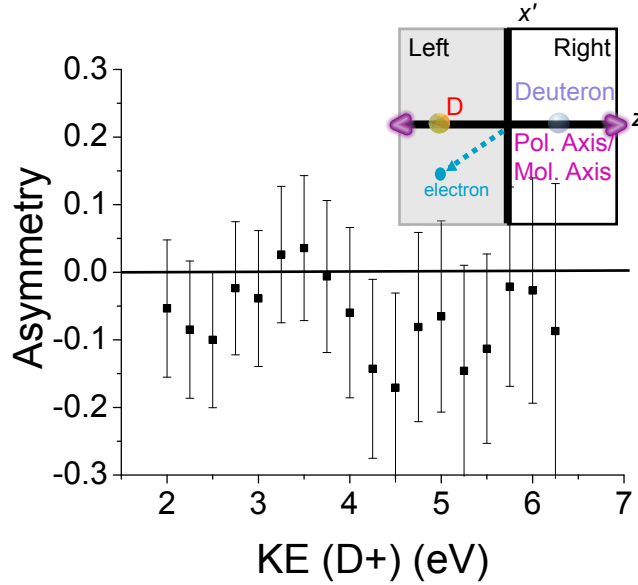


Figure 5.10: The left-right electron asymmetry parameter with respect to the deuteron emission direction (towards the right) is plotted as a function of the  $KE$  of the ions for photon energy of 29 eV. In the upper left corner the geometry is illustrated.

can be expressed as a coherent superposition of both the  $\sigma_u$  and  $\sigma_g$  wave functions, then depending on the linear combination coefficients, antisymmetric probability distributions can be obtained as illustrated in Fig. 5.11. In the context of  $D_2^+$ , at large internuclear distances, the  $1s\sigma_g$  and the  $2p\sigma_u$  curves become degenerate, so the molecular ion state has to be described as combination of these two wave functions. The linear combination leading to an antisymmetric probability distribution, can then be associated with the dissociated state  $D^+ + D$ , where the electron is finally localized on one of the nuclei.

In the discussion in the previous paragraph, the localization of the lone electron on either one of the two nuclei was independent of the way in which the molecular ion itself was formed. In other words, the photoelectron accompanying the formation of  $D_2^+$  during ionization can yield no information about the localization of the second electron. Hence, with respect to the photoelectron, the deuteron is found to be symmetrically distributed, or from the point of view of the deuteron, the electron distribution is symmetric. However, the transient molecular ion can potentially "remember" the direction of the departed electron, provided that, during the photoionization, the molecular ion is formed in a state that is a linear combination of both the  $1s\sigma_g$  and the  $2p\sigma_u$  wave functions. Then, the symmetry of the dissociation is broken (as in Fig. 5.11), and the electron distribution in the molecular frame exhibits a left-right asymmetry, with respect to the direction of the emission of the deuteron [Mar07].

In a direct process (Fig. 5.2(a) and (b)), where these two states are populated by the

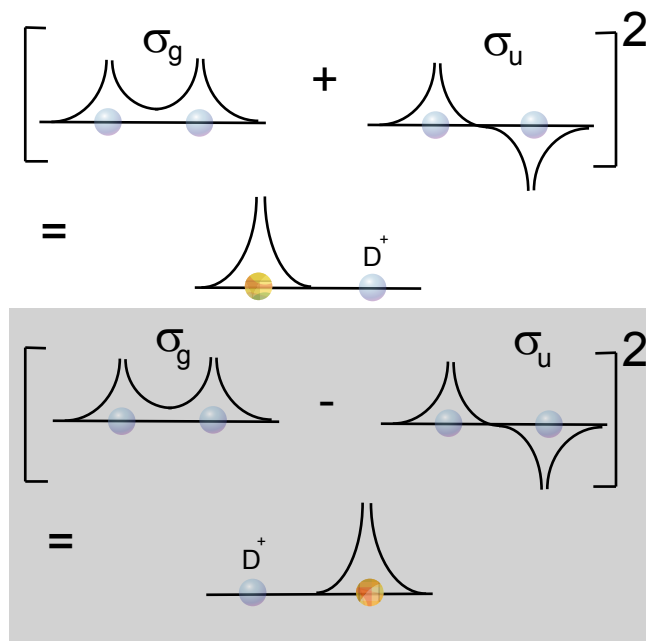


Figure 5.11: A pictorial representation of the origin of asymmetry from the coherent superposition of a  $\sigma_g$  and  $\sigma_u$  state.

same photon, the energy difference between the states translates to different photoelectron energies, thereby making them distinguishable. It may be noted that in direct transitions occurring outside the Franck-Condon region, both the states can be populated, such that the final states are indistinguishable. However, the probability of such a channel is negligible. On the other hand, we may now specifically consider parallel transitions, as in the left panel of Fig. 5.12, where the  $Q_1$  states are available to be resonantly populated by an energetic photon (orange curves). These states have a lifetime of  $\sim 2$  fs [Per09], following which they decay with the release of an autoionized electron with energy  $E_e$  and the molecular ion relaxes into a  $1s\sigma_g$  state. At the same time, there exists the direct ionization channel which populates the  $2p\sigma_u$  state (blue curves), with the formation of an electron with the same energy  $E_e$ <sup>7</sup>. Now, in an experiment, these two electrons are indistinguishable, forcing the molecular ion to be in a coherent superposition of the two states. Depending on the relative phase (which depends on the  $KER$  of the ions) between the  $1s\sigma_g$  and  $2p\sigma_u$  states, the bound electron localizes on either one of the two nuclei. This symmetry breaking in the dissociation process manifests as a  $KER$  (or  $KE$ ) -dependent left-right asymmetry of the photoelectron distribution in the molecular frame.

For perpendicular transitions, the picture (right panel of Fig. 5.12) is a little more involved. The two states,  $1s\sigma_g$  and  $2p\sigma_u$ , are now populated through autoionization from the lowest  $Q_2$  state (green and orange curves, respectively). Again, we can find a range

<sup>7</sup>by energy conservation the  $KER$  for the two competing processes are also the same

of  $KER$  where,  $KER_1 = KER_2$ , and therefore, the molecular ion is found in a coherent superposition of the two opposite parity states,  $1s\sigma_g$  and  $2p\sigma_u$ . Theory [Fer09], therefore, predicts an asymmetry in electron distributions from the interference of the two pathways, shown as orange and green curves in the right panel of Fig. 5.12, clearly seen in recent experiments [Laf03, Mar07] and also here, in Fig. 5.8. *Ab initio* four body quantum calculations [Mar07, Fer09] show that the ions in the  $KE$  range 3-7 eV lie in the overlap region of the  $KE$  distributions arising from dissociation along the  $1s\sigma_g$  and the  $2p\sigma_u$  curves, hence predicting the interference of the two channels in this  $KE$  region. Furthermore, by turning off the resonant ionization channel  $Q_2$ , it was seen that the asymmetry vanished, lending support to the conclusion that the observed asymmetry resulted from the interference between the two path ways, populated by the autoionization of the  $Q_2$  states. Thus, in the single-photon DPI of  $D_2$  ( $H_2$ ) the nuclear (molecular dissociation) and electron (photoionization/autoionization) dynamics can be coupled, manifesting as a  $KE$  dependent asymmetric emission of the electron in the molecular frame.

At this point we may raise an interesting question: upon what parameters of the XUV radiation does this coupling depend on? This is of significance to the present experiment, since here, as against previous measurements with nanosecond synchrotron-based XUV pulses, ultrashort, coherent XUV pulses<sup>8</sup>, from a HHG-based source, have been used. Furthermore, as will be shown later (next section), with HHG-based sources, the pulse duration can be tuned so as to generate isolated,  $\sim 300$  attosecond pulses. In fact, recent theoretical studies of DPI with such ultrashort pulses [Per09, Mor09] have shown that for  $H_2$  with an autoionization time for the lowest  $Q_1$  state of  $\sim 2$  fs, the left-right electron asymmetry vanishes in DPI with XUV pulses ( $\omega = 33$  eV) of durations  $\leq 2$  fs. On the other hand, the asymmetry reaches a maximum and stays constant for pulse durations  $\geq 10$  fs. An interesting implication of the pulse-duration dependent electron asymmetry is a possible route to experimentally determining the autoionization time of the  $Q_1$  state. Additionally, in [Mor09], a detailed analysis of the deuteron (proton) kinetic energy and electron angular distributions has been undertaken for a diverse range of pulse characteristics, varying the spectrum, chirp and duration of the ultrashort XUV pulses.

These are, to the best of the author's knowledge, however, the only available calculations for DPI in  $D_2/H_2$ , particularly with ultrashort pulses. In an endeavor to compare the present experimental data with theory, shown here, in Fig. 5.13, are the preliminary results of the calculations of Fernando Martin, for ultrashort XUV pulse trains with parameters closest to the present experimental conditions. In the inset of Fig. 5.13(a) are sketched the vector potentials of the fields considered in the calculation. Of significance to the measurements here are only the fields in the black and red curves, corresponding to XUV ( $E_{XUV} = 30$  eV) pulse trains comparable to those available here [Sans09b]. In the Fig. 5.13(a) are plotted the corresponding kinetic energy distributions, with emphasis on the contributions from dissociation along the  $1s\sigma_g$  curve (solid red and black curves) and the  $2p\sigma_u$  curve (broken red and black curves). In Fig. 5.13(b) the left right electron asymmetry parameter as a function of the  $KE$  of the ions for the calculations (red and black curves)

<sup>8</sup>more precisely pulse trains under an envelope of  $\sim 15$  fs

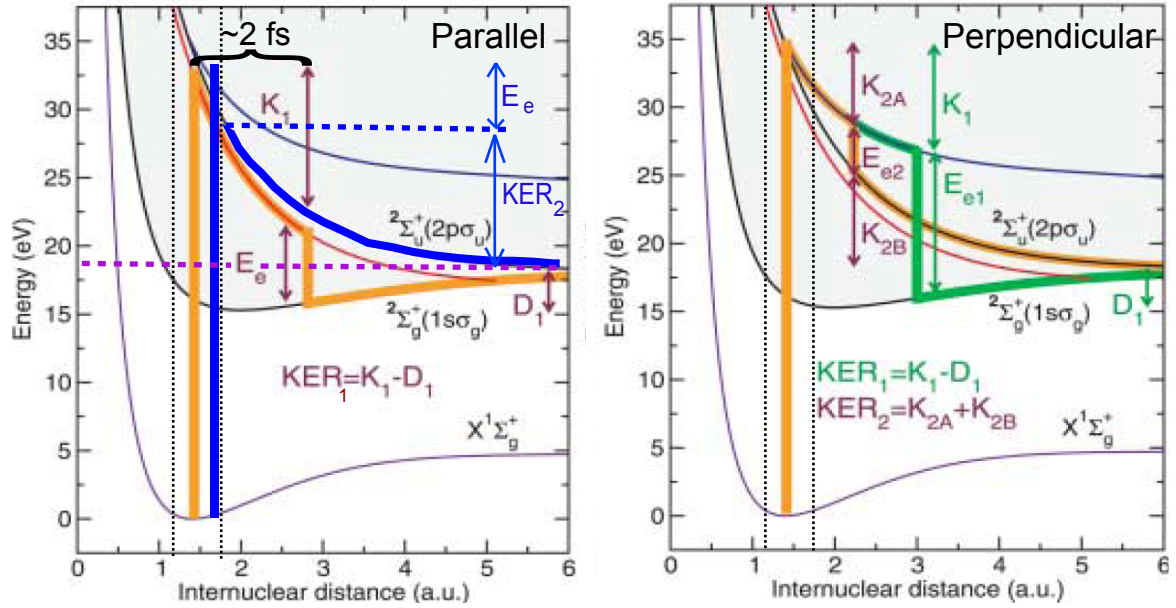


Figure 5.12: (Left panel) At a given photon energy, for parallel transitions, the direct ionization path (blue curves) results in the deuteron being formed in a  $2p\sigma_u$  state with a  $KE = KER_2/2$  (green) and an electron with energy  $E_e$ . Alternatively, within the Franck-Condon overlap (demarcated by broken vertical lines), a resonant photon can excite the  $D_2$  molecule to the  $Q_1$  doubly excited state (orange curves). With a lifetime of  $\sim 2$  fs, the excited state decays, leading to autoionization of one of the electrons, with energy  $E_e$  (brown) and the ion relaxes to the  $1s\sigma_g$  state with a final  $KE = KER_1/2$ . For the same electron energy  $E_e$ , the above two paths cannot be distinguished, and the final molecular ion wave function is coherent superposition of the  $1s\sigma_g$  and  $2p\sigma_u$  states. (Right panel) The interfering pathways for perpendicular transitions are  $Q_2 \rightarrow 2p\sigma_u$  (orange) and  $Q_2 \rightarrow 1s\sigma_g$  (green).

are presented. The theoretical asymmetry curve (black), relevant to this experiment, is compared to the asymmetry at discrete  $KE$  points obtained in this experiment (see Fig. 5.9).

A qualitative agreement for the two asymmetry curves can be seen in the sense that an oscillation of the asymmetry is evident for both, the experimental and theoretical curves. Furthermore, the absolute values of the maximum asymmetry, seen in the  $KE$  region of 5-7 eV, are nearly the same for both the curves. However, in the higher  $KE$  region, an artificial cut off at  $\sim 7.2$  eV is imposed in the experimental data on account of selecting events corresponding to a single photon ( $32 \pm 1$  eV), which precludes comparison with calculations for  $KE$  greater than this value. Furthermore, the calculations predict a more rapid oscillation of the asymmetry with  $KE$ , with a period of  $\sim 1$  eV. On the contrary, the oscillation in the experimental data seems to be slower, with almost twice the period.

At the time of writing this thesis, the origin of this discrepancy was not yet resolved.

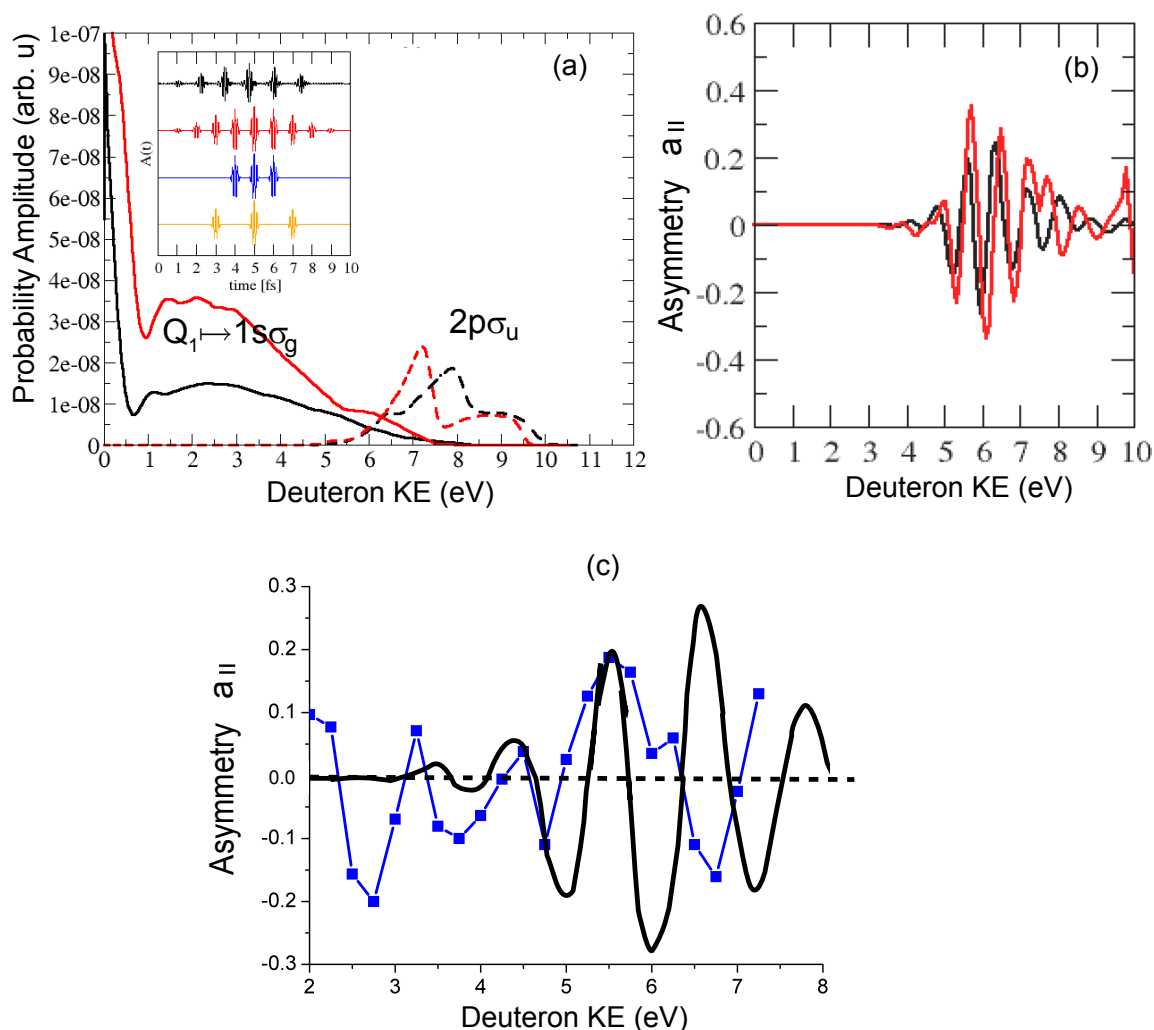


Figure 5.13: a) Calculations from Fernando Martin for DPI of  $D_2$  with an XUV pulse train. In the inset is plotted the vector potential of the XUV field used in the calculations. The red curve represents the vector potential of an ideal pulse train of 9 XUV pulses with a period that is half of the driving IR field generating the pulse train. The black curve is the time structure for an XUV pulse train obtained through TDSE simulations of high harmonic generation by an intense IR pulse (FWHM  $\sim 25$  fs) [Sans09a], best replicating the present experimental conditions. For the vector fields given by the black and red curves, the corresponding  $KE$  distributions highlighting the contributions from the  $1s\sigma_g$  dissociation curve (solid curves) and from the  $2p\sigma_u$  dissociation curve (broken curves). (b) The calculated (red and black) left-right electron asymmetry parameter as a function of the ion  $KE$ . (c) The comparison between the experimental (blue dots) and calculated (black) asymmetry parameter curves. The error bars for the experimental data are omitted for better visibility. The blue lines are also an aid for visibility.

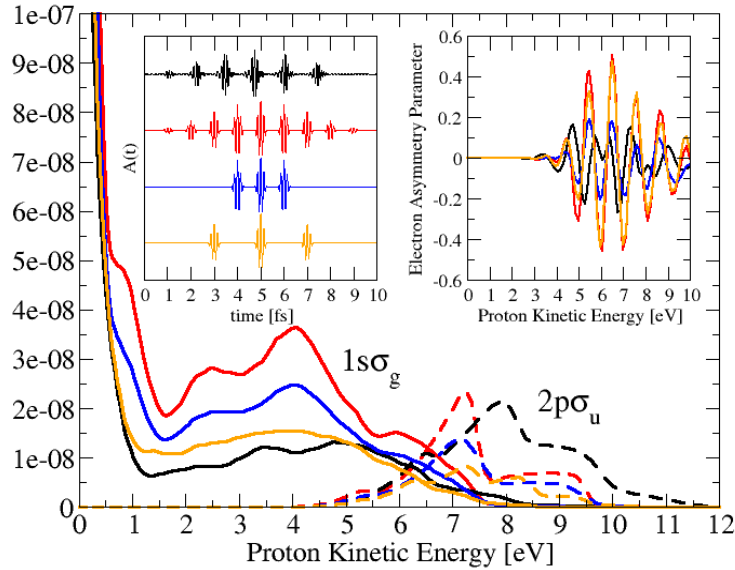


Figure 5.14: Calculations from Fernando Martin for DPI of  $H_2$  with XUV pulse trains. (inset left corner) The vector potentials of the XUV field, with the parameters given above. (inset right corner) The calculated left-right electron asymmetry parameters.

Here, we may refer to recent theoretical work, where it has been shown that the exact details of the asymmetry for DPI with coherent pulses is complexly dependent on the exact temporal and spectral characteristics of the pulse [Mor09]. While calculations with varied forms and spectral phases have been discussed in Ref. [Mor09], we show here (Fig. 5.14) as an illustration, calculations for  $H_2$  for the same pulses considered for  $D_2$  exhibiting a different behavior for the asymmetry parameter, which emphasizes the need to have *a priori* information on the details on the pulse. In the present experiment, we have however, no information on the spectral phase of the XUV pulse, rather, only on the duration.

## 5.5 Conclusions and outlook

In future experiments, a complete reconstruction of the temporal structure of the XUV pulse is envisaged through the technique of RABITT [Mul02], allowing a better comparison with theory. Moreover, experiments with  $H_2$  are also being planned and executed to provide a better understanding of the isotope dependence on coupled electron-nuclear dynamics. Additionally, as has been shown in a few laboratories, control over the durations of the XUV pulse can be achieved and thus a systematic study of DPI with decreasing pulse durations may provide us with an estimate of the autoionization widths as predicted in theory [Per09]. In fact, as an example, we provide here results of an experiment to

demonstrate the availability of XUV pulses with envelopes as short as  $\sim 6$ -8 fs at the HHG laboratory at MPI-K.

We refer to [Kel09] for details of a similar experiment in Milan, Italy. In brief, the XUV pulse with a central energy of  $\sim 18$  eV ionizes the  $D_2$  molecule to the  $1s\sigma_g$  level in  $D_2^+$ . The Frank-Condon principle requires that a number of vibrational levels are populated, implying that a coherent, bound vibrational wave packet is excited in  $D_2^+$ . However, when a delayed, moderately intense ( $\sim 10^{12}$  W/cm<sup>2</sup>) IR pulse is applied, then the repulsive  $2p\sigma_u$  level is so modified that it crosses the  $1s\sigma_g$  curve at a finite internuclear distance,  $R_C$ . In this process, called *bond softening*, an avoided crossing is created. So whenever the bound vibrational wave packet reaches  $R_C$ , a part of the wave packet travels along the dissociating curve, leading to  $D^+$  ions. Therefore, at certain delays of the IR pulse, which is given by the vibrational time period, which is  $\sim 24$  fs [Erg06], there is an increase in the  $D^+$  signal. However, if the exciting XUV pulse or the probing IR pulse are longer or comparable in duration to the vibrational period, then the oscillations in the  $D^+$  signal are washed out.

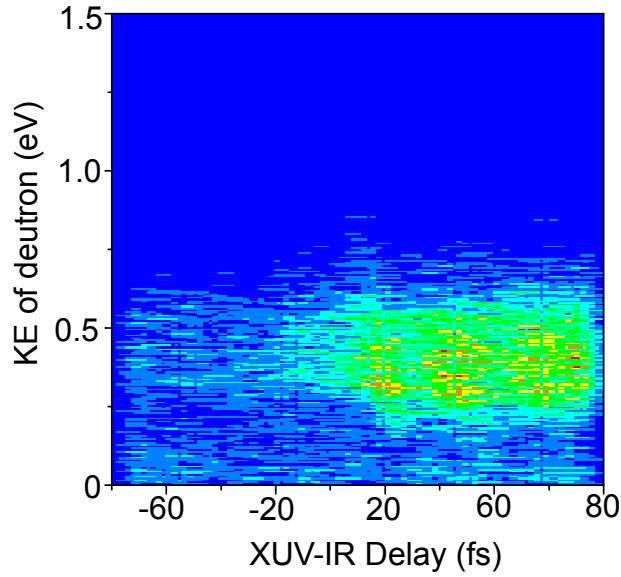


Figure 5.15:  $KE$  vs XUV-IR delay spectrum. For positive delays, the IR comes after the XUV pulse, thereby leading to bond softening in the  $D^+$  molecular ion. The vibrational wave packet dissociates at avoided crossing leading to oscillations in the spectrum with the vibrational period of  $D^+$ .

In Fig. 5.15, we plot on the vertical axes  $KE$  of the  $D^+$  ions as a function of the XUV-IR delay, where positive delays denote that the XUV pulse precedes the IR pulse. For delays  $< 0$ , there is only a constant signal at  $KE \sim 0$  eV, corresponding to ground state dissociation by the XUV pulse. However, for positive delays, we see a clear oscillation of the signal for the bond softening channel at  $KE \sim 0.5$  eV. The period can be easily verified

to be  $\sim 24$  fs, thus indicating that the IR pulses are  $\sim 12$  fs long, while the corresponding envelope of the XUV pulse<sup>9</sup> would therefore be about 6-8 fs long. The details of how such ultrashort IR pulses can be generated is not covered here, and we will refer to [Kre09b] (and references within) for more information.

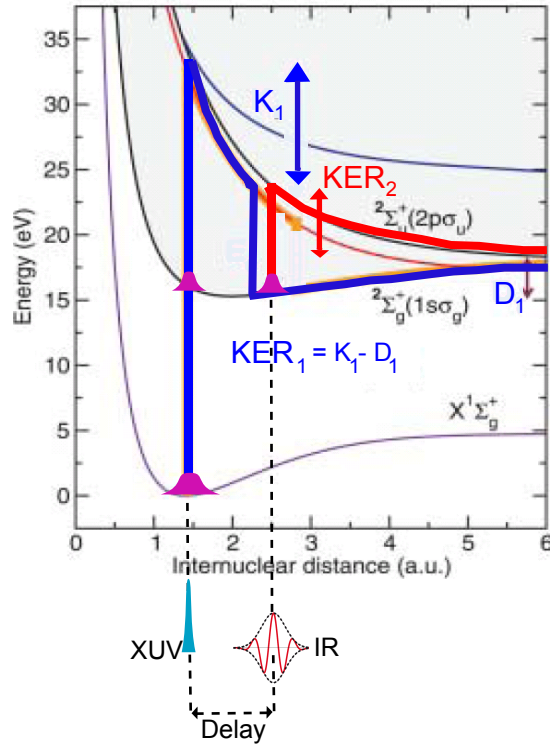


Figure 5.16: In an experiment using isolated ultrashort ( $\sim 300$  attoseconds) XUV pulses (cyan), the  $Q_1$  channel is resonantly excited (blue), and proceeds to decay (blue) on the scale of  $\approx 2$  fs leading to a kinetic energy release,  $KER_1$  through the dissociative continuum of  $1s\sigma_g$ . A delayed, intense, IR pulse can then excite the  $2p\sigma_u$  state (red) from the fraction of the population which is in the bound state of  $1s\sigma_g$ . The repulsive  $2p\sigma_u$  curve leads to energetic fragments with  $KER_2$  (red).

So, in the very immediate future, control over the pulse durations of the XUV pulses will be achieved and we can therefore proceed to exciting experiments with such novel sources used to probe atomic and molecular dynamics on ever shorter time scales. In particular, with reference to the current experiment, the resonant channel  $Q_1 \rightarrow 1s\sigma_g$  can be populated using an isolated XUV pulse as short as  $\sim 300$  attoseconds<sup>10</sup>, and the direct channel can be populated with a delayed moderately intense few-cycle IR pulse ( $\sim 6-7$  fs), so as to study the time-resolved dynamics of the interference of these two DPI pathways

<sup>9</sup>which was generated using the same IR pulse

<sup>10</sup>where we have a single attosecond pulse and not a pulse train

(Fig. 5.16). Theoretical work to describe such two colour interactions is underway, and also first experiments, observing only the ion spectra have been conducted in Milan [Sans09b]. With its electron-ion coincidence capability, the Reaction Microscope would be the ideal tool for a complete characterization of these dynamics. Finally, the successful coupling of these novel light sources with the Reaction Microscope as demonstrated in this current experiment paves the way for future studies on time-resolved dynamics of electron-electron correlation, particularly in the context of a molecular Coulomb field.

In conclusion, we have studied DPI in  $D_2$  for the first time with ultrashort ( $\sim 15$  fs) XUV pulses in a Reaction Microscope. Molecular frame electron momentum distributions show an asymmetry with respect to the direction of deuteron emission dependent on the  $KE$  of the ions for both perpendicular and parallel transitions, in qualitative agreement with previous experiments and theory. Finally, we have also imaged the vibrational wave packet dynamics in  $D_2$ , raising the possibility of studying time-resolved dynamics in the near future, using ultrashort XUV pulses in a Reaction Microscope.



# Chapter 6

## Summary and Outlook

The work presented in this thesis reports on pioneering experiments carried out with forefront, ultrashort, photon sources in combination with a Reaction Microscope. We can broadly classify the experimental results presented here into two sections depending on the nature of the ultrashort laser source used in the measurement.

Part one reports, for the first time, on three-dimensional momentum imaging of Electron Wave Packet interferences in the single ionization of helium, using carrier-envelope-phase (CEP) controlled few-cycle ( $\sim 5$  fs), intense ( $\sim 4 \times 10^{14}$  W/cm<sup>2</sup>) laser pulses (740 nm), in a Reaction Microscope. Preferential emission of low-energy electrons ( $E_e < 15$  eV) to either hemisphere was observed as a function of the CEP. This was accompanied by an asymmetric distribution of peaks, which are different from the multiphoton peaks introduced in Chap. 2. In this work, a model based on SFA theory was developed, where the one-dimensional momentum distribution resulting from the interference of only two Electron Wave Packets (EWPs) arising within a single cycle of the laser pulse were calculated. The correspondence of the calculated interference peaks with the experimental peaks indicates that this experiment demonstrates the possibility of potentially obtaining information about the time-dependent potential in atoms and molecules. Specifically, the first EWP, or 'object' electron wave as in Fig. 6.1, represents a classical trajectory where the electron in the continuum is driven back to the ion and is modified in phase through its interaction with the Coulomb potential. The second 'reference' EWP does not interact with the ion, and thus samples only the potential of the laser field. The 3D momentum distribution can therefore be interpreted as a holographic image of the time-dependent combined potential of the ion and the laser field. As discussed in Sec. 4.5, one may imagine fascinating applications for this holographic technique in mapping the time-dependent potentials in multi-electron systems such as molecules and clusters on the time scale of a few attoseconds (Fig. 6.1). Additionally, future interesting experiments could be designed based on this holographic-principle, using attosecond pulse trains (APTs) containing only 2-3 pulses [Abe09]. The APT would excite the EWPs in to the continuum, and a dressing IR laser field, depending on the time of birth, would drive the EWPs either back to the parent ion (object EWP) or directly to the detector (reference EWP).

In the second part, the construction, performance and operation of a dedicated Reac-

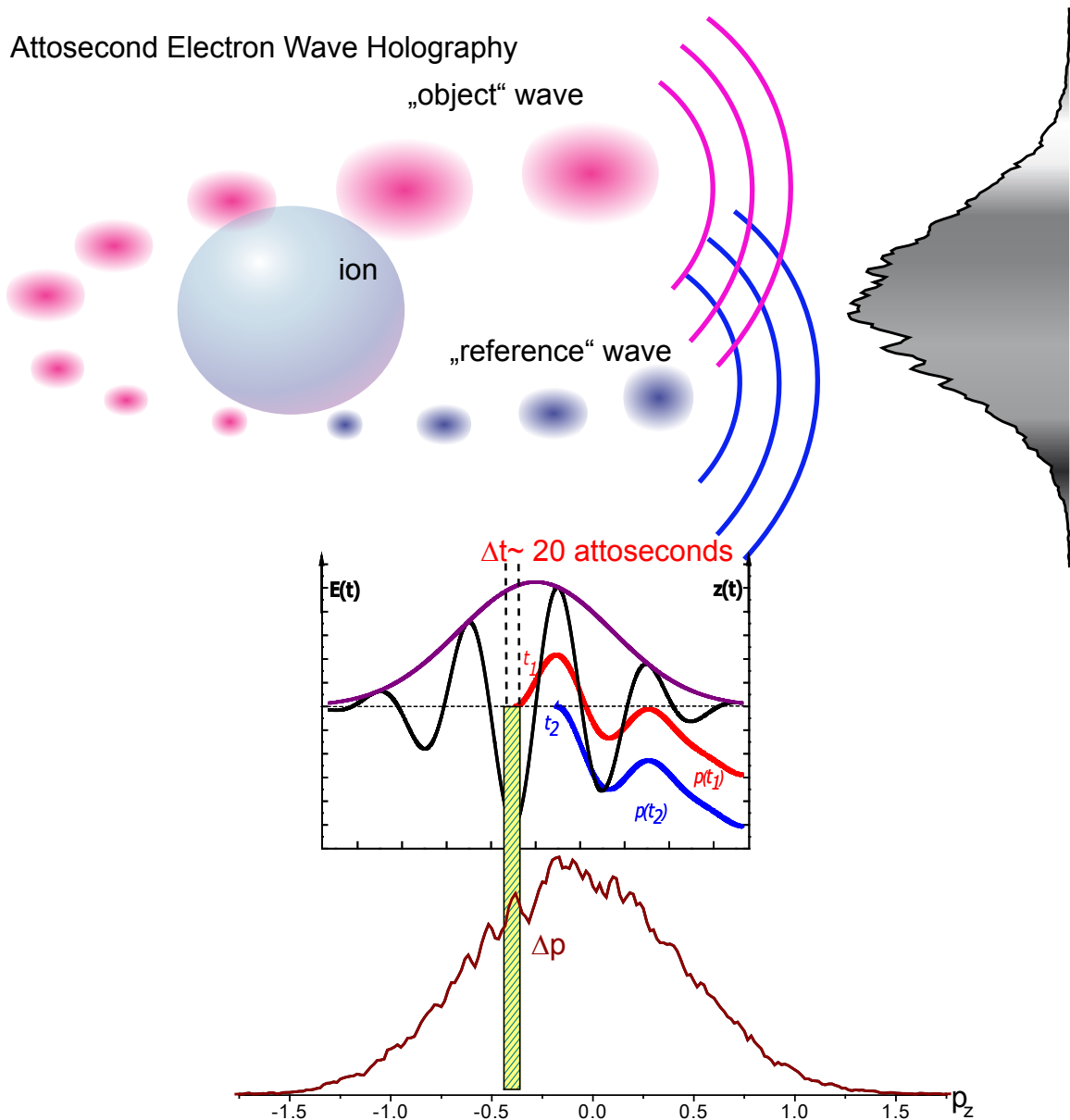


Figure 6.1: In the upper panel is illustrated a possible application of electron wave packet interference using few-cycle laser pulses in 'Attosecond Electron Wave Holography.' The object electron wave (magenta) is driven back to the ion by the laser field and can be modified in phase through its interaction with the ion. The reference electron wave (blue) samples only the driving laser field. The coherent superposition of these two manifests as interference peaks in the momentum domain. In the lower panel, the narrow width of the interference peak ( $\Delta p$ ) attests to the possibility of obtaining an unprecedented time resolution of the order of  $\Delta t \sim 20$  attoseconds.

tion Microscope optimized for studies with low brilliance sources and installed at the HHG laboratory at MPI-K, Heidelberg, has been detailed in Chap. 3. Photoionization experiments with He using the high harmonics attest to a high photon flux of  $> 10^9$  photons per second from the high harmonics source, comparable to only few other facilities in the world. Stable continuous operation for over 72 hours was achieved, highlighting the fact that experiments involving low probability processes in atoms and molecules could be undertaken with this experimental setup. In fact, in Chap. 5 such an experiment investigating the interaction of ultrashort ( $\sim 15$  fs) XUV ( $\sim 32$  eV) pulses with a simple molecule,  $D_2$ , is reported.

In the dissociative photoionization of  $D_2$  only  $\approx 2\%$  of the ionization events lead to dissociation. However, there are multiple pathways to dissociation which could be effectively analyzed and separated through the experimentally obtained kinetic energy distribution of the ions ( $0 \text{ eV} < KE < 8 \text{ eV}$ ) and the coincident electron energy distributions ( $0 \text{ eV} < E_e < 16 \text{ eV}$ ). It further turns out that the kinetic energy spectrum is actually a coherent superposition of these multiple pathways. The interference of these paths which involve molecular states of different symmetry manifests itself as a backward-forward asymmetry of the photoelectron distribution, with respect to the direction of the emission of the deuteron. In this intriguing phenomenon of electron-electron correlation involving doubly excited states, the outgoing photoelectron 'knows' to which nucleus the other bound electron will attach itself. In this work, for the first time, ultrashort XUV pulses have been used to induce this coupling of photoelectron-molecular dissociation dynamics.

The implication of this experiment goes beyond the immediate possibility of studying the time-resolved dynamics of the doubly-excited states as mentioned in the concluding part of the preceding chapter. Rather, the successful coupling of the two frontier technologies of table-top coherent XUV generation with multi-particle coincident momentum imaging paves the way to study a plethora of phenomena in soft X-ray induced molecular dynamics. For example, in molecules such as  $CH_3OH$ , and especially interesting in  $C_2H_2$  and  $C_2H_4$ , the migration of the proton proceeds on a time scales of a hundred fs [His07], accompanied by conformational dynamics of the molecule. So, the XUV pulse can initiate the migration in the molecular ion, whose time resolved dynamics can be probed by a delayed IR pulse. Another interesting possibility is to obtain photoelectron angular distributions from aligned molecules. Sub-fs electron dynamics, or in particular, studying sideband generation with molecular targets is also of contemporary interest [Hae09], experiments for which are being planned with this new setup.



# Appendix A

## Atomic units

In atomic physics the use of *atomic units* is customary. The base units of this system are related to the dimensions of the hydrogen atom.

### Base units and natural constants

$r_e = 1 \text{ a.u.} = 5.2918 \cdot 10^{-11} \text{ m}$	Bohr radius of the K-shell of hydrogen
$m_e = 1 \text{ a.u.} = 9.1095 \cdot 10^{-31} \text{ kg}$	rest mass of the electron
$q_e = e = 1 \text{ a.u.} = 1.6022 \cdot 10^{-19} \text{ As}$	charge of the electron
$\hbar = m_e v_e r_e = 1 \text{ a.u.}$	reduced Planck constant
$c = e^2 / (\hbar \alpha) = 137 \text{ a.u.}$	speed of light

The conversion factors to other commonly used quantities are:

### Conversion factors

energy	$E \text{ [in eV]} = 27.2 \cdot E \text{ [in a.u.]}$
momentum	$p \text{ [in Ns]} = 1.995 \cdot 10^{-24} \cdot p \text{ [in a.u.]}$
time	$t \text{ [in s]} = 4.134 \cdot 10^{16} \cdot t \text{ [in a.u.]}$
velocity	$v_e \text{ [in m/s]} = 2.1877 \cdot 10^6 \cdot v_e \text{ [in a.u.]}$
Laser-field intensity	$I_0 \text{ [in W/cm}^2] \hat{=} 3.51 \cdot 10^{16} \cdot I_0 \text{ [in a.u.]}$



# Bibliography

- [Abe09] M. Abel *et.al.*, Chem. Phys **366**, 9 (2009). [119](#)
- [Ago79] P. Agostini, F. Fabre, G. Mainfray, G. Petite, and N.K. Rahman, Phys. Rev. Lett. **42**,1127 (1979). [9](#)
- [Amm86] M.V. Ammosov, N.B Delone, and N.B. Krainov, Soviet Physics JETP, **64**, 1191 (1986). [13](#)
- [Ant96] P. Antoine, A.  $\acute{L}$  Huillier and M. Lewenstein, Phys. Rev. Lett. **77**, 1234 (1996). [27](#)
- [Arb06] D. G. Arb3, E. Persson, and J. Burgd3rfer, Phys. Rev. A **74**, 063407 (2006). [80](#), [81](#), [85](#), [88](#), [91](#)
- [Aug89] S. Augst, D. Strickland, D. D. Meyerhofer, S. L. Chin, and J. H. Eberly, Phys. Rev. Lett. **63**, 2212 (1989). [11](#), [16](#)
- [Bak06] S. Baker *et.al.*, Science **312**, 424 (2006). [80](#)
- [Bal93] Ph. Balcou and A.  $\acute{L}$  Huillier Phys. Rev. A **47**, 1447 (1993). [25](#)
- [Bal03] A. Baltuska *et.al.*, Nature (London) **421**, 611 (2003). [2](#), [24](#)
- [Bec02] W. Becker *et.al.*, Adv. At. Mol. Phys. **48**, 35 (2002). [18](#), [21](#), [77](#), [89](#)
- [Bec05] A. Becker, R. D3rner and R. Moshhammer, J. Phys. B: At. Mol. Opt. Phys. **38**, S753 (2005). [21](#)
- [Bel98] M. Bellini, C. Lyng3, A. Tozzi, M. B. Gaarde, T. W. H3nsch, A.  $\acute{L}$ . Huillier and C.-G. Wahlstr3m, Phys. Rev. Lett. **81**, 297 (1998). [25](#), [30](#)
- [Bet77] H. A. Bethe and E. E. Salpeter *Quantum Mechanics of One- and Two- electron Atoms* 1st ed., Springer (1977). [8](#), [9](#)
- [Boy03] R. W. Boyd, *Nonlinear Optics* 2nd ed., (Academic Press, San Diego 2003). [27](#)
- [Bra00] T. Brabec and F. Krausz, Rev. Mod. Phys., 545 (2000). [2](#), [18](#), [77](#)

- [Bra03] B. H. Bransden and C. J. Joachain, *Physics of Atoms and Molecules* 2nd ed., (Pearson Education, 2003). 6, 8, 35
- [Bro73] R. Browning and J. Fryar, *J. Phys. B* **6**, 364 (1973). 94
- [Bun79] P. R. Bunker, *Molecular Symmetry and Spectroscopy*, (Academic Press, New York, 1979). 40
- [Cam84] R. Campargue, *J. Phys. Chem.* **88**, 4466 (1984) 53
- [Coo68] J. Cooper and R. N. Zare, *J. Chem. Phys.* **48**, 942 (1968). 9
- [Cor89] P. B. Corkum, N. H. Burnett, F. Brunel, *Phys. Rev. Lett.* **62**, 1259 (1989). 13, 16
- [Cor93] P. B. Corkum, *Phys. Rev. Lett.* **71**, 1994 (1993). 20, 22
- [Cor01] E. Cormier, D. Garzella, P. Breger, P. Agostini, G. Chériaux and C Leblanc, *J. Phys. B: At. Mol. Opt. Phys.* **34**, L9 (2001). 11
- [Cha97] Z. Chang, A. Rundquist, H. Wang, M. M. Murnane, and H. C. Kapteyn, *Phys. Rev. Lett.* **79**, 2967 (1997). 24
- [Chu93] Y M. Chung, E.-M. Lee, T. Masuoka, and J. A. R. Samson, *J. Chem. Phys.* **99**, 885 (1993) 94, 95
- [Ced99] L.S. Cederbaum and J. Zobeley, *Chem. Phys. Lett.* **307**, 885 (1999) 205. 93
- [CXRO] [http://henke.lbl.gov/optical\\_constants/mirror2.html](http://henke.lbl.gov/optical_constants/mirror2.html) 51
- [Deh78] J. L Dehmer and D. Dill, *Phys. Rev. A.* **18**, 164 (1978). 34, 40, 99
- [Del91] N.B Delone and V.P. Krainov, *J. Opt.Soc. Am. B*, **8**, 1207 (1991).
- [Del00] N.B Delone and V.P. Krainov, *Multiphoton Processes in Atoms (Springer Series on Atomic, Optical, and Plasma Physics)* (Springer, 2000). 9
- [Dew06] S. Dewald, *Erzeugung intensiver Lichtfelder mit einem Laseroszillator und deren Wechselwirkung mit Atomen*, PhD Thesis, Ruperto-Carola University of Heidelberg (2006). 3, 43, 76
- [Dil76] D. Dill, *J. Chem. Phys.***65**, 1130 (1976). 97, 103
- [Din03] L. C. Dinu *et al.*, *Phys. Rev. Lett.* **91**, 063901 (2003). 24, 27
- [Dor90] M. Dörr, R. M. Potvliege, and R. Shakeshaft, *Phys. Rev. Lett.* **64**, 2003 (1990). 16
- [Dor96] R. Dörner *et.al.*, *Phys. Rev. Lett.* **76**, 2654 (1996). 5, 6

- [Dor02] . Dörner, Th. Weber, M. Weckenbrock, A. Staudte, M. Hattass, R. Moshhammer, J. Ullrich, and H. Schmidt-Böcking, *Adv. At. Mol. Opt. Phys.* **48**, 1 (2002).
- [Dow09] D. Dowek, Y. J. Picard, P. Billaud, C. Elkharrat, J. C. Houver, *Chin. J. Chem. Phys.* **22** 178 (2009).
- [Dow07] D Dowek, J Fernandez, M Lebech, J C Houver and F Martin, *J. Phys.: Conf. Ser.* **88**, 012009 (2007).
- [Dre02] M. Drescher *et.al.*, *Nature (London)* **419** 803 (2002). [93](#)
- [Dur06] M. Dürr, *Electron Induced Break-up of Helium: Benchmark Experiments on a Dynamical Four-Body Coulomb System*, PhD Thesis, Ruperto-Carola University of Heidelberg (2006). [58](#), [69](#)
- [Dun76] G. H. Dunn, *Phys. Rev. Lett.* **8**, 62 (1962). [40](#)
- [Erg06] Th. Ergler, A. Rudenko, B. Feuerstein, K. Zrost, C. D. Schröter, R. Moshhammer, and J. Ullrich *Phys. Rev. Lett.* **97**, 193001 (2006). [93](#), [115](#)
- [Esa09] E. Esarey, C. B. Schroeder, and W. P. Leemans, *Rev. Mod. Phys.* **81**, 1229 (2009) [1](#)
- [Fai86] F. H. M. Faisal, *Theory of Multiphoton Processes*, (Plenum Press, New York 1986). [10](#)
- [Fab82] F. Fabre, G. Petite, P. Agostini, and M. Clement, *J. Phys. B: At. Mol. Opt. Phys.* **15**, 1353 (1982). [11](#)
- [Fan83] U. Fano, *Rep. Prog. Phys.* **46**, 97 (1983). [93](#)
- [Fed97] M. Federov, *Atoms and Free Electrons in a Strong Light Field*, (World Scientific Singapore-New Jersey-London-Hong Kong, 1997). [8](#)
- [Fer88] M. Ferray, A. L. Huillier, X. F. Li, G. Mainfray, and C. Manus, *J. Phys. B: At. Mol. Opt. Phys* **21**, L31 (1988). [20](#), [21](#), [23](#)
- [Fer09] J. Fernández and F. Martín, *New J. Phys.*, **11**, 043020(2009). [94](#), [111](#)
- [Fis03] D. Fischer, *Mehr-Teilchen-Dynamik in der Einfach- und Doppelionisation von Helium durch geladene Projektile*, PhD Thesis, Ruperto-Carola University of Heidelberg (2003). [57](#), [62](#), [69](#)
- [FLA09] HASYLAB at DESY, Notkestr. 85, D-22607 HAMBURG, Germany, [http://hasylab.desy.de/facilities/flash/index\\_eng.html](http://hasylab.desy.de/facilities/flash/index_eng.html).
- [Fre87] R.R. Freeman, P.H. Bucksbaum, H. Milchberg, S. Darack, D. Schumacher, and M.E. Geusic, *Phys. Rev. Lett.* **59**, 1092 (1987).

- [Gag07] E. Gagnon, P. Ranitovic, X-M. Tong, M. M. Murnane, H. C. Kapteyn, A. S. Sandhu, *Science* **317**, 1374 (2007). [2](#), [34](#), [93](#)
- [Gag08] E. Gagnon, *Femtosecond molecular dynamics driven by extreme ultra violet radiation*, PhD Thesis, University of Colorado (2008). [3](#)
- [Gar75] J. L Gardner and J. A. R. Samson, *Phys. Rev. A.* **12**, 1404 (1975). [100](#)
- [Ged93] J. Geddes, K. F. Dunn, N. Kouchi, M. A. McDonald, V. Srigengan and C. J. Latimer, *J. Phys. B* **27**, 2961 (1994).
- [Gop09] R. Gopal *et.al.* *Phys. Rev. Lett.* **103**, 053001 (2009). [4](#)
- [Gou05] E. Goulielmakis, *Complete characterization of light waves using attosecond pulses*, PhD Thesis, Max-Planck-Institut für Quantenoptik (2005). [2](#), [3](#), [75](#), [79](#), [81](#)
- [Gou08] E. Goulielmakis *et.al.* *Science* **320**, 1614 (2008). [79](#)
- [Gus07] E. Gustafsson *et.al.*, *Opt. Lett.* **32**, 1353 (2007). [29](#)
- [Hae09] S. Haessler *et.al.*, *Phys. Rev. A* **80**, 011404(R) (2009). [121](#)
- [Har78] D. C. Harris and M. D. Bertolucci, *Symmetry and Spectroscopy*, (Dover, New York, 1978). [40](#)
- [He95] Z. X. He, J. N. Cutler, S. H. Southworth, L. R. Hughey, and J.A. R. Samson, *J. Chem. Phys.* **103**, 3912 (1995) [95](#), [97](#)
- [Hik02] Y. Hikosaka and J.H.D. Eland, *Chem. Phys.*, **277**, 53 (2002). [34](#), [97](#), [99](#), [105](#)
- [Hik03] Y. Hikosaka and J.H.D. Eland, *J. Electron Spectrosc. Relat. Phenom.*, **133**, 77 (2003). [34](#), [97](#)
- [His07] A. Hishikawa, A. Matsuda, M. Fushitani, and E. J. Takahashi, *Phys. Rev. Lett.* **99**, 258302 (2007). [121](#)
- [Hol72] J. M. Hollas, *Symmetry in Molecules*, (Chapman and Hall, London, 1972). [40](#)
- [Hui90] A. ´L Huillier K. J. Schafer, and K. C. Kulander, *Phys. Rev. Lett.* **66**, 2200 (1990) [25](#)
- [Hui92] A. ´L Huillier and Ph. Balcou, *Phys. Rev. Lett.* **70**, 774 (1992). [20](#), [24](#)
- [Ita04] J. Itatani *et.al.*, *Nature (London)* **432**, 867 (2004). [80](#)
- [Ito96] K. Ito, R. I. Hall and M. Ukai, *J. Chem. Phys* **104**, 8449 (1996). [95](#), [97](#), [99](#), [100](#)
- [Ito96] K. Ito, J. Adachi, R. Hall, S. Motoki, E. Shigemasa, K. Soejima, A. Yagishita, *J. Phys. B* **33**, 527 (2000). [97](#)

- [deJ04] V. L. B. de Jesus, A. Rudenko, B. Feuerstein, K. Zrost, C. D. Schröter, R. Moshhammer, and J. Ullrich, *J. Electron Spectrosc. Relat. Phenom.*, **141**, 127 (2004). [57](#), [72](#)
- [JILA09] <http://jila.colorado.edu/kmgroupp/> [2](#)
- [Joh05] P. Johnsson *et.al.*, *Phys. Rev. Lett.* **95**, 013001 (2005). [32](#), [33](#)
- [Joh06] P. Johnsson *et.al.*, *J. Mod. Opt.* **53**, 233 (2006). [29](#), [30](#), [34](#)
- [Kan83] S. Kanfer and M. Shapiro, *J. Phys. B* **16**, L655 (1983). [97](#)
- [Kel64] L.V. Keldysh. *Soviet Physics JETP*, **20**,1307 (1964). [11](#)
- [Kel09] F. Kelkensberg *et.al.*, *Phys. Rev. Lett.* **103**, 123005 (2009). [115](#)
- [Kir48] P. Kirkpatrick and A. V. Baez, *J. Opt. Soc. Am.* **38**, 766 (1948). [49](#)
- [Khe01] A. Kheifets, *J. Phys. B: At. Mol. Opt. Phys.* **34**, L247 (2001).
- [Kou97] N. Kouchi, M. Ukai and Y. Hatano, *J. Phys. B: At. Mol. Phys.* **30**, 2319 (1997). [34](#), [93](#)
- [Kir81] K. Kirby, T. Uzer, A.C Allison and A. Dalgarno, *J. Chem. Phys* **75**, 2820 (1981). [97](#)
- [Kli06] M. Kling, F. Krausz, M. J. J. Vrakking, Ch. Siedschlag, J. I. Khan, M. Schultze, T. Uphues, Y. Ni, and M. Drescher, *Science* **312**, 246 (2006). [2](#), [79](#), [93](#)
- [Kra92] J. L. Krause, K. J. Schafer, and K. C. Kulander, *Phys. Rev. Lett.* **68**, 3535(1992). [20](#)
- [Kra09] F. Krausz and M. Ivanov, *Rev. Mod. Phys.* **81**, 163 (2009). [2](#), [93](#)
- [Kre09a] M. Kremer, B. Fischer, B. Feuerstein, V. L. B. de Jesus, V. Sharma, C. Hofrichter, A. Rudenko, U. Thumm, C. D. Schröter, R. Moshhammer, and J. Ullrich, *Phys. Rev. Lett.* **103**, 213003 (2009). [2](#), [79](#), [93](#)
- [Kre09b] M. Kremer, *Einfluß der Träger-Einhüllenden-Phase auf die Wechselwirkung ultrakurzer Laserpulse mit Molekülen*, PhD Thesis, Ruperto-Carola University of Heidelberg (2009). [2](#), [116](#)
- [Kru00] W. Kruer, *Phys. Plasmas* **7**, 2270 (2000). [1](#)
- [Kul87] K. C. Kulander, *Phys. Rev. A* **35**, 445 (1987). [16](#)
- [Laf01] A. Lafosse *et al.*, *J. Chem. Phys.* **114**, 6605 (2001). [103](#)

- [Laf03] A. Lafosse, M. Lebech, J. C. Brenot, P. M. Guyon, L. Spielberger, O. Jagutzki, J. C. Houver and D. Dowek, *J. Phys. B* **36**, 4683 (2003). [98](#), [100](#), [102](#), [103](#), [105](#), [111](#)
- [Lam76] P. Lambropoulos, *Adv. At. Mol. Phys.* **12**, 87 (1976). [10](#)
- [Lat93] C. J. Latimer, K. F. Dunn, N. Kouchi, M. A. McDonald, V. Srigengan and J. Geddes, *J. Phys. B* **26**, L595 (1993). [97](#)
- [Lat96] C. J. Latimer, J. Geddes, K. F. Dunn, N. Kouchi and M. A. McDonald, *J. Phys. B* **29**, 6113 (1996).
- [LCLS09] <http://lcls.slac.stanford.edu/>
- [Lei07] M. Lein, *J. Phys. B: At. Mol. Opt. Phys.* **40**, R135 (2007).
- [Lep07] F. LéPine *et al.*, *J. Mod. Opt.* **54**, 953 (2007). [103](#)
- [Lew94] M. Lewenstein, Ph. Balcou, M. Yu. Ivanov, A. L' Huillier, and P. Corkum, *Phys. Rev. A* **49**, 2117 (1994). [24](#)
- [Lin03] F. Lindner, W. Stremme, M. G. Schätzel, F. Grasbon, G. G. Paulus, H. Walther, R. Hartmann, and L. Strüder, *Phys. Rev. A* **68** 013814 (2003). [22](#)
- [Lin04] F. Lindner *et al.*, *Phys. Rev. Lett.* **92**, 113001 (2004). [82](#)
- [Lin05] F. Lindner *et al.*, *Phys. Rev. Lett.* **95**, 040401(2005). [2](#), [91](#)
- [Lun09] <http://www.atto.fysik.lth.se/> [2](#)
- [Mad63] R. P. Madden and K. Codling, *Phys. Rev. Lett.* **10**, 516 (1963).
- [Mai04] Y. Mairesse *et al.*, *Phys. Rev. Lett.* **93**, 163901 (2004) [29](#), [30](#)
- [Mar05] R. López-Martens *et al.*, *Phys. Rev. Lett.* **94**, 033001(2005). [24](#), [28](#), [29](#), [30](#)
- [Mar07] F. Martín *et al.*, *Science* **315**, 629 (2007) [94](#), [95](#), [96](#), [98](#), [105](#), [109](#), [111](#)
- [Mar08] J. P. Marangos, S. Baker, N. Kajumba, J. S. Robinson, J. W. G. Tisch and R. Torres, *Phys. Chem. Chem. Phys.* **10**, 35 (2008).
- [Mar08] G. V. Marr and J. B. West, *At. Data Nucl. Data Tables* **18**, 476 (1976). [70](#)
- [Mau08] J. Mauritsson *et.al.*, *Phys. Rev. Lett.* **100**, 073003 (2008). [80](#)
- [Mev92] E. Mevel, P. Breger, R. Trainham, G. Petite, P. Agostini, J.-P. Chambaret, A. Migus, and A. Antonetti, *J. Phys. B: At. Mol. Opt. Phys* **28**, L401 (1992).
- [Mev93] E. Mevel, P. Breger, R. Trainham, G. Petite, P. Agostini, A. Migus, J.-P. Chambaret, and A. Antonetti, *Phys. Rev. Lett.* **70**, 406 (1993). [11](#), [16](#)

- [Mil88] D. R. Miller, *Atomic and Molecular Beam Methods*, volume 1, chapter Free Jet Sources (Oxford University Press, 1988). [53](#), [55](#)
- [Mil06] D. B. Milošević *et al.*, J. Phys. B **39**, R203 (2006). [2](#), [18](#), [77](#), [90](#)
- [Mor09] F. Morales, J. F. Pérez-Torres, J. L. Sanz-Vicario, F. Martín, Chem. Phys., **366**, 58 (2009). [94](#), [98](#), [111](#), [114](#)
- [Mor09] T. Morishita *et al.* J. Phys. B **42**, 105205 (2009). [80](#)
- [Mos09] R. Moshhammer, D. Fischer, and H. Kollmus, *Many-Particle Quantum Dynamics in Atomic and Molecular Fragmentation*, chapter Recoil-Ion Momentum Spectroscopy and "Reaction Microscopes", (Springer-Verlag Berlin Heidelberg New York, 2003). [55](#)
- [Mul02] H. G. Muller, A. Tip and M. J. van der Wiel, J. Phys. B: At. Mol. Phys. **16**, L679 (1983). [11](#)
- [Mul02] H. G. Muller, Appl. Phys. B **74**, S17 (2002). [34](#), [114](#)
- [Mur84] H. R. Murphy and D. R. Miller, J. Phys. Chem **88**, 4474 (1984). [53](#)
- [Nis97] M. Nisoli, S. De Silvestri, O. Svelto, R. Szipöcs, K. Ferencz, Ch. Spielmann, S. Sartania, and F. Krausz, Opt. Lett. **22**, 522 (1997). [2](#)
- [Oku08] M. Okunishi *et al.*, Phys. Rev. Lett. **100**, 143001 (2008). [80](#)
- [Pau01] P. M. Paul *et al.*, Science **292**, 1689 (2001); [33](#)
- [Pau94a] G. G. Paulus, W. Nicklich, H. Xu, P. Lambropoulos and H. Walther, Phys. Rev. Lett. **72**, 2851 (1994). [20](#)
- [Pau94b] G. G. Paulus, W. Becker, W. Nicklich, and H. Walther. J. Phys. B: At. Mol. Opt. Phys **21**, L703 (1994).
- [Pau03] G. G. Paulus *et al.*, Phys. Rev. Lett. **91**, 253004 (2003). [79](#), [82](#)
- [Per09] J. F. Pérez-Torres, F. Morales, J. L. Sanz-Vicario, F. Martín, Phys. Rev. A **80**, 011402 (2009). [34](#), [94](#), [98](#), [110](#), [111](#), [114](#)
- [Pro97] M. Protopapas, C. H. Keitel, P. L. Knight, Rep. Prog. Phys. **60**, 389 (1997). [25](#), [27](#)
- [Pet88] G. Petite, P. Agostini and H. G. Muller, J. Phys. B: At. Mol. Opt. Phys. **21**, 4097 (1988). [11](#), [12](#)
- [Que05] F. Quéré, Y. Mairesse, J. Itatani, J. Mod. Opt., **52**, 339 (2005). [30](#), [32](#)
- [Rie80] H. Riess, Phys. Rev A **22** 1786 (1980). [16](#), [17](#)

- [Rie92] H. Riess, Prog. Quant. Electr. **16**, 1 (1992). [16](#)
- [Rem06] T. Remetter *et al.*, Nat. Phys. **2**, 323 (2006). [80](#)
- [Rem99] B. A. Remington, D. Arnett, R. P. Drake, H. Takabe, Science **284**, 1488 (1999). [1](#)
- [Rem00] B. A. Remington, R. P. Drake, H. Takabe, D. Arnett, Phys. Plasmas **7**, 1641 (2000). [1](#)
- [Rie06] H. Rietz, *Aufbau und Inbetriebnahme einer Apparatur zur Erzeugung hoher harmonischer Strahlung und deren Charakterisierung*, Diploma Thesis, Ruperto-Carola University of Heidelberg (2006). [3](#), [47](#), [48](#), [99](#)
- [Rud04] A. Rudenko *et al.*, J. Phys. B **37** L407 (2004). [16](#), [18](#), [84](#), [86](#)
- [Sal02] P. Salières, *et al.*, Science **292** 902 (2001). [25](#), [26](#)
- [Sem03] S. K. Semenov and N. A. Cherepkov, J. Phys. B: At. Mol. Opt. Phys. **36** 1409 (2003) [105](#)
- [San97] I. Sánchez and F. Martín, J. Chem. Phys. **106**, 7720 (1997). [97](#)
- [San98] I. Sánchez and F. Martín, Phys. Rev. A **57** 1006 (1998). [97](#)
- [San99a] I. Sánchez and F. Martín, Phys. Rev. A **60** 2200 (1999). [97](#)
- [San99b] I. Sánchez and F. Martín, Phys. Rev. Lett **82** 3775 (1999). [97](#)
- [San08] A. Sandhu *et al.*, Science **322**, 1081 (2008). [2](#), [34](#), [93](#)
- [Sans09a] G. Sansone, *private communication*. [113](#)
- [Sans09b] G. Sansone, *private communication*. [111](#), [117](#)
- [San06] J. L. Sanz-Vicario, H. Bachau, F. Martín, Phys. Rev. A, **73**, 033410 (2006). [97](#)
- [Sim09] K. Simeonidis, *private communication*. [49](#)
- [Sch93] K. J. Schafer, Baorui Yang, L. F. DiMauro, and K. C. Kulander, Phys. Rev. Lett. **70**, 1599 (1993).
- [Sch97] H. T. Schmidt *et al.*, Hyperfine Interactions **108**, 339 (1997). [53](#), [54](#)
- [Sch07] M. Schultze *et al.*, New J. Phys. **9**, 243 (2007). [75](#), [81](#)
- [Spa04] M. Spanner *et al.*, J. Phys. B **37**, L243 (2004). [80](#)
- [Spr92] P. Spranglet and E. Esarey, Phys. Fluids B **4**, 2241 (1992).

- [Sta95] H. Stapelfeldt, E. Constant and P. Corkum, *Phys. Rev. Lett.* **74**, 3780 (1995).
- [Sta03] H. Stapelfeldt and T. Seideman, *Rev. Mod. Phys.* **75**, 543 (2003). [103](#)
- [St004] A. Stolow, A. E. Bragg and D. M. Neumark, *Chem. Rev.* **104**, 1719 (2004).
- [Str79] S. Strathdee and R. Browning *J. Phys. B: At. Mol. Phys.* **12**, 1789 (1979). [97](#)
- [Ton79] G. Tondello, *J. Mod. Opt.* **26**, 357 (1979). [49](#), [50](#)
- [Ten96] J. Tennyson, *At. Data Nucl. Data Tables* **64**, 253 (1996). [97](#)
- [Tse83] I. Tserruya *et al.*, *Phys. Rev. Lett.* **50**, 30 (1983). [91](#)
- [Uib07] M. Uiberacker *et al.*, *Nature (London)* **446**, 627 (2007). [2](#)
- [Ull03] J. Ullrich *et al.*, *Rep. Prog. Phys.* **66**, 1463 (2003). [3](#), [43](#)
- [Ven96] V. Véniard, R. Taïeb, and A. Maquet, *Phys. Rev. A* **54**, 721 (1996). [33](#)
- [Wie03] R. Wiehle, B. Witzel, H. Helm, and E. Cormier, *Phys. Rev. A* **67**, 063405 (2003) [11](#), [13](#)
- [Wol05] M. Wollenhaupt, V. Engel, and T. Baumert, *Annu. Rev. Phys. Chem.* **56**, 25 (2005). [1](#)
- [Xie90] J. Xie and R. N. Zare, *J. Chem. Phys.* **93**, 3033 (1990). [40](#)
- [Yang93] B. Yang, K. J. Schafer, B. Walker, K. C. Kulander, P. Agostini, and L. F. DiMauro, *Phys. Rev. Lett.* **71**, 3770 (1993). [20](#)
- [Zew00] A H. Zewail, *J. Phys. Chem. A* **104**, 5660 (2000). [1](#), [93](#)



# Acknowledgments

The work presented here would not have been possible without the contributions of several people, to whom I am deeply indebted.

I would first like to thank the head of our group at MPI-K, Joachim Ullrich, for providing me with the motivation, opportunity, and infrastructure to carry out this work. I am also grateful to Konstantin "Konni" Simeonidis, our team leader, for his constant support in building, and bringing into operation the Reaction Microscope at the HHG laboratory and in making my PhD experience an instructive and memorable one. Robert Moshhammer, Claus Dieter Schröter, Daniel Fischer and Artem Rudenko have also been readily available for expert guidance and timely trouble-shooting. I have also benefited greatly from excellent discussions with Alexander Voitkiv, Bennaceur Najjari, Dieter Bauer and Thomas Pfeifer.

I have immensely enjoyed working in our "Attosecond Dynamics" team of MPI-K, consisting of Helga Rietz, Alexander Sperl, and Andreas Fischer, who have been assisting and encouraging me in my PhD endeavors. In particular, Helga and Alex were of invaluable help in running the laser and HHG system stably, for long periods of time.

For the experiments at MPQ, Garching, Matthias Kling and Matthias Lezius were instrumental in organizing the beamtime, and I thank Oliver Herrwerth and Sergey Zherebtsov for their excellent cooperation. In the final stages of my PhD work, I have had the opportunity to work with Giuseppe Sansone and Francesca Calegari, who were guests to our lab from Milan. To Giuseppe, I am thankful for many, long, exhaustive, discussions and particularly for suggesting the  $D_2$  experiment, and to Francesca for assistance during this experiment.

Our work at the MPI-K could not have been smooth and well-oiled without the support of Bernd Knape, Claudia Ries and Helga Krieger. I would also like to thank the "old guard" of PhD students of Sebastian Dewald, Martin Dürr and Thorsten Ergler and former members of our team, Petros Tarantilis and Georg Gademann for their initial aid.

The experience of working at MPI-K has been enjoyable, partly on account of co-workers like Michael Schuricke, Siva Ramakrishnan and Petros who have always managed to raise our flagging spirits. In fact, I express my thanks to all the members of the Ullrich division at MPI-K for their help and cooperation.

I dedicate this work to my parents and teachers, without whom, this would never have been possible. Finally, words fail to convey my gratitude to my wife, Vandana Sharma, who has been source of my strength and motivation all-throughout, both at the lab and

at home.